ResearchGate

See discussions, stats, and author profiles for this publication at: https://www.researchgate.net/publication/342453673

Master thesis Horacek

Thesis · August 2000

DOI: 10.13140/RG.2.2.18843.28967

CITATIONS
0

READS
39

1 author:

J. Horacek
The Czech Academy of Sciences
169 PUBLICATIONS **2,988** CITATIONS

SEE PROFILE

Some of the authors of this publication are also working on these related projects:

tokamak physics View project

All content following this page was uploaded by J. Horacek on 25 June 2020.

The user has requested enhancement of the downloaded file.

Charles University in Prague
Faculty of Mathematics and Physics
Institute of Particle and Nuclear Physics

DIPLOMA THESIS

Jan Horáček

Turbulent structures in tokamak plasma

Academy of Sciences of the Czech Republic
Institute of Plasma Physics
Association EURATOM / IPP.CR
Tokamak CASTOR

Supervisor: RNDr. **Jan Stöckel**, CSc.

Printed: August 18, 2000

This thesis was performed by myself only (except chapter 8), being supervised by RNDr. Jan Stöckel, CSc. (Work at CASTOR part) and Dr. R.A. Pitts (Work at TCV part), and used only the literature listed in the bibliography.

I agree with borrowing of this thesis.

Tuto diplomovou práci jsem vypracoval samostatně (kromě kapitoly 8) pod vedením RNDr. Jana Stöckela, CSc. (Work at CASTOR part) a Dr. R.A. Pittse (Work at TCV part), a použil jsem jen uvedenou literaturu.

Souhlasím se zapůjčováním této práce.

Jan Horáček

Contact to the author
E-mail: horacek@ipp.cas.cz, WWW: http://tokamak.ipp.cas.cz/∼horacek

Contact to the supervisor
E-mail: stockel@ipp.cas.cz, tel. (+420 2) 6605 2037

- this thesis is available on http://tokamak.ipp.cas.cz/∼horacek/thesis.html
- scientifically the most important work is included in chapters 8 and 12
- concepts written in *italic* are mostly present either in the Index or in the appendix D

typeset in LaTeX

Once a physicist said: let a Sun be on the Earth!

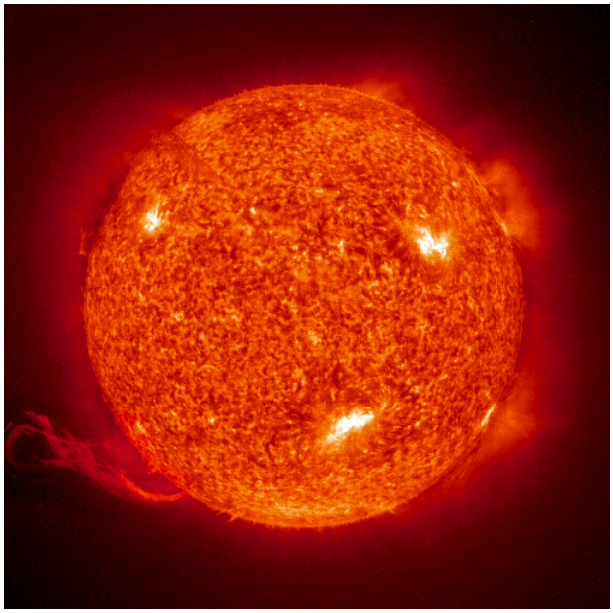

The reason why I focus my mind on field of the nuclear fusion is the current global problem of the mankind:
Searching after an environmentally acceptable and long-lasting energy supply.
Tokamak nowadays seems to be the best candidate to realize the thermonuclear fusion on the Earth.

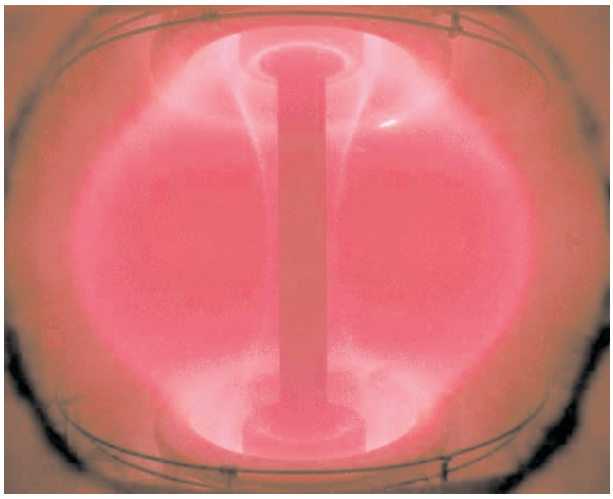

... and searched out a tokamak.

Contents

Part I

Introduction

Chapter 1

Why just fusion?

1.1 Energy crisis

The following Tab.1.1 shows the available energy supplies or methods currently present at the Earth. These numbers assures us about the real actuality of the *energy problem*. Its consumption in different places of the Earth is also strongly heterogeneous, the developing countries will *surely strongly increase* their energy demands in the next decades. In addition, burning fossil fuels (coal, oil, gas) leads to the well-known *green-house effect* which is being taken as a serious problem even already by politician.

For more information see [50, in czech], [42, p. 193] and generally about current global environmental problems read the fundamental works [48], [49].

1.2 Renewable energy sources

These following items are in more detail described in e.g. [45, p. 31-42], or in details in thesis [6, in czech].

method/resource	reserve time [years]
coal	300
oil	40
gas	50
^{235}U	30
$^{238}U + ^{232}Th$ (breeders)	30000
fusion (D+T)	10^7
fusion (D+D)	10^{10}

Table 1.1: Current total energy resources [1, p. 25] (the annual worldwide consumption is nowadays $3 \times 10^{20} J$, i.e. 1.5 kW per each Earth inhabitant).

Biomass

Environmental characteristics of biomass are comparable to the case of coal, the only advantage is its renewability.

Solar energy

The Sun emits power of $1.3\ kWm^{-2}$ on our planet. One half of this is absorbed or reflected by the atmosphere; multiplicate this value by $\cos\alpha/\pi$ (α is the latitude) and further by the current efficiency of the photovoltaic elements of $max.\ 14\%$ one finally gets only $20 - 30\ W_e m^{-2}$.

This power density implicates that a power station with electric power of about $1GW_e$ (nowadays standard power-station) would cover $\sim 10 - 20\ km^2$ of the Earth surface with the solar panels! Such a system also needs additional *accumulation system* for nights, cloudy days and winter, i.e. in times of the largest energy demand.

For example, a solar element made in the Czech Republic at present has the following parameters [55]:

- Area: $0.36m^2 \Rightarrow$ average day/night & winter/summer electricity *power* in European latitude: $\sim\ 7 - 11W$
- Lifetime: 10-20 years, during which it earns $\$180$ (using electricity price of $ 0.1/kWh)
- Price: $ 430 + accumulator system + voltage-up conversion + personal staff

The price of electricity is therefore $\sim 10\times$ higher than from the conventional supplies. In other words, only the amount of energy eaten to make a solar element returns after several years of its operation!

Available current usages of such *electric* energy source are only special: buoies, space crafts, distant (isolated) houses.

The accumulator system is troublesome by its own. It can be well-solved in case of not selling electricity into the grid but using the electric power from the solar cells for *water electrolysis* to produce *hydrogen* as a fuel for engines. There already exist experiments in using hydrogen in cars [53, p. 61, p. 40].

Reasonable use of solar energy for *heating* can be realized in solar furnaces or in collectors for water heating.

Wind

It is technically problematic to achieve high powers per one power station, normally up to 100 kW [6]. Nowadays it is minimally $4\times$ more expensive than from the grid.

Waves, flood-tide

Flood-tide power stations need flood-tide high enough (10-18m) which *limits their localities*, however, the output power can reach even several gigawatts!

Wave power stations, that make use of the force of sea-waves, are still in development.

Water

There is need of high altitude differences and high water-flow and large areas. They are available for covering peak energy demands.

Geothermal

There is huge amount of accumulated thermal energy in a thin layer of the Earth. At present there are commercially available *heat pumps* that "pumps" the geothermal energy from deep (100-200 m) wells to heat houses flats and residences.

1.3 Nuclear fission

Advantages

- Tradition – long-lasting experience (since the 2nd WW), physical & technological problems well-solved
- (In the past) *cheap electricity*

Disadvantages

- *Risk of uncontrolled nuclear fission* (**hundred tons** of the fuel inside the reactor!) $\Rightarrow$ *Radioactivity getaway* danger (Three mile Island 1979, Chernobyl 1986 [46])
- *Radioactive waste* (the high level active waste of has to be *isolated* from the environment $\sim$500 years)
- *Uranium (UO_2) supplies* limited (see Tab.1.1)
- Electricity cost increases due to increasing requirements on *safety and environmental cleanness* which makes it nowadays comparable or even more expensive than conventional supplies
- High & increasing *disbelief* in the public

1.4 Thermonuclear fusion

Advantages

- **Inherent safety**
  - in principal *no uncontrolled nuclear reaction danger (like "explosion")* because the reaction is self-unstable (no chain reaction)
  - only **several grams** of the fuel in the reactor
- Fusion does not give rise to *greenhouse gases* (CO_2) or acid rain gases ($SO_2,\ NO_2$)
- *Fuel source* is **huge** and the cheapest one: just deuterium (from water by electrolysis) and lithium (for T-production by Eq.(2.7), gained e.g. from sea water in form of Li_2CO_3, see e.g. www.limtech.com) $\Rightarrow$ the fuel price is 10^{-4} of current electricity cost [1, chap. 1.8]
- The *waste* is harmless helium and lower level active waste from the construction materials (no high level waste as in the fission case)

Disadvantages [42, p. 225], [43], [52]

- *Radioactivity* from construction materials, Fig.1.2. $\frac{fission\text{: }200\ MeV}{fusion\text{: }17\ MeV}$ per one neutron yield $\Rightarrow$ *an order of magnitude higher neutron flux* in comparison to the fission case

- Essential problem is the need of *tritium*:
  - Tritium is weakly β–radioactive ($T_{1/2} = 12\ years$), flammable and toxic.
  - T is just an isotope of hydrogen $\Rightarrow$ T is chemically identical to ${}^{1/2}H$ $\Rightarrow$ tritium bounds into water molecules T_2O !

  $\Rightarrow$ total amount of tritium in a fusion power-plant building has to be limited under $2\ kg$ [52, p. 19-20][1]. In tokamaks T will be produced in the blanket from lithium, Eq.(2.7).

  However, the more demanding ($10\times$ higher ignition temperature) fusion reaction[2] $D + D$ *does not need any* T.

- Huge *technological problems*:
  - wall and divertor materials will be exposed to *enormous power and radiation loads*; current materials withstand power load below $5MW/m^2$ [1, p. 651] (comparable to power outflux of a $100\ W$ bulb filament); solution of this problem is a job for divertor designers
  - high magnetic field of $B_t \sim 10T$ in large volume ($\sim 10^3 m^3$) requires *superconducting* toroidal field coils
  - high *price* $\sim 1 - 3\times$ higher than of fission plants [1, chap. 1.9] $\Leftarrow$ mainly due to *high capital requirement*

For more details look in [47], [44], [5].

[1] Estimated for case of sudden total release into environment.

[2] the "2^{nd} generation" of fusion reactors

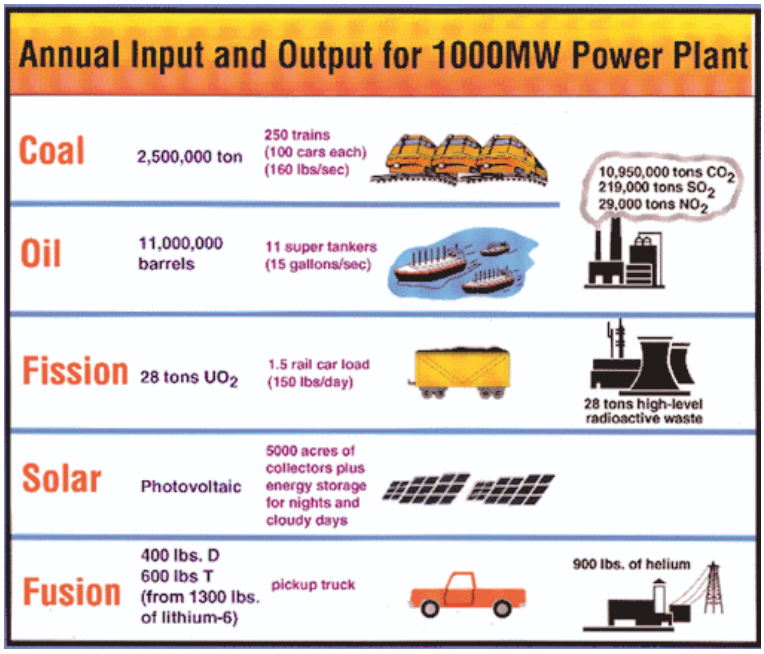

Fig. 1.1: Annual inputs and outputs of a $1GW_e$ power-station

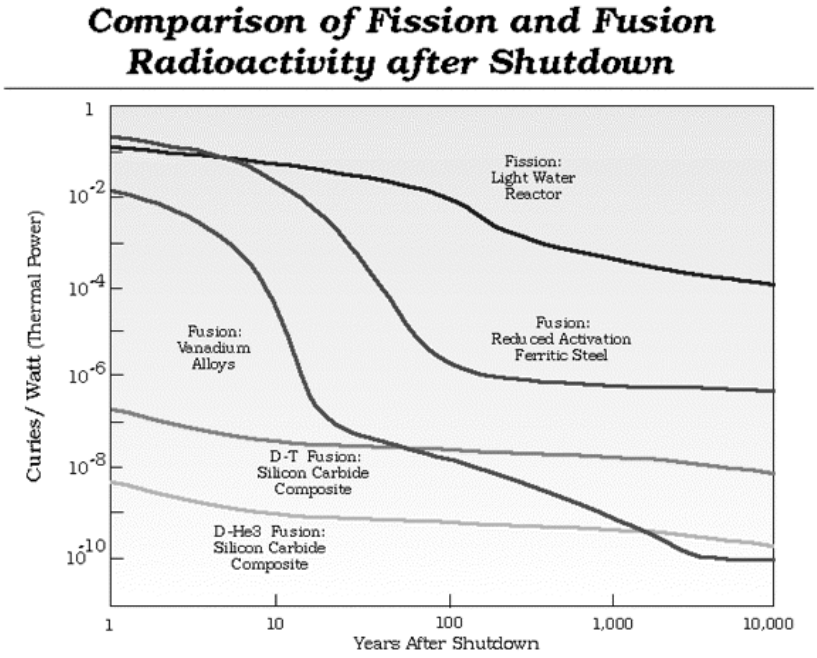

Fig. 1.2: Fall of radioactivity after fission/fusion reactor shut-down

Chapter 2

Fusion and tokamaks

In this chapter general introduction to fusion, the used fuel and its principal advantage as a new energy source is present. In a more pedagogical form it also available on the web at

www.ipp.cas.cz/tokamak

by clicking on Education (Výuka) after choosing appropriate language.

2.1 Fusion research nowadays

There are several large fusion devices (Great Britain, Japan, Germany, France) and tens of middle- and small-sized machines all over the world. Fusion power producing ones are only JET (Great Britain) and TFTR (USA, closed in 1998), see Fig.2.1; no more because using low-level-radioactive tritium is mostly unnecessarily complicated and therefore all other devices use only deuterium plasma (therefore with no fusion reactions).

A new very large device is planned to be constructed in the near future. This Next Step , the less ambitious one than ITER[1], [42, p. 228], Fig.2.2 which was planned to produce about $1500\ MW_{Th}$ and costed $\$_{'89}$ 6 billions[2] [1, chap. 13.4]. For comparison, the U.S. fusion budget was $260 million in 1996, total worldwide fusion budget (managed mainly by Europe, Japan and (until 1998) USA) is roughly $1 billion, total worldwide military budget is $\$_{'88}$ 1000 billions per year [40, p. 127][3]! The Next Step device would be still experimental but would cost only half of the price, and produce only $500\ MW$ and offered locations are mainly Canada[4] and France[5]. The first power-stations (Fig.2.4) based on fusion are not planned before 2030.

Whether the whole world fusion research is or is *not* expensive depends on the point of view: the estimated requirements of the fusion research over the next 20 years (i.e. until a demonstrating fusion power-plant) is $ 50 billions. This can be expressed, for example, as a "fusion tax" on gasolene of 0.1% of its current price over the same time [51, p. 11]; for

[1] www.iter.org, www.itereu.de, International Thermonuclear Experimental Reactor, rejected after stopping fusion programme in the USA, 1998

[2] Billion = 10^9

[3] The amount is really huge in comparison to anything.

[4] http://www.itercanada.com

[5] PlasmaNet on 6.8.2000: "Mr. Schwarzenberg, the new French minister responsible for nuclear energy, is now laying the emphasis of the development of French nuclear energy on fusion."

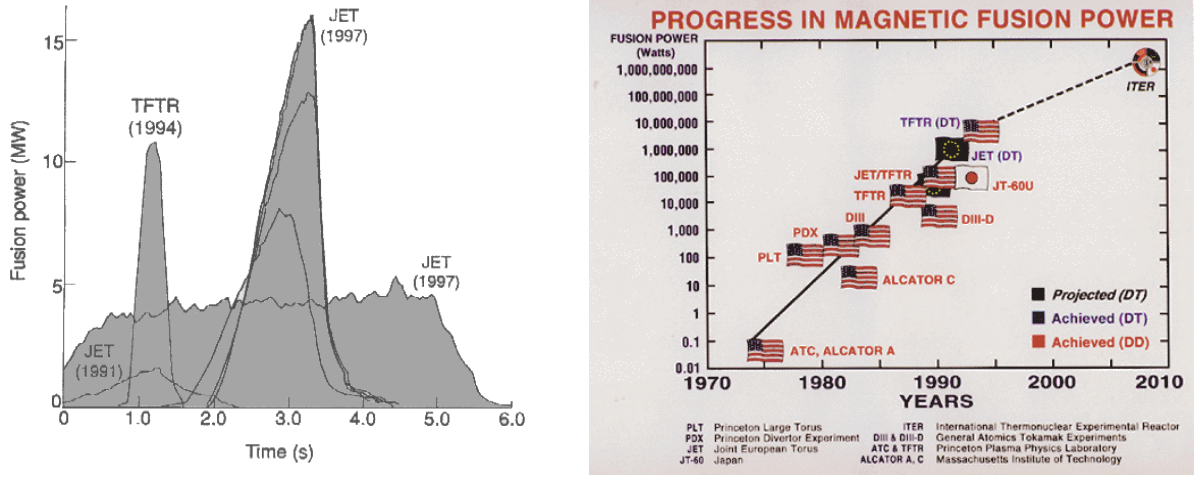

a) **b)**

Fig. 2.1: **a)** Record fusion powers achieved in the largest world tokamaks, **b)** Progress in magnetic fusion

comparison: the gasolene in the Czech republic raised extremely fast of about 50% during the year 1999 as a reaction to nearly the same worldwide increase.

Latest news of the European Commission fusion programme is available at fire.pppl.gov.

2.2 What is nuclear fusion?

The thermonuclear fusion is based on reaction which is naturally present in stars [1, chap. 1.2]:

$$\begin{aligned} D + T &\rightarrow^4 He + n + 17.6\ MeV \\ D + D &\rightarrow^3 He + n + 3.3\ MeV \\ D + D &\rightarrow^3 T + p + 4.0\ MeV \end{aligned} \tag{2.1}$$

where $D \overset{\text{def}}{=} {}^2_1H$, $T \overset{\text{def}}{=} {}^3_1H$ are deuterium, tritium, respectively.

To ignite this reaction[6] it is necessary to achieve the so-called *Lawson criteria* [1, p. 11]:

$$n \cdot T \cdot \tau_E \geq C_{crit,D+T} \approx (3-5) \times 10^{21} sm^{-3} keV, \tag{2.2}$$

where τ_E is the *energy confinement time*, n, T is the volume-averaged density and temperature, respectively. The condition would be reached for example by $n = 10^{20} m^{-3}, T = 10keV, \tau_E = 3s$. There are An order of magnitude higher requirements for the DD-reaction in Eq.(2.1) that does not need tritium which is, from the environmental safety point of view, dangerous [52].

To achieve and keep these conditions a magnetically confined device tokamak has been proposed, described in the following section.

[6] I.e. the fusion power being higher than radiative and particle energy losses.

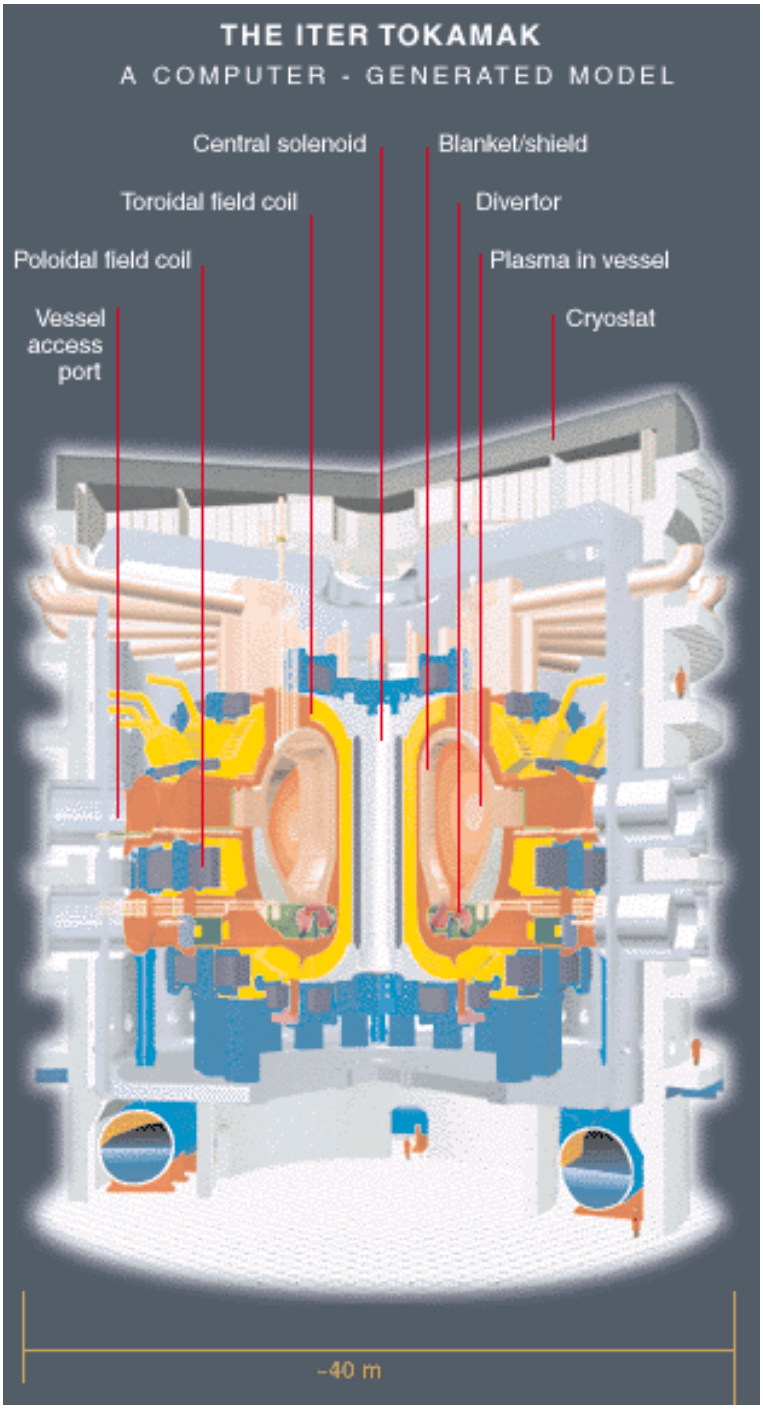

Fig. 2.2: The planned international device ITER: size compare with a man at right bottom, temperature of $12\ keV$, output electric power of $1.5\ GW_{Th}$, burn duration of 1000s, costs $\$_{'89}$ 6 billions.

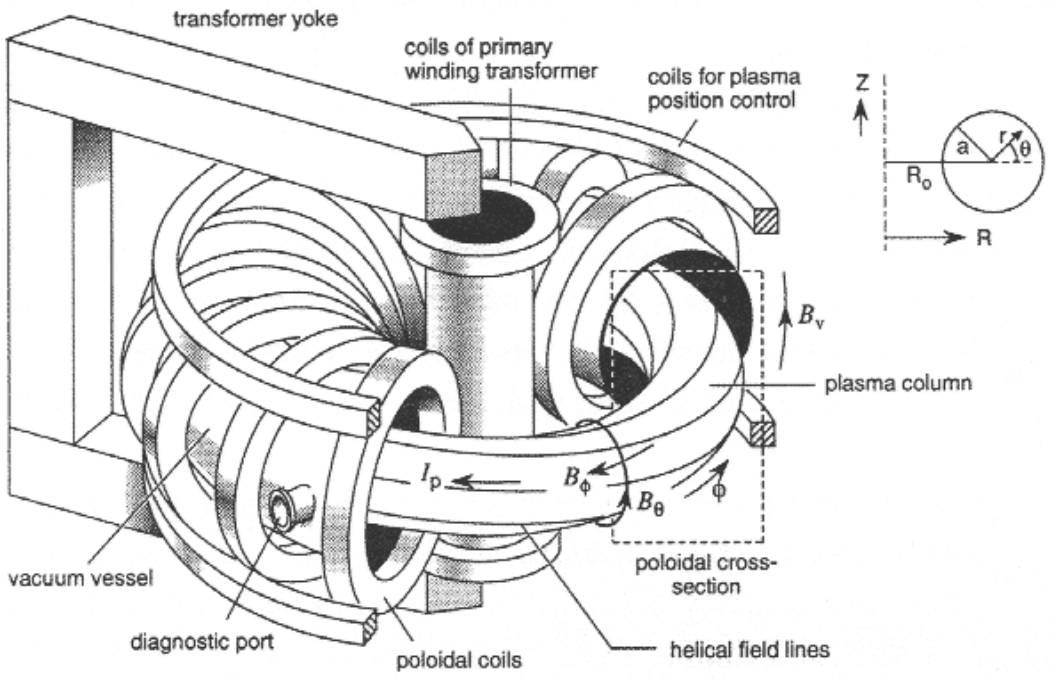

Fig. 2.3: Schematic view of a tokamak device

2.3 What is tokamak?

Tokamak has been proposed by russian scientist Artsimovich in half of the 20th century. Nowadays tokamak seems to be the most perspective fusion device in comparison to others[7]: stellarators, (Z/Θ) - pinches, magnetic mirrors, inertial (laser) fusion[8], [2, chap. 9].

2.3.1 Magnetic confinement

The hydrogen plasma is confined in a toroidal vessel (Fig.3.1) walls by a strong (several Teslas) toroidal magnetic field B_t since the plasma is too hot to touch the walls.

The magnetic confinement is based on the known fact that any charged particle performs helical movement around the magnetic field line with a *Larmor radius* (of cyclotron rotation)

$$r_L = \frac{v_\perp m}{eB}$$

where $v_\perp$ (the *velocity*[9] *perpendicular to the magnetic field*) is given by plasma temperature T:

$$\frac{1}{2}mv^2 = k_B T, \quad v^2 = v_\perp^2 + v_\parallel^2. \tag{2.3}$$

For the maximal value of $v_\perp = v$ one can estimate characteristic radius r_L of particle Larmor rotation as a function of temperature:

$$r_L = \frac{\sqrt{2k_B m T}}{eB} \tag{2.4}$$

[7] Our republic is lucky that the only fusion device it has is just a tokamak.

[8] Visit http://www-lasers.llnl.gov

[9] As velocity the standard deviation of the velocity is meant, $\sqrt{< v^2 >}$.

that is (for fusion plasma with $B = 6T, \bar{T} = 10keV$): $43 r_{L,e} = r_{L,ion} \simeq 3cm$ [10].

So, the plasma particles are fixed on the magnetic field lines. Movement *across* the field (i.e. mostly radially) is due to drifts and *collisions* with other particles.

One of principal dangerous drifts is ∇B*-drift* [1, p. 45]: $v \propto \frac{\nabla B \times B}{B^2}$, i.e. pushing particles of opposite signs up or down of the torus $\Rightarrow$ creates vertical electrical field which leads to instability. The additional poloidal magnetic field is thus necessary: it turns particles poloidally, they get on both top and bottom part of the torus and the ∇B-drift is thus, in average, suppressed.

The effect of collisions among particles is described by the well-known Fick's law [2, p. 138] for the radial particle flux Γ_r:

$$\Gamma_r = -D_\perp \nabla n \equiv -D_\perp \frac{dn}{dr}, \tag{2.5}$$

where this perpendicular diffusion coefficient $D_\perp$ is higher than the *classical diffusion* [2, chap. 9.2.1 in czech edition] and even the *neoclassical diffusion*[11], [1, chap. 4][12].

2.3.2 Heating

The main principal heating of tokamak is the *Ohmic heating*: the conductive plasma column forms the secondary transformer loop of the transformer (see Fig.3.1). The induced voltage (so-called *loop voltage* U_{loop}) drives current through the plasma column (so-called *plasma current* I_p) and therefore *heats* it by the *Ohmic heating* $P_{OH} = U_{loop} I_p = \eta U_{loop}^2$. Unfortunately, the *plasma resistivity* η decreases with temperature as $\eta \propto T^{-3/2}$ even below copper resistivity for the desired fusion conditions (Eq.(2.2)). Therefore the Ohmic heating is not powerful enough for high temperatures and other heating methods have to be used [1, chap. 5].

2.3.3 Heat transfer

The produced heat from the nuclear reaction would be converted to electricity by the common steam-cycle, as depicted in Fig.2.4 and in the following:

Heat transfer

plasma center $\Rightarrow$ *SOL* $\Rightarrow$ *divertor plates and blanket* $\Rightarrow$ *cooling medium* $\Rightarrow$ *water steam* $\Rightarrow$ *steam turbine* $\Rightarrow$ *dynamo* $\Rightarrow$ *electricity*

The 2nd generation fusion devices (only deuterium plasma, DD in Eq.(2.1)) could *avoid* the steam-cycle because all heated particles are *charged* such that can be used the *MHD-dynamo effect* charged particles flying off the plasma column are focused into a tube with *electrostatic plates* slowing them down and so transferring their kinetic energy directly into electricity [2, p. 305].

[10] For CASTOR or TCV parameters it is less even by two orders of magnitude, see Tab.3.1 or Tab.9.1.

[11] taking into account the tokamak configuration

[12] In linear (i.e. not-curved $\Rightarrow \nabla B \sim 0$) devices (e.g. "magnetic mirrors") this poloidal field is therefore not necessary and thus no current drive is needed (which can not, however, exist in such an open system).

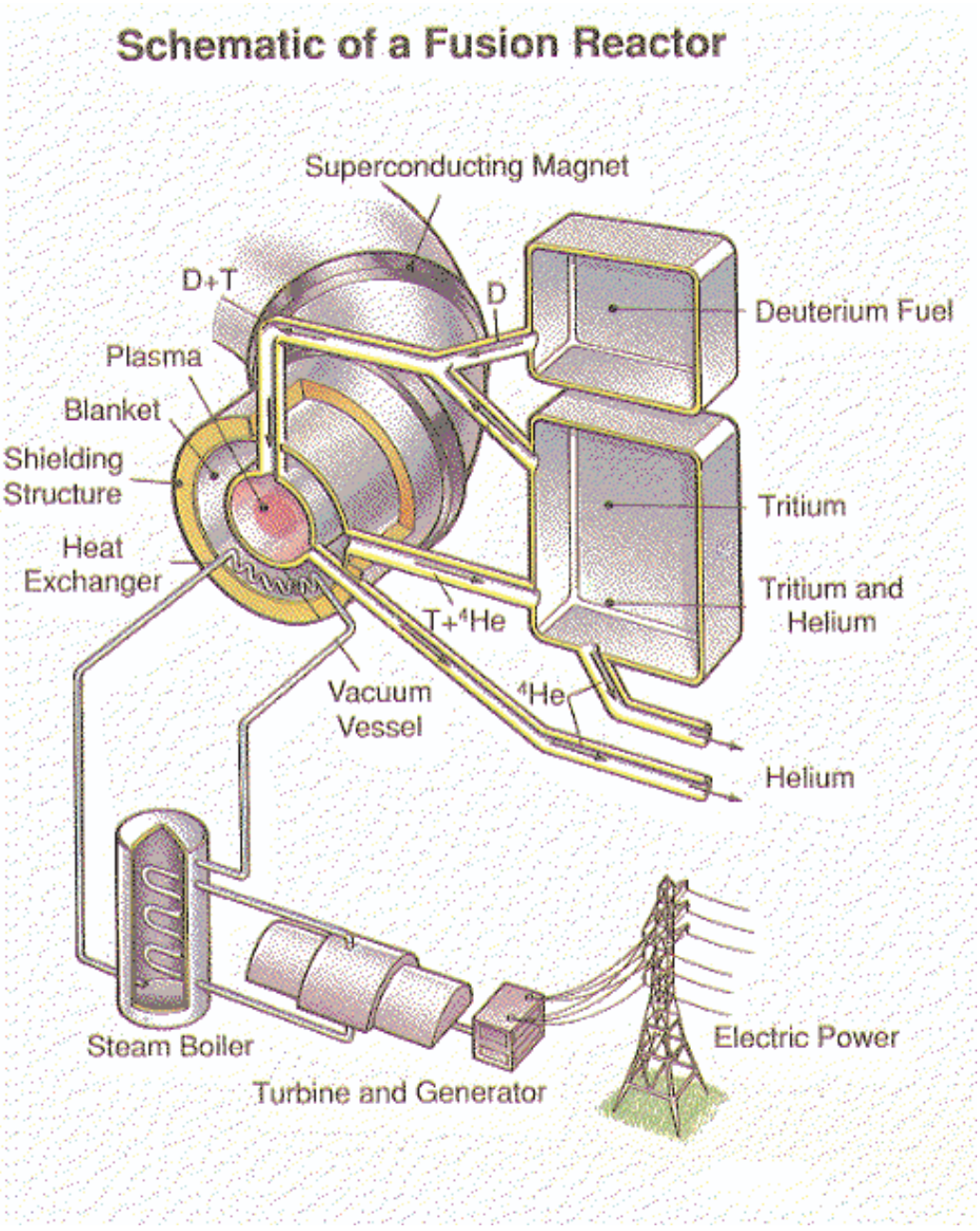

Fig. 2.4: Schema of a tokamak-like power-station

2.3.4 Tritium breeding in blanket

Tritium is very rarely present in the Nature. It has to be bred in the *blanket* (consisted from Li_2O, look at Fig.2.4) by reactions ([1, p. 18, 24]):

$$n + {}^6Li \rightarrow T + {}^4He + 4.8MeV \tag{2.6}$$

$$n + {}^7Li \rightarrow T + {}^4He + n - 2.5MeV \tag{2.7}$$

The natural abundances are 7.4% of ${}^6Li$ and 92.6% of ${}^7Li$. The blanket is also useful to absorb the fusion α–particles and neutrons[13] and therefore for the heat transfer (the lithium thus has to be in a liquid state).

[13] this radioactive shielding has to reduce the neutron energy flux by 6-7 orders of magnitude to avoid damage and heating of the superconducting toroidal B-field coils; made from high Z-material such as steel of $1\ m$ of thickness

Part II

Work at CASTOR (electrostatic fluctuations)

Work aims

Plasma in toroidal magnetic vessels of the tokamak type is in a turbulent state. *Turbulent structures* in the plasma causes *the confinement time* to be $10^{1\div3}\times$ shorter (i.e. worse) than predicted by the neoclassical theory [1, p. 145]. Although the turbulence in tokamaks is studied for long time its *fundamental* or the way *how to suppress it* is not understood enough for to have the confinement time high enough to have the thermonuclear reactions burning by itself.

This thesis should be focused on *experimental study* of the turbulent structures created during a discharge at the CASTOR tokamak. Basic diagnostic tools are *multiple-tip Langmuir probes* measuring local plasma parameters: density, potential and temperature, respectively, with high resolution both in time and space.

I will mainly focus on estimation of *characteristic sizes* and lifetimes of the turbulent structures in the radial direction. These experiments will be executed both in *standard discharges (ohmic heating, OH)* and also in *Biased discharges (Biasing)*, i.e. these with hopefully better confinement reached by creating radial electric field at the edge of the tokamak plasma column.

The aims are to contribute to *turbulent structure characterization*, its origins and the way how to suppress the turbulence transport.

In more detail I will focus on *comparison of turbulence* of two types of discharges (Ohmic, Biased) in:

- Measurement of *poloidal and radial profiles* (of fluctuations) of plasma density and potential using multiple-tip Langmuir probes with time and space resolution high enough (typically $1\mu s,\ 2.5mm$)
- *Poloidal and radial cross-correlation function (CCF)* computation; i.e estimation of the turbulence characteristic parameters like: amplitude, life-time, radial and poloidal decay-lengths, poloidal phase velocity, density vs. potential correlation, density vs. poloidal electric field correlation (i.e. ExB-outflux)

Some effort has been also done in other fields (Hurst analysis (avalanches), Reynolds stress) without including them into this thesis.

Chapter 3

Tokamak CASTOR

The CASTOR tokamak (http://www.ipp.cas.cz/tokamak) is one of the oldest, still-working machines in the world (built up in Moscow in the end of fiftieth), brought to Prague in 1976 and reconstructed at half of eighties. The main aims of the experimental research are:

- study of plasma turbulence
- study of some aspects of non-inductive current drive
- development of new diagnostics
- education of students

Just recently (1999), the tokamak research in the Institute of Plasma Physics (www.ipp.cas.cz) has been associated, [53, No.6, 2000, p. 28] or [54], to the European fusion programme EURATOM.

My work at physics of the thermonuclear fusion begun just at this device in 1996.

Years ago there used to live a tomcat in the CASTOR building. He used to hunt mouses and we all loved this Castor (as everyone called him). Once, however, he has gone away and what only left is his shadow in our logo, see also [56].

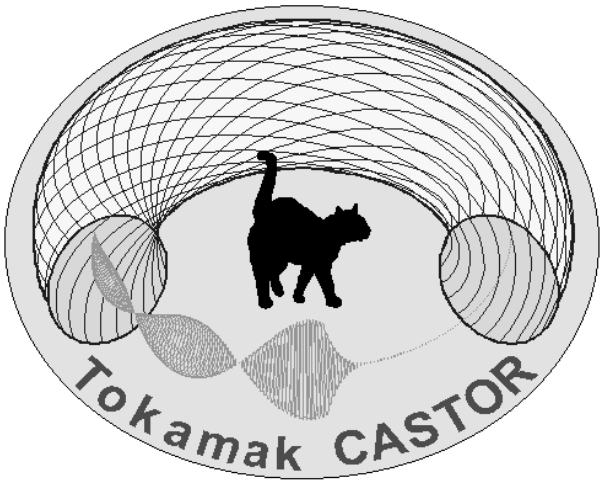

3.1 Technical parameters

Tokamak CASTOR is a small device (the major radius of $R = 0.4\ m$) and circular cross-section of plasma column, Fig.3.1. The minor radius is fixed by a poloidal *limiter*[1] of radius

[1] Explanation of what is limiter is described in Appendix (section C.2.1).

Toroidal magnetic field B_t	$1T$
Additional heating	none
Additional current drive	LHCD
Plasma current I_p typical	$8kA$
Loop Voltage	$1-2V$
Plasma duration	max. $30ms$
Poloidal plasma shape	circular cross-section
Major radius	$R = 400mm$
Minor radius (limiter)	$a = 85mm$, occasionally $a = 60mm$
Radius of the vessel	$b = 100mm$
Wall cleaning methods	hydrogen glow discharge heating at $220°C$
Hydrogen fuelling	stationary & gas puffing

Table 3.1: Tokamak CASTOR parameters

$a = 0.085\ m$. Optionally, an additional material limiter with $a = 0.06\ m$ can be introduced into the vacuum chamber to enhance the *aspect ratio*[2] *A=R/a.* The *safety factor* at the limiter radius, $q(a)$, can be varied in a rather broad range, $q(a) = 2.8 \div 15$ ($B_t = 0.5 \div 1.2\,T,\ I_p = 5 \div 15\,kA$). The line average density is kept around $\bar{n}_e = 0.4 \div 3.0 \cdot 10^{19} m^{-3}$, the central electron temperature being in the range of 150 - 250 eV.

The position of the plasma column within the vacuum vessel (liner) is *feedback-stabilized* both in the horizontal and vertical directions.

This tokamak is equipped with a radio-frequency system for non-inductive current drive with lower hybrid frequency band (Lower Hybrid Current Drive). Furthermore, the radial electric field can generated at the plasma edge by means of a biased electrode, described in more detail in chapter 8.

Of course, in such small tokamak no fusion power can be produced because the temperature and energy confinement time $\tau_E \approx 1\ ms$ are by $2 \div 3$ orders less than necessary to achieve fusion conditions, Eq.(2.2).

Nevertheless, this small experimental device has several advantages to study some aspects of physics still relevant to fusion-like plasmas:

- the device is flexible; opening of the vacuum vessel and replacement of diagnostic tools is easy
- plasma is well accessible; diagnostics ports are available at top, bottom & midplane of the torus
- discharges are reproducible; $\sim$100 shots a day can be easily reached
- tools for external influencing of plasma are available (LHCD, edge plasma polarization)
- unique diagnostics methods for investigation of edge plasma are well-developed (multiple-tip arrays of LP, available to get deep into the confined plasma)

[2] Read the unknown concepts in Tab.D

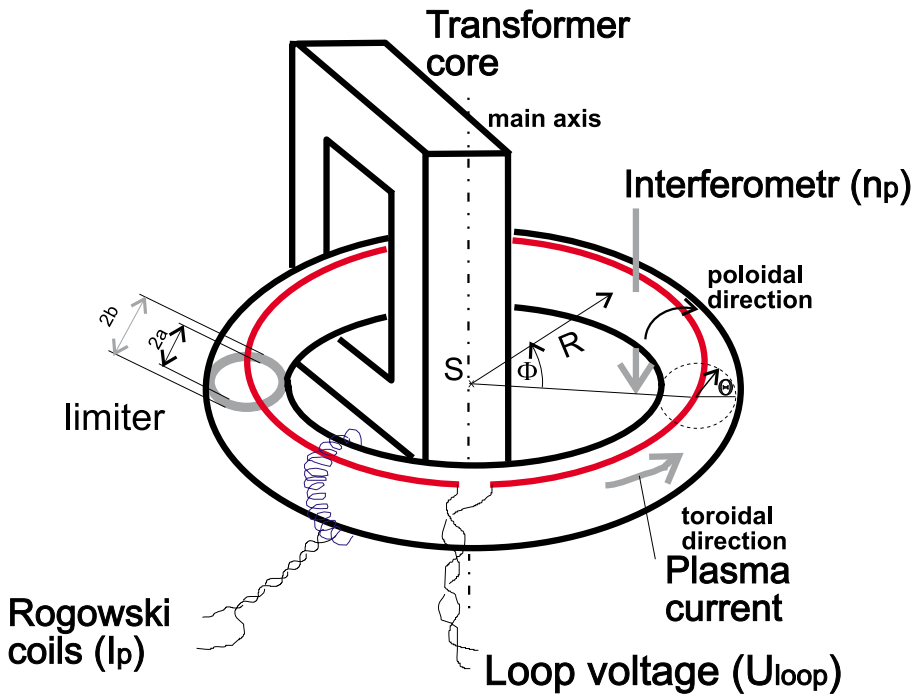

Fig. 3.1: Schematic view of a tokamak device with depicted standard diagnostics.

3.2 Standard diagnostics

Standard diagnostics used for measuring macroscopic parameters of a discharge are depicted schematically in Fig.3.1.

3.2.1 Plasma current (I_p)

Toroidal plasma current is measured by a *Rogowski coil (RC)* twisted poloidally around the vacuum vessel (with radius R_c). It measures poloidal magnetic field B_p induced by the plasma current I_p estimated by the Ampere's low:

$$\oint_{vessel} \vec{B} \cdot \vec{dl} = 2\pi R_c B_p = \epsilon I_p \ .$$

Time derivation of magnetic flux Φ through the RC equals the circulation of the electromotive power:

$$\frac{d\Phi}{dt} \equiv \frac{dB_p}{dt} S_{coil} = -\oint_{coil} \vec{E} \cdot \vec{dl} \equiv -k\, U_{coil}.$$

So the final formula goes further:

$$U_{coil} = \frac{-\epsilon S_{coil}}{2\pi k R_c} \frac{dI_p}{dt}, \tag{3.1}$$

where k is number of loops and S_{coil} is cross-section of the coil. The signal U_{coil} is integrated by an analog integrator $U_{out}(T) = \int_0^T U_{coil}(t)dt$, so the plasma current is then (using $I_p(0) = 0$ before a discharge starts)

$$I_p = C_{rc} U_{out}, \quad for\ CASTOR \quad C_{rc} = 4kA/V. \tag{3.2}$$

3.2.2 Loop voltage (U_{loop})

The voltage induced by a single toroidal loop turned along the torus is:

$$U_{loop} = -\frac{d\psi}{dt},$$

where ψ is the magnetic flux through the transformer core. So the toroidal electric field accelerating the charged particles in the plasma column is: $E_t = \frac{U_{loop}}{2\pi R}$, for CASTOR usually $0.8V/m$.

The loop voltage is related to the resistivity R_p and inductance L_p of the plasma column as

$$U_{loop} = R_p I_p - L_p \frac{dI_p}{dt} .$$

The inductance of the plasma column on the CASTOR is about $\approx 1\mu H$. So, during the quasi-stationary phase of a discharge the inductance part can be neglected, therefore the resistivity of plasma column can be derived as:

$$R_p = \frac{U_{loop}}{I_p}$$

For typical values of the loop voltage and plasma current on the CASTOR tokamak ($U_{loop} \approx 2V, I_p \approx 10\ kA$), the plasma resistivity is $R_p \approx 0.2\ m\Omega$
Similarly, the ohmic heating power of the plasma column is:

$$P_{OH} = U_{loop} \cdot I_p$$

which is typically $P_{OH} \approx 20\ kW$.

3.2.3 Electron temperature (T_e)

Unfortunately, the electron temperature is not measured directly in CASTOR; the *Thomson scattering method* (measure of $T_e(r)$-profile) will be available in the near future. At present there are only two methods for estimation of T_e.

Estimate of T_e from plasma conductivity

The total plasma current can be derived as

$$I_p = \int_0^a 2\pi r j(r) dr, \tag{3.3}$$

where $j(r) = \sigma(r) E_t$ is the *toroidal current density*. If we use the Spitzer's expression ([7, chap. 7.1], generally [1, chap. 2.16]) to estimate the plasma conductivity σ, then:

$$j(r) = 1.923 \times 10^4 \frac{U_{loop}\, T_e(r)^{3/2}}{2\pi R\, f(Z_{eff})\, Z_{eff}\, \ln\Lambda} \qquad [A/m^2, V, m, eV],$$

where

$$f(Z_{eff}) = 1.961(0.29 + \frac{0.46}{1.08 + Z_{eff}}),$$

profile	$T_e(r)/T_e(0)$	$a = 85mm$	$a = 60mm$
Single-parabolic:	$1-(\frac{r}{a})^2$	0.3599	0.5727
Double-parabolic:	$(1-(\frac{r}{a})^2)^2$	0.4924	0.7834
Shifted-gaussian[3]:	$\exp(-(\frac{r-A_1}{A_2})^2)$	0.2706	0.4284

Table 3.2: Values of parameter K_t computed for the CASTOR according to Eq.(3.5).

and $\ln\Lambda = 15$ is the *Coulomb logarithm*. The effective ion charge Z_{eff} is not standardly measured in the CASTOR tokamak. According results of previous experiments we estimate this quantity as $Z_{eff} \approx 2.5$.

After performing integration of Eq.(3.3) we can express the central electron temperature $T_e(0)$ from I_p/U_{loop} measurements as

$$T_e(0) = K_t \cdot [Z_{eff}\ f(Z_{eff})]^{2/3}(\frac{I_p}{U_{loop}})^{2/3}. \tag{3.4}$$

Here the constant parameter K_t characterizes the radial profile of the electron temperature, and can be expressed (from the above equations) as

$$K_t = (\frac{R \cdot \ln\lambda}{1.923\times 10^4 \int_0^a r(\frac{T_e(r)}{T_e(0)})^{3/2}dr})^{2/3} \quad [m^{-2/3}, m], \tag{3.5}$$

Because there has not been measured the electron temperature profile on the CASTOR, we use only an approximation, Fig.6.7. The values of K_t for a few reasonable profiles are summarized in the Tab.3.2.

Our recent measurements (described in the section 5), using Langmuir probes for estimating *density* profile, have shown that the gaussian profile is close to reality on the CASTOR tokamak for the parameters A_1, A_2 written in the Tab.5.1 [4].

Estimate of $T_e(0)$ from SXR-measurements

It is based on a passive diagnostic: detection of soft X-ray (coming from the plasma column) by two SBD detectors. T_e is determined from the ratio of X-ray intensity absorptions by two different aluminium *foil absorber*. For more details see [5].

3.2.4 Plasma density (line average density $\bar{n}_e$)

The plasma density is measured on the CASTOR tokamak by a *microwave interferometer*[5], which yields total number of particles L along the central chord of the vessel:

$$L = \int_{-b}^{b} n(0,y)\ dy = 2b\bar{n}_e\ . \tag{3.6}$$

[4] we assume the profile of *temperature* and of *density* of the same form which the best we can do without the Thomson scattering measurement

[5] Ordinary wave used at $\lambda = 4.255mm$

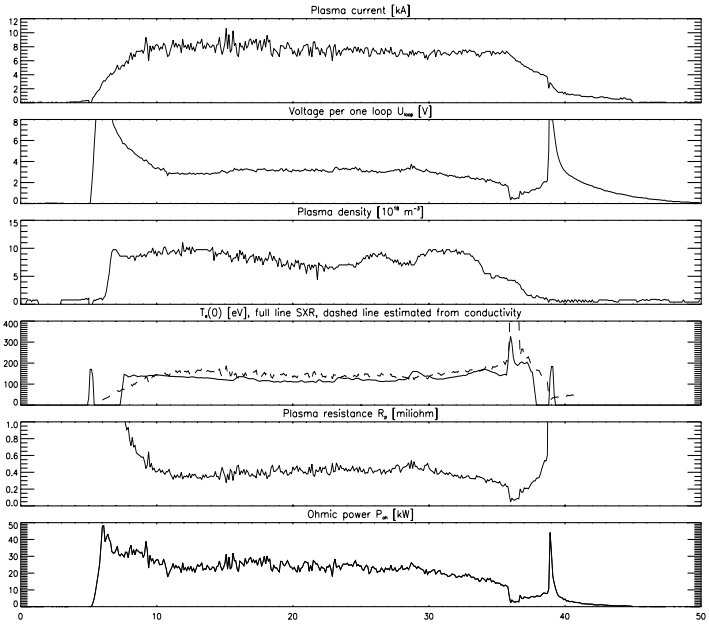

Fig. 3.2: Typical temporal evolution of plasma parameters during the shot 5908. The primary winding of transformer is short-circuited at $35\ ms$, the quasistationary phase at $\sim 10 \div 35\ ms$.

For local densities low enough $n << n_{critical} \approx 6 \times 10^{19} m^{-3}$, the relation between L and a phase shift $\Delta\gamma$ of the interferometer is:

$$L = \frac{\lambda \cdot n(\omega_0)}{\pi}\Delta\gamma, \qquad n(\omega) \equiv m\epsilon_0 e^{-2}\omega^2 \ .$$

Here $n(\omega_0)$ is the *critical* density when the *plasma* frequency ω equals the *interferometer* frequency $\omega_0 = 2\pi c/\lambda$. A signal from the interferometer U_{int} equals the phase shift $\Delta\gamma$ between the ray going through the plasma column and the reference one, going beside. Specially for the CASTOR:

$$L = 0.5205 \times 10^{18} \cdot U_{int}, \ \ U_{int} = \frac{\Delta\gamma}{2\pi} \quad [m^{-2}, V]. \tag{3.7}$$

3.3 Typical discharge regimes

Typical temporal evolutions of macroscopic parameters are shown in Fig.3.2. These are: *plasma current* I_p*, loop voltage* U_{loop}*, line-average density* $\bar{n}_e$*, central electron temperature* $T_e(0)$, *plasma resistance* $R_p = U_{loop}/I_p$ and *heating power* $P_{OH} = U_{loop}I_p$. Probe data are mostly processed in quasistationary phase of a discharge when macroscopic parameters do not change significantly.

The radial position of the plasma column is preprogrammed to regime[6] No. 3.

[6] Any displacement of the plasma column magnetic is detected by a system of ***Mirnov coils*** and, after being processed, the signal comes to a powerful system of coils that moves the plasma column back [9]. On the CASTOR we usually change the set-off of the feedback signal, so that the radial position of the plasma column is permanently shifted. There are five standard pre-programmed positions of the plasma column.

Chapter 4

Langmuir probes on CASTOR

The local plasma parameters are measured either by a swingable probe[1] or by probe arrays, both schematically shown in Fig.4.1.

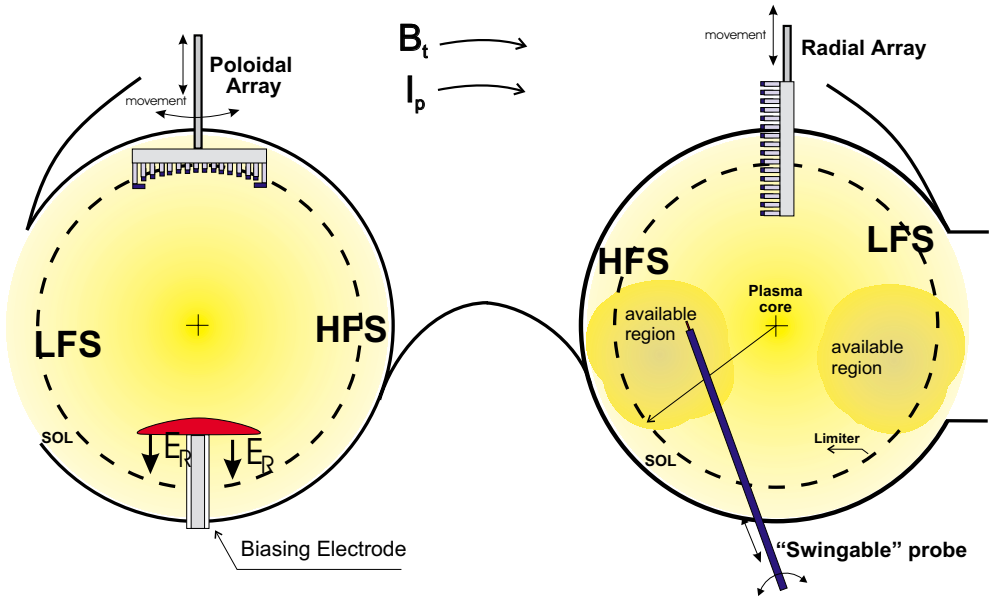

Fig. 4.1: Experimental layout of the Langmuir probes on the CASTOR tokamak. Both the poloidal and radial probe array has 16 tips with mutual distance of 2.5 mm.

Swingable arm of probes The swingable probe consists of arm which can be declined and moved radially, so that the tips can be arranged into any place of the poloidal cross-section. In practise one can measure only in the part of poloidal cross-section with $r/a > 0.4$. Placing the arm deeper into the plasma core *disturbs* already the discharge.

The arm carries two pins of Langmuir probe, the first tip operates in the floating potential mode, the second one measures the ion saturation current. Fig.4.2 shows the electric circuit for measurement of these quantities.

The floating potential is measured by the voltage divider $\sim 1/200$. The ion saturation current is measured by biasing the tip to the voltage -85 V.

[1] Basics of the Langmuir probes theory is described briefly in Appendix C.1.

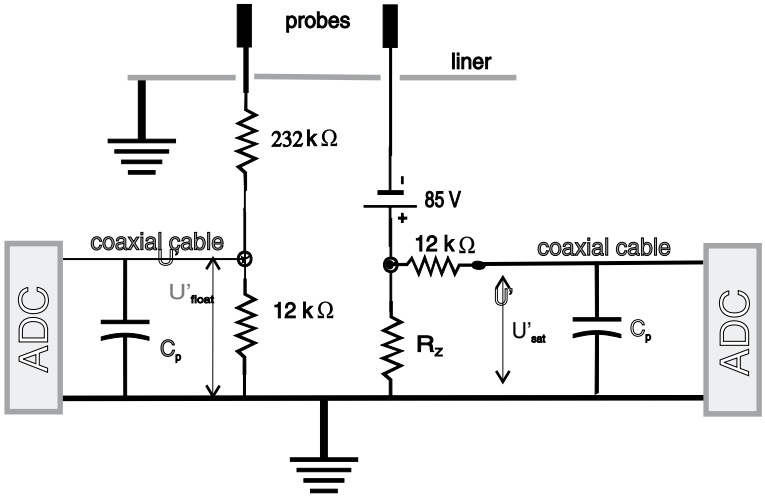

Fig. 4.2: Electric circuit for V_{fl} and I_{sat} measurement by the swingable probe. $R_z = 10$ or $100\ \Omega$.

It is necessary for fluctuation measurements that both the signals are monitored in the same frequency range which is defined by the time constants of the R-C circuit for V_{fl}-measurements $\tau = C_p \cdot 12\ k\Omega \approx 2.4\mu s$, where $C_p \approx 200pF$ is a parasitic capacitance of a coaxial cable. Therefore we inserted additional resistance ($12k\Omega$) to the I_{sat}-circuit. The frequency band is therefore $(0 \div 450)kHz$, where the upper limit is lower than the *Nyquist frequency*, which is equal $f_{Nyquist} = \frac{1}{2f_s} = 500kHz$.

The signals I_{sat} and V_{fl} are processed by an analog-digital convertor (ADC), sampling $f_s = 1\mu s$.

Poloidal and radial array of probes The local plasma parameters are monitored by a poloidal and a radial array of 16 Langmuir probes spaced by 2.5 mm, see photos in Fig.4.3.

The radial position of the probe arrays can be changed on a shot-to-shot basis. The poloidal probe array can be, if necessary, inclined poloidally by $\pm 25^o$ to adjust all the tips along a single magnetic surface. The respective position of the poloidal probe array and a magnetic surface is checked by measuring the profile of the time averaged floating potential along the probe array.

Any tip can measure either the ion saturation current or the floating potential. The electric circuit allowing to switch between shots the mode of operation is shown in Fig.4.4.

The frequency band of fluctuations measurements is 1.5 - 150 kHz in this particular case.

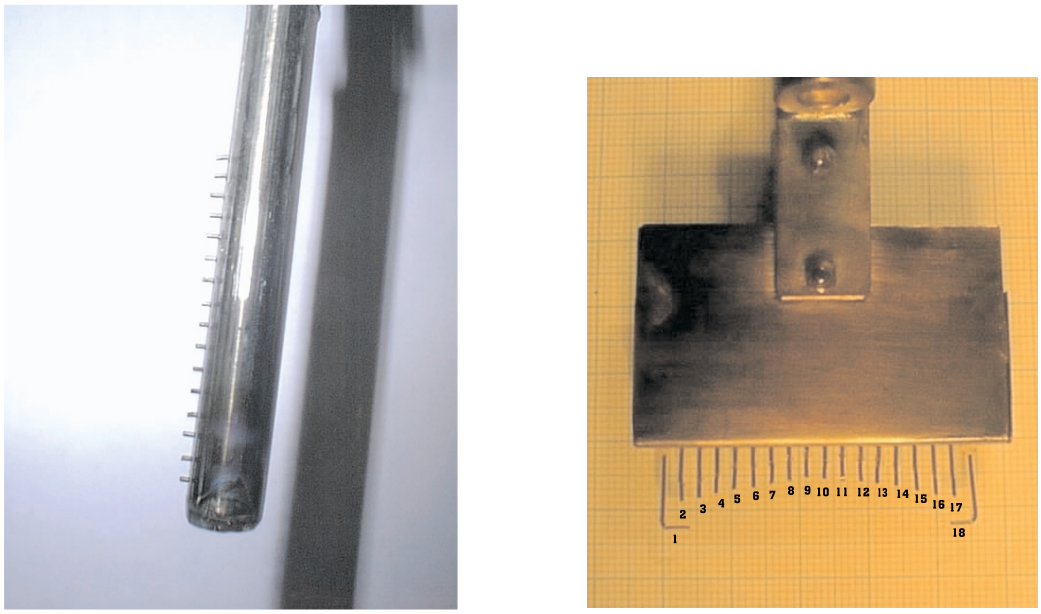

Fig. 4.3: **a)** radial probe array (37.5 mm long) consists of 16 tips spaced by 2.5 mm, each tip is 2 mm long and 0.6 mm in diameter (220^0), the probe head is covered by quartz tube to avoid short-circuiting of the radial electric field within the plasma; **b)** poloidal probe array (42.5 mm wide) has 18 tips, spaced also by 2.5 mm, the conductive part of each tip is again 2 mm (40^0).

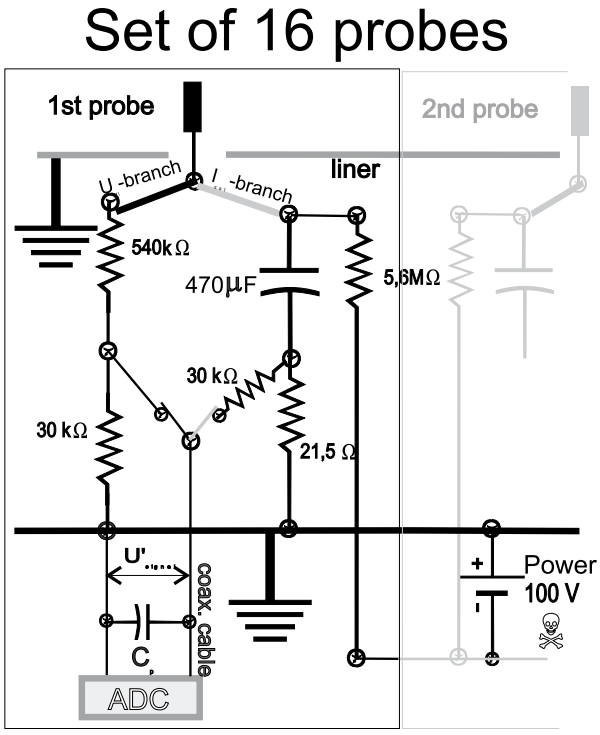

Fig. 4.4: Electric circuit of the probe arrays of 16 tips.

Chapter 5

Radial profile of plasma density

5.1 Introduction

The radial profiles of plasma density have never been measured on the CASTOR tokamak till now. The only, but routine information on the plasma density, is its line average value measured by the microwave interferometer, see section 3.2.4.

We report here the spatially resolved measurements of the plasma density derived from the single Langmuir probe mounted on the swingable arm, Fig.4.1 which allows us to measure at the low as well as at the high field sides of the torus, see Fig.5.1. Consequently, a possible asymmetry of the density profile can be deduced by this way.

The measurement has been performed in a part of the poloidal cross-section, as evident from Fig.5.1

Arrangement of this experiment is described in section 4.

5.2 Results of measurements

The local electron density is calculated from I_{sat} using Eq.(C.4). Probe active area was taken as a surface of a cylinder $A = 2\pi\rho l$, where ρ is radius and l is length of the probe tip. The resulting radial profiles of plasma density are shown in the upper windows of Fig.5.2. Filled circles correspond to n_e when the macroscopic parameters (U_{loop}, $\bar{n}_e$) were approximately the same as in discharges when the probe is withdrawn from the plasma. The *empty* circles denote the remaining disturbed discharges. *The only filled circles were taken for further processing.*

Is is seen that the radial profile is not symmetric, the maximum is shifted in the direction of the major radius R. It is also evident that usual assumption of parabolic profile is not suitable. So we use a *gaussian approximation*:

$$n(x, y) = n_{max} e^{-[(x-A_1)^2+y^2]/A_2^2}, \tag{5.1}$$

where (x, y) both move in poloidal plane (Fig.4.1) and $n_{max} \stackrel{\text{def}}{=} n(A_1, 0)$. For regime No. 3, set before, there are the parameters of density profile computed in Tab.5.1.

The shift of the plasma column is also visible from another diagnostics: Fig.5.3a) shows the radial profiles of plasma radiation in spectral line H_α taken by *vertically* oriented CCD camera.

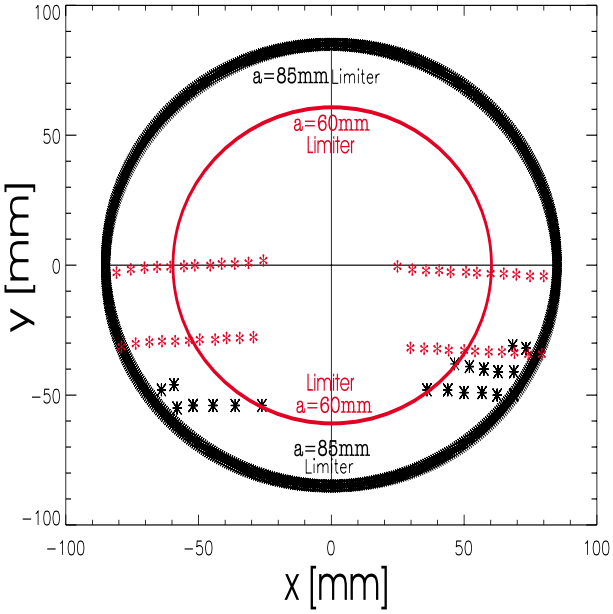

Fig. 5.1: Stars show places of the swingable probe measurement in poloidal cross-section. Red stars for $\#4541 - 4586,\ a = 60mm$, black stars for $\#6084 - 6140,\ a = 85mm$.

	$a = 85mm$	$a = 60mm$
A_1/a	0.37 ± 0.03	0.32 ± 0.02
A_2/a	0.64 ± 0.02	0.67 ± 0.01
$n_{max}[10^{18}m^{-3}]$	15.8 ± 1.2	21.6 ± 1.2

Table 5.1: Parameters of gaussian profile for regime No. 3. The errors ($\pm$) does not contain the uncertainty of the points cut-off (i.e. dividing measured points of Fig.5.2 into groups of filled/empty circles) which was done "by eye" !

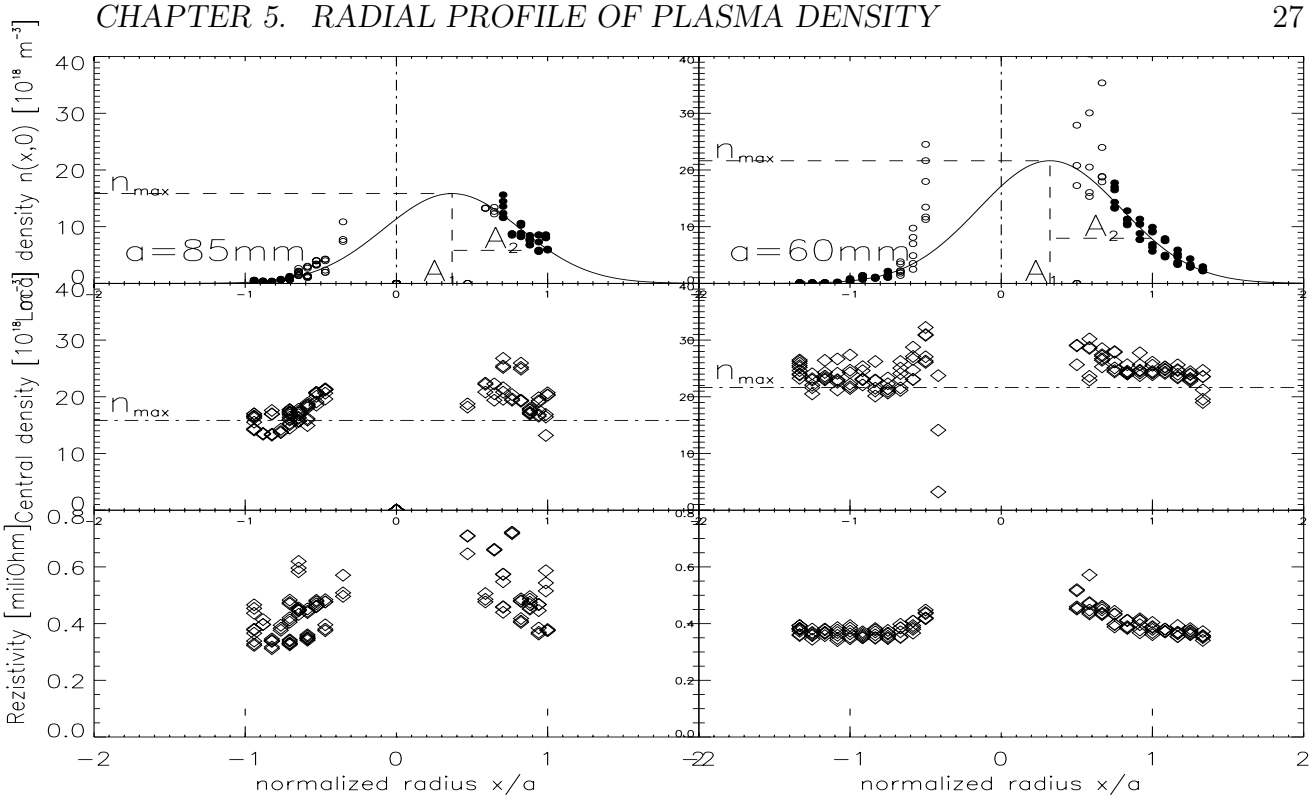

a) $a = 85mm$ **b)** $a = 60mm$

Fig. 5.2: The **Top windows:** Radial profiles of local plasma density estimated from $I_{sat}-$measurement. The gaussian fit (Eq.(5.1)) was counted only with the discharges marked by the **filled** circles when the plasma was not too perturbed, as one can see in Fig.6.2 (I_{sat},T_e) and in the **Middle windows** of *central density* and the **Bottom windows** of the total plasma column *resistance*.

The same profile taken by *horizontally* oriented camera is in Fig.5.3b). Its symmetry allows us to use the approximation Eq.(5.1) (meaning the profile depends only on radius $\sqrt{(x-A_1)^2+y^2}$).

Estimation of maximum density n_{max}

There is a famous problem with Langmuir probes: it is not clear (especially in a magnetized plasma) what exactly is the *probe active area* A, see Eq.(C.4). Assuming $T_i = T_e$ we can compare the signal from the interferometer with the probe measurements, assuming the gaussian profile (Eq.(5.1)), too:

The signal U_{int} from the interferometer equals L - the number of particles along the path of the microwave beam, see Eq.(3.6). So we are to integrate Eq.(5.1) along a central vertical chord $x = 0$:

$$L = \int_{-b}^{b} n(0,y)dy = n_{max}e^{-A_1^2/A_2^2}\int_{-b}^{b} e^{-y^2/A_2^2}dy =$$

$$= n_{max}\cdot\sqrt{\pi}A_2\; e^{-A_1^2/A_2^2}errf(b/A_2),$$

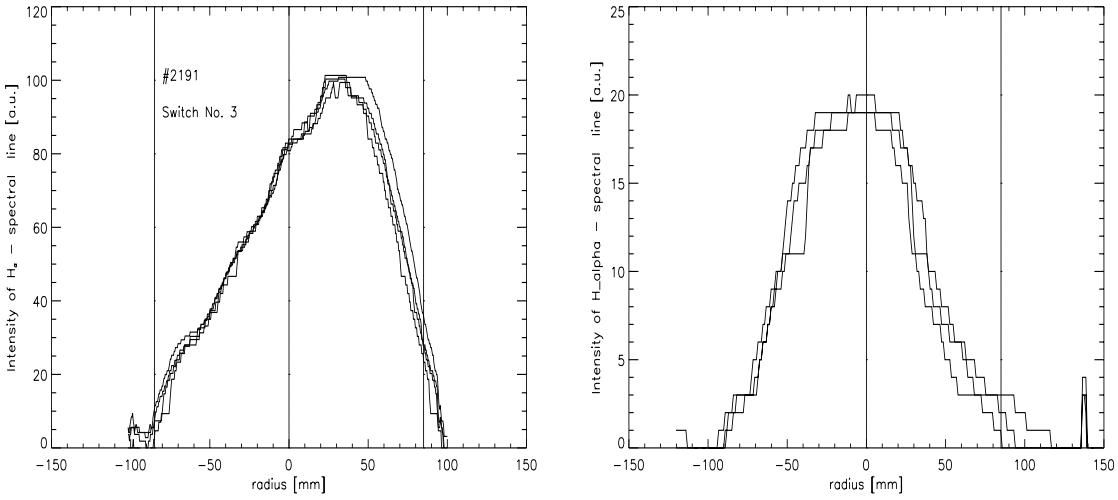

Fig. 5.3: **a) Vertical** and **b) horizontal** profile of plasma radiation at spectral line H_α, taken by the CCD camera.

where $err\,f$ is the *error function*[1]. Using now Eq.(3.7) we get the relation between n_{max} and the output signal from the interferometer U_{int}:

$$n_{max} = K_{max} \cdot U_{int} \tag{5.2}$$
$$K^{60}_{max} = 9.18 \times 10^{18} m^{-3}/V \; for \; limiter \; a = 60mm \tag{5.3}$$
$$K^{85}_{max} = 7.31 \times 10^{18} m^{-3}/V \; for \; limiter \; a = 85mm, \tag{5.4}$$

where K_{max} is the computed calibration factor.

Values of n_{max}, counted by this way (using the **interferometer** signal), are shown in the middle windows of Fig.5.2. In the same figure one can also see the n_{max} estimated (by gaussian approximation) from Langmuir **probes** measurements, marked by a dashed-dotted line. This coherence ensures us that the counting method of the active probe area A was right, although it is usually assumed the area equals the double of the area of the probe projection perpendicular to the magnetic field line.

Estimating line average density $\bar{n}_e$

The plasma is mostly characterized by the "line average density $\bar{n}_e$" parameter, which is usually defined (for symmetrical profiles) as:

$$\bar{n}_e = \frac{1}{2a} \int_{-a}^{a} n(r) dr.$$

For a asymmetrical profile we **define "line average density $\bar{n}_e$"** generally as a mean density over a central horizontal chord:

$$\bar{n}_e(\zeta) = \frac{1}{2\zeta} \int_{-\zeta}^{\zeta} n(x, 0) dx.$$

[1] defined at Tab.D

Using again the Eq.(5.1) and integrating it we get:

$$\bar{n}_e = n_{max}\frac{\sqrt{\pi}A_2}{4\zeta}[erf(\frac{\zeta - A_1}{A_2}) + erf(\frac{\zeta + A_1}{A_2})], \tag{5.5}$$

Taking now Eq.(5.2) for n_{max} we finally get a relation between the mean density (resp. $\bar{n}_e$) and the interferometer signal L:

$$\bar{n}_e = K_{aver}(\zeta)U_{int} \tag{5.6}$$

$$\begin{array}{l} K^{60}_{aver}(\zeta = b) = 3.26 \times 10^{18} m^{-3}V^{-1} \text{ for } a = 60mm \\ K^{85}_{aver}(\zeta = b) = 3.39 \times 10^{18} m^{-3}V^{-1} \text{ for } a = 85mm \\ K^{60}_{aver}(\zeta = a) = 5.02 \times 10^{18} m^{-3}V^{-1} \text{ for } a = 60mm \\ K^{85}_{aver}(\zeta = a) = 3.82 \times 10^{18} m^{-3}V^{-1} \text{ for } a = 85mm, \end{array}$$

where K_{aver} is a computed calibration factor.

Mind this $\bar{n}_e$ does not depend on the profile (whether it is gaussian or parabolic or etc...).

Chapter 6

Electrostatic fluctuations at High and Low field side

6.1 Introduction

High diffusion casualties of particles and energy from tokamak plasma are undesirable. The magnetic surfaces are convex at the low field side (shortly LFS) and so MHD unstable [25]. So we expect density fluctuation level $\tilde{n}$ (directly proportional to ion saturation current I_{sat}) and plasma potential $\tilde{\phi}$ to be lower at HFS (in comparison to LFS). By the *model of eddies*, any arbitrary local fluctuation $\tilde{\phi}$ raises particle radial transport off plasma [21].

Arrangement of this experiment is described in Section 4.

6.1.1 Electrostatic plasma fluctuations

- Local parameters of tokamak plasma are not stationary but they fluctuate around their *mean values*. In this work we are focused on the electrostatic fluctuations, i.e. fluctuations of plasma density $I_{sat} \propto n_e$ and plasma potential $V_{fl} \propto \phi$.
- It is claimed these fluctuations are responsible for *anomalously* high loss of particles. Let toroidal magnetic field $\vec{B}_t$, plasma density n and poloidal electric field $\vec{E}_p$ be:

  $$n(t) =< n > +\tilde{n}(t) \qquad E_p(t) =< E_p > +\tilde{E}_p(t) \;\text{ and also }\; < E_p > \simeq 0,\; \vec{B}_t \perp \vec{E}_p,$$

  The symbols $< q >$ resp. $\tilde{q}$ signifies *in time mean value* and a *fluctuating component* of a quantity q, respectively.

  The *radial particle flux* $\vec{\Gamma}$ induced by drift of particles in the crossed fields is [2, p. 35]:

  $$\vec{\Gamma}(t) = n\vec{v}_{radial} = n(t)\frac{\vec{E}(t) \times \vec{B}}{B^2} = \vec{e}_r n E_p/B_t =$$

  $$= \vec{e}_r(< n > +\tilde{n})\tilde{E}_p/B_t,$$

  $$< \vec{\Gamma} >= \frac{< \tilde{n}(t)\tilde{E}_p(t) >}{B_t}\vec{e}_r,$$

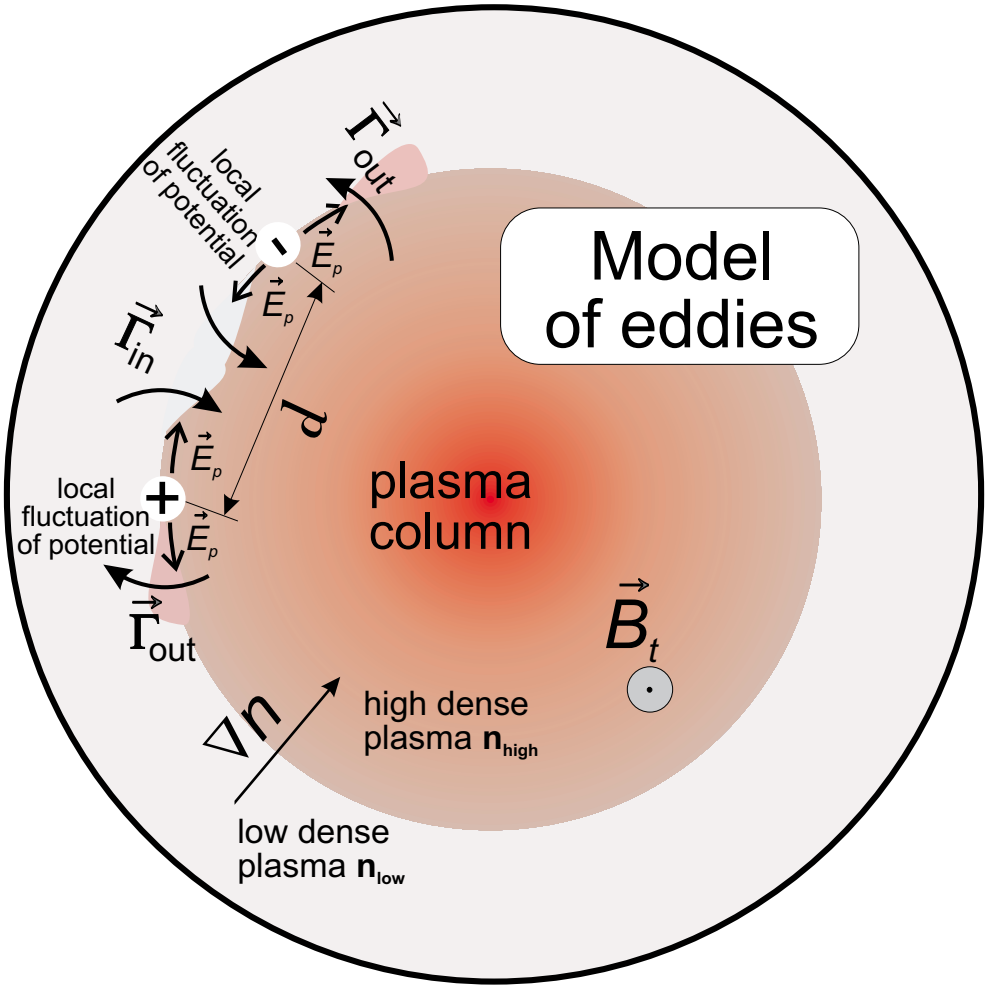

Fig. 6.1: Mechanism of origin of eddies in a plasma column with radial density gradient (schematically).

where $\vec{E_p} = -\frac{d\phi}{rd\Theta}$, and $\vec{e_r}$ is a radial outward unit vector. This so called *fluctuation induced flux* can be also expressed forwardly:

$$< \Gamma >= C_{n,E_p}\sqrt{< \tilde{n}^2 >}\sqrt{< \tilde{E}_p^2 >}/B_t \tag{6.1}$$

where Θ is poloidal angle and $C_{n,E_p} \in (-1,+1)$ is a *correlation coefficient between density and poloidal electric field fluctuations.*

- There has been proposed a model showing coherence between density and poloidal el. field fluctuations (*model of eddies*) in [21]. By this model these quantities are in phase and so the coefficient of correlation is positive ($C_{n,E_p} > 0$). The model is described in the following:

  Let us suppose there appears some local extrema of potential (in Fig.6.1 marked as +). Then original poloidal el. field causes mixture of close areas of plasma due existence of $\vec{E_p} \times \vec{B_t}$ drift. There are, afterwards, particle fluxes off the plasma column:

$$\Gamma_{in} = -v_r n_{low} \; ; \;\; \Gamma_{out} = +v_r n_{high}$$

$$\Gamma_{net} = \Gamma_{in} + \Gamma_{out} = v_r(n_{high} - n_{low}) > 0,$$

Any arbitrary local fluctuation of plasma potential raises then radial transport of particles out of plasma column.

There are also observed fluctuations *periodical* in poloidal direction with a characteristic wave-length $d \approx 10 - 15cm$, depicted in Fig.6.1.

- Now the question is how these *fluctuations* originate? One mechanism of their origin in SOL proposed in work [25] is as following:

  The plasma surface at LFS is convex and therefore unstable (due to the *MHD-instability* [1, chap. 6.1], [3, chap. 9], [25]) unlike the HFS. Due the instability we expect that level of electrostatic fluctuations will be *lower at HFS*.

So the main destination of this work is to compare levels of fluctuations of plasma potential and density in SOL at HFS and LFS by the single Langmuir probes. Construction of our probes and also parameters of plasma enabled us to measure radial profiles of $n,\ \tilde{n},\ \phi,\ \tilde{\phi}$.

6.2 Results

6.2.1 Radial profiles of (fluctuations of) I_{sat}, V_{fl}

From raw data we have estimated mean values and level of fluctuations in different times and different places in the plasma, see Fig.6.2. Central electron temperature $T_e(0)$ counted from plasma conductivity (Eq.(3.4)) and local density from I_{sat} (Eq.(C.4)). In the case of $a = 60mm$ the central T_e is higher because the plasma volume is smaller and the ohmic input power $P_\Omega = I_p V_{loop}$ stays about constant.

6.2.2 Frequency analysis of signals

Measuring *magnetic fluctuations* there are observed magnetic structures, rotating in poloidal plane, so called *magnetic islands*. They are also in the CASTOR, see [4, chap. 2.1]. The next destination of this work was to try to identify them by our Langmuir probes: If getting into such an island we expect periodical changing of probe signals. So, we applicated *the Fourier transform* on both signals V_{fl} and I_{sat}.

There were not found any dominant frequency in both these signals, it means *magnetic islands were not observed*. In work (e.g. [4]) islands with $q = 2$ were observed.

There one can see used function of the $q - factor$ in Fig.6.3. Whether $q(r) = 1$, or 2, or 3,.., for some special radius r, there can origin the islands. We have found some little suggestions of existing of any dominant frequency in a few shots: for $q = 3, r = (39 \pm 3mm), f \approx 95kHz$. We have chosen the more conspicuous shot - see Fig.6.4.

6.3 Discussion

Measuring I_{sat} we have found a problem: the I_{sat} value we measured as probe current I when biased at -85 V. This is correct if local temperature is low enough, but when moving the probe

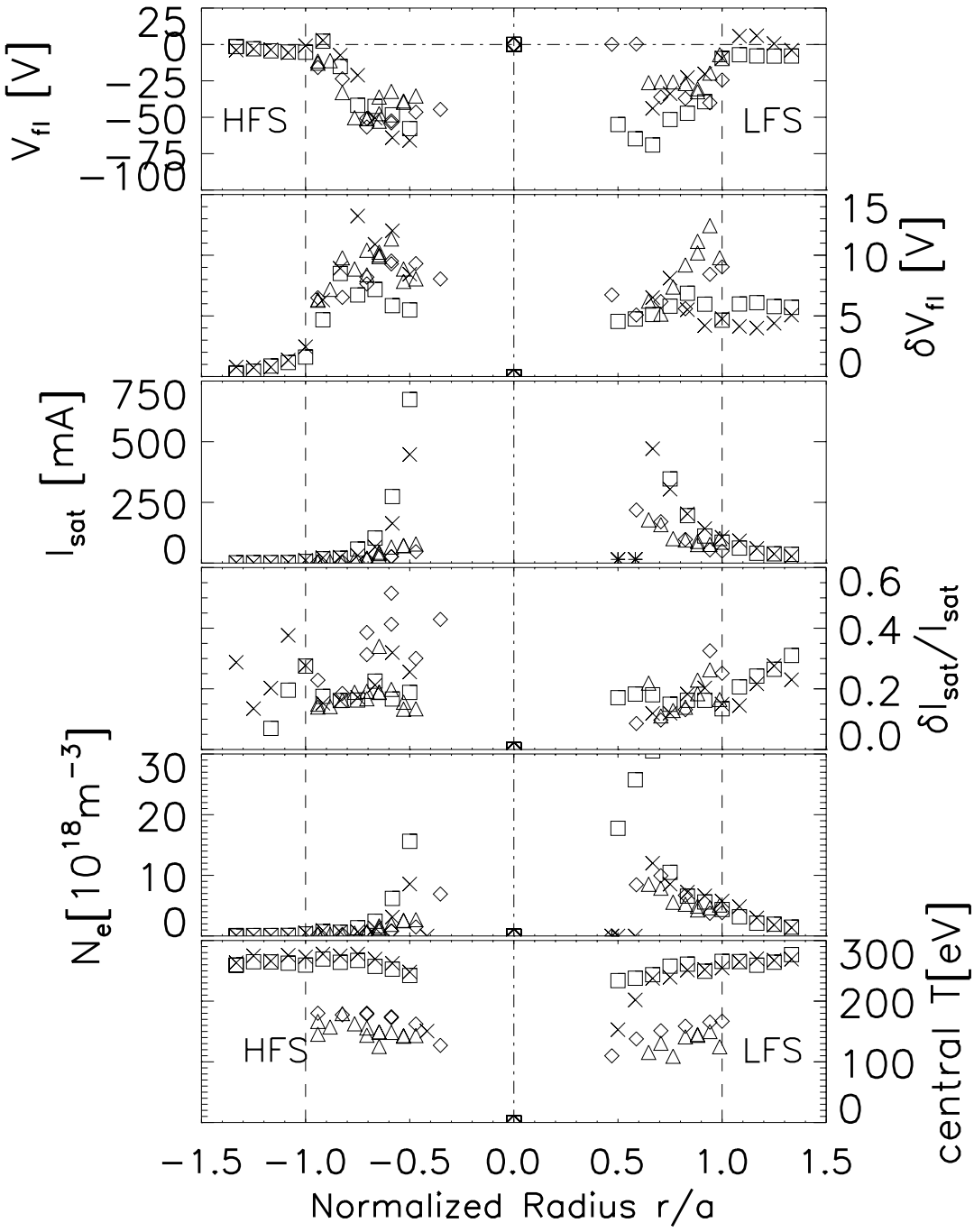

Fig. 6.2: Radial profiles (of fluctuations) at HFS and LFS. Some points at zero values are mistakes due to data-processing.

limiter radius	a=60mm	a=85mm
at equatorial plane	×	△
about 30mm below it	□	◇

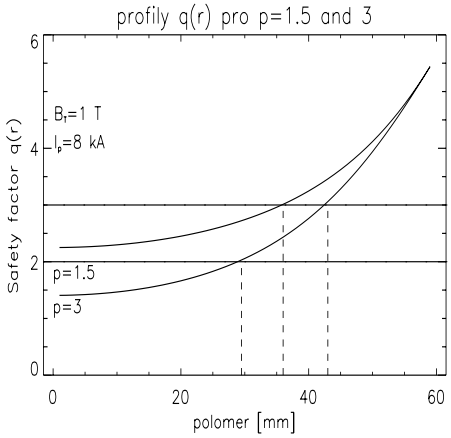

Fig. 6.3: Expected profile of the q-factor. This was counted with assumption that plasma current radial profile $I_p(r)$ is parabolic.

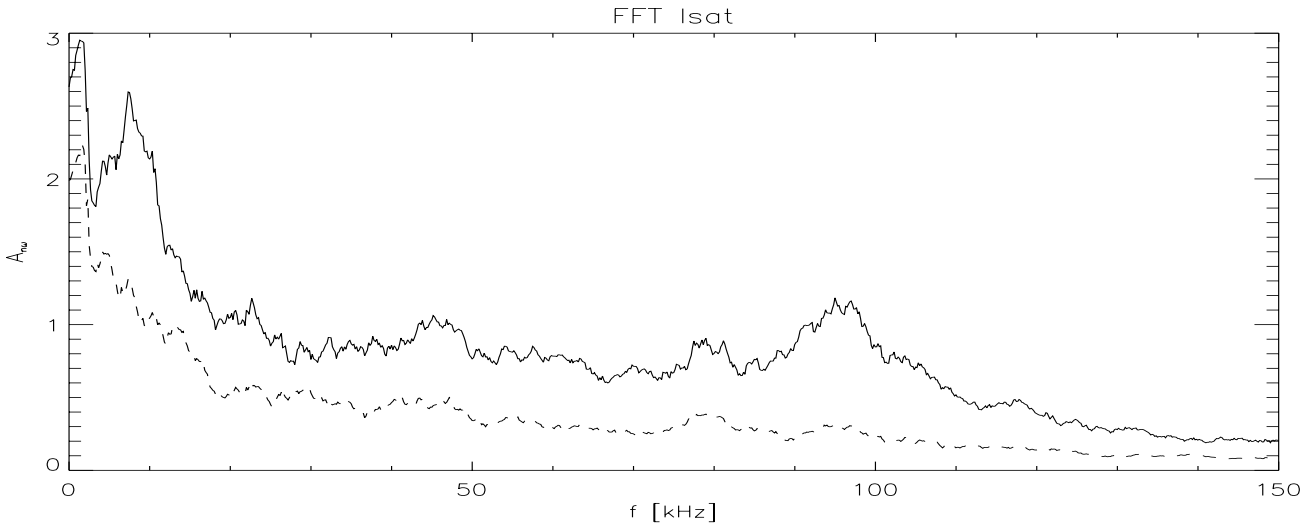

Fig. 6.4: The Fourier transform of the signals

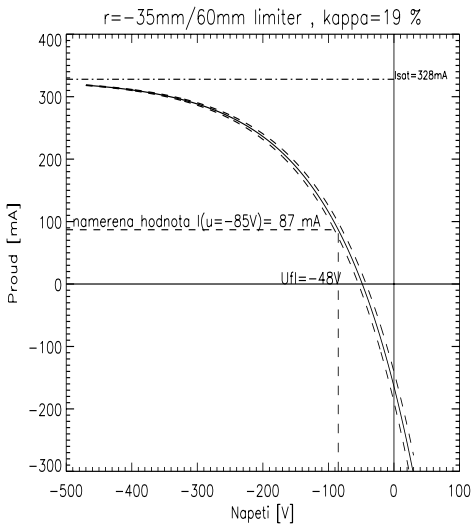

Fig. 6.5: V-I characteristics, wrong measurement

to the center T_e is raising and the value of $I_{(V_{appl}=-85V)}$ gets far away from I_{sat}(see Fig.6.5) and also the correlation between I_{sat} and V_{fl} is influenced. This problem is discussed in the two following sections.

6.3.1 Possible error in I_{sat}-measurement

The introduced wrong-measurement can be eliminated when knowing the temperature profile. Because it is not known, we approximate it by [5, p. 54]:

$$T_e(r) = T_e(0)(1 - (\frac{r}{a})^2)^2 \tag{6.2}$$

Two points of the profile we know: in the center from the conductivity Eq.(3.4) and in SOL measured in many ways, so we take $T_e(r \geq a) = 16eV$.

How to eliminate the mistake? Look at Fig.6.5. Using Eq.(C.1) let us write:

$$I_{sat} = \frac{I_{(U=-85V)}(t)}{1 - exp(\frac{-85V - V_{fl}(t)}{T_e})} = K(V_{fl}(t), T_e)^{-1} \cdot I_{(U=-85V)}(t),$$

where $I_{(U=-85V)}(t)$ is the measured signal. In the first approximation we have used

$$K = 1 - exp(\frac{-85V - < V_{fl} >}{T_e}) = constant\ in\ time.$$

This correction constant enlarges I_{sat}up to $4\times$ and so the same the local plasma density n_e. **All the I_{sat} values have been computed in this way!**

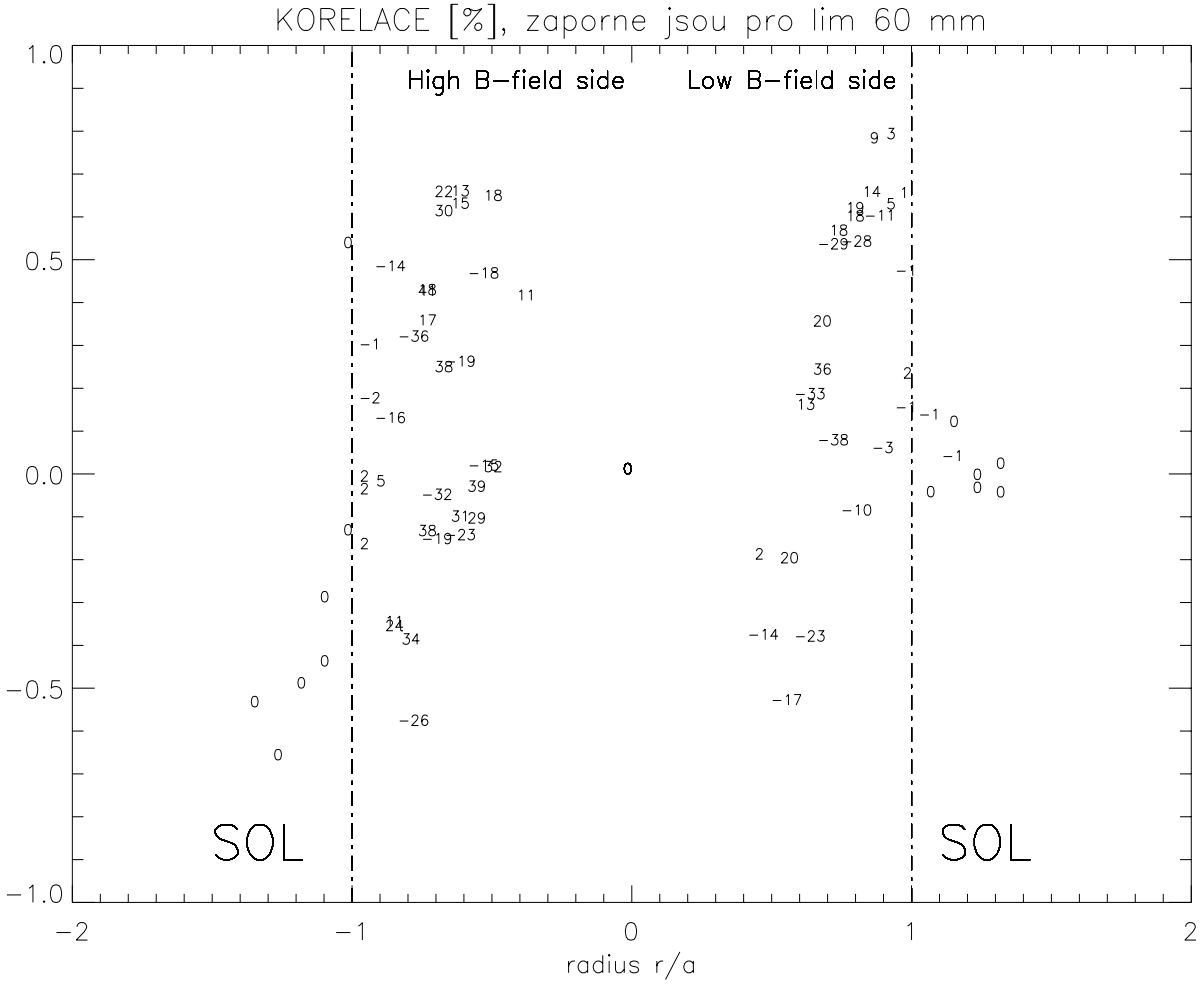

Fig. 6.6: Correlation of local quantities V_{fl} and I_{sat}. The numbers mean the coefficients $\pm\kappa$ in percent, negatively marked are the ones measured with limiter $60mm$.

6.3.2 In time correlation of local quantities V_{fl} and I_{sat}

Look at Fig.6.6. There are drawn measured values of correlation between the signals of V_{fl} and I_{sat} as a function of probe position, its radius r. It is wondering, sometimes, how high the correlation is.

But : because of the bad measurement of I_{sat} (taken equals $I_{(U=-85V)}$), the positive correlation is partly affected by this way (see Fig.6.5):

$\tilde{V}_{fl}$ fluctuations around its mean value $< V_{fl} >$ mean *moving* of the V-I characteristics left and right at the 'voltage axis', and so the value of probe current at voltage $-85V$ fluctuates, too. This is a parasitic fluctuation and causes a parasite positive correlation !

How big the influence is?

Let us take SD of potential $\sqrt{< \tilde{V}_{fl}^2 >} \approx 1 \div 10V$ as mean amplitude of potential. Then, using Eq.(C.1), we estimate *part* fluctuations of ion saturation current $\tilde{I}_{sat}$ taken as $\tilde{I}_{(U=-85V)}(V_{fl}(t))$. Let us define a coefficient of this effect κ:

$$\kappa = \frac{\tilde{I}_{(U=-85V)}}{\sqrt{< \Delta I_{sat}^2 >}}$$

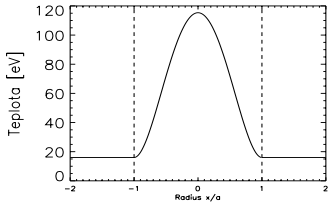

Fig. 6.7: The temperature profile approximation

The numbers in the Fig.6.6 are the coefficients κ for all shots. It is clear that the deeper we are in plasma the higher the influence is.

6.3.3 Conclusions

- Central electron temperature $T_e(0)$-profile shows that the swingable arm *cools* the plasma if placed deeper. The case with $a = 60mm$ the plasma is hotter because the volume is smaller while the ohmic input power stays constant.
- V_{fl}-profile is as expected, compare e.g. with Fig.8.2a) measured at LFS.
- potential fluctuation $\sqrt{< \tilde{V}_{fl}^2 >}$-profile shows *clear difference* between HFS and LFS by a factor of 4-10 ! Is this the expected verification of the model of the *MHD-instability* [25] at convex surfaces ? However, density fluctuations $\tilde{I}_{sat}/I_{sat}$ does not show difference between LFS and HFS.

However, this measurement should be performed again with higher voltage at ion saturation current[1] and using swingable probe with *two* floating pins distanced poloidally and one saturated[2]. This configuration would allow us to measure the desired *fluctuation induced flux* Γ_r. Then this measurement would be really interesting and suitable to be written as a paper.

[1] to eliminate the wrong measurement (see Sec. 6.3.1)

[2] unsuccessful measurement has already been performed, shots 9443-9484

Chapter 7

Solution of 1/2 puzzle

7.1 Fluctuation-induced flux

Jan Petržílka has published in his PhD-thesis [8] the "1/2 Puzzle" which consists from the following:

Using the poloidal array of the Langmuir probe V_{fl} and I_{sat} were measured alternately. In the perpendicular magnetic and electric field ($\vec{E}_p \perp \vec{B}_t$) appears the well-known $E \times B$–drift in the radial direction:

$$\vec{v} = \frac{\vec{E} \times \vec{B}}{B^2}.$$

Multiplicating this velocity by local plasma density n_e one gets the radial $E \times B$–flux.

$$\vec{\Gamma} = n \cdot E_{pol}/B_{tor} = \frac{const \cdot I_{sat} \cdot (U_{fl}^{(1)} - U_{fl}^{(2)})}{B \cdot d},$$

where $E_{pol} = (U_{fl}^{(1)} - U_{fl}^{(2)})/d$ and d is the distance between poloidally separated probes 1 and 2.

Being interested only in the *fluctuating part* of the induced flux we get a similar formula for estimating the radial particle flux

$$\Gamma \equiv \Gamma_r = \frac{const \cdot \tilde{I}_{sat} \cdot (\tilde{U}_{fl}^{(1)} - \tilde{U}_{fl}^{(2)})}{B \cdot d}, \tag{7.1}$$

where $\tilde{q}$ means fluctuating part of a quantity q, i.e. $< \tilde{(q)} > \equiv 0$.

There was empirically found in the cited work [8] that the mean value of the fluctuation induced flux goes outwards and poloidal electric field and density are correlated of about $0.5 - 0.7$, nothing surprising, but:

The 1/2 puzzle consisted just in the following:

By chance it was found during the analysis that the radial outflux fulfils such a law:

Ratio of time when the outflux is higher than its mean value ($\Gamma > \bar{\Gamma}$) and time when the outflux is (in contrary) lower is just equal 1/2:

$$P = \frac{T_{\Gamma > \bar{\Gamma}}}{T_{\Gamma < \bar{\Gamma}}} \approx 1/2. \tag{7.2}$$

This value $P \approx 1/2$ was found to be constant in *any* plasma condition, tested on ≈ 150 different shots.

It seemed to be a puzzle and the author expected there might be some hidden interesting physics in it.

We have focussed on this puzzle and found that it is just a *statistical law* with *no "magic" physics* inside, that is described in the following section.

7.2 Solution

Let us generate two random variables $I_{sat}(t), E_p(t)$ (i.e. density and poloidal electric field) both with normal distribution. Then compute, from these variables, the radial fluctuation induced particle flux from Eq.(7.1). When they are *not correlated*, the ratio (from Eq.(7.2)) $P = 1$, i.e. number of points *above* and *below* the mean value are *equal*. In the case of total correlation it is clear the ratio P has to decrease[1].

There is shown in Fig.7.2 the ratio P dependence on the correlation which we got by **computer simulation**.

Because measured correlation between E_{pol}, n_e lies in region 0.5–0.7, the corresponding value of the ratio (Fig.7.2) is $P = 0.5 \pm 0.1$. This is just the *solution of the 1/2 puzzle*.

How much the *measured* signal PDF is *close* to normal distribution ? The answer is shown in Fig.7.1 where the *measured* and *generated* signals are compared; one can see they are very close. In work [28] the PDF of measured signals is discussed in more detail.

7.3 Conclusion

The ratio $P \approx 1/2$ does not have any "magical" meaning concerning the fluctuation induced particle outflux *because* it is just only a *statistical law* that two normally distributed variables with correlation higher than $\approx 20\%$ give (after multiplication) the ratio P of about 1/2.

Mind, however, that the flux does really behave in this way (the ExB contribution to the total outflux is dominant); if we measured it by another (direct) method I expect to get the same behaviour but in this case we did not likely understand the reasons.

[1] Here one has got square of a normally distributed variable. Its distribution surely vanishes for $\Gamma < 0$ because square is always positive.

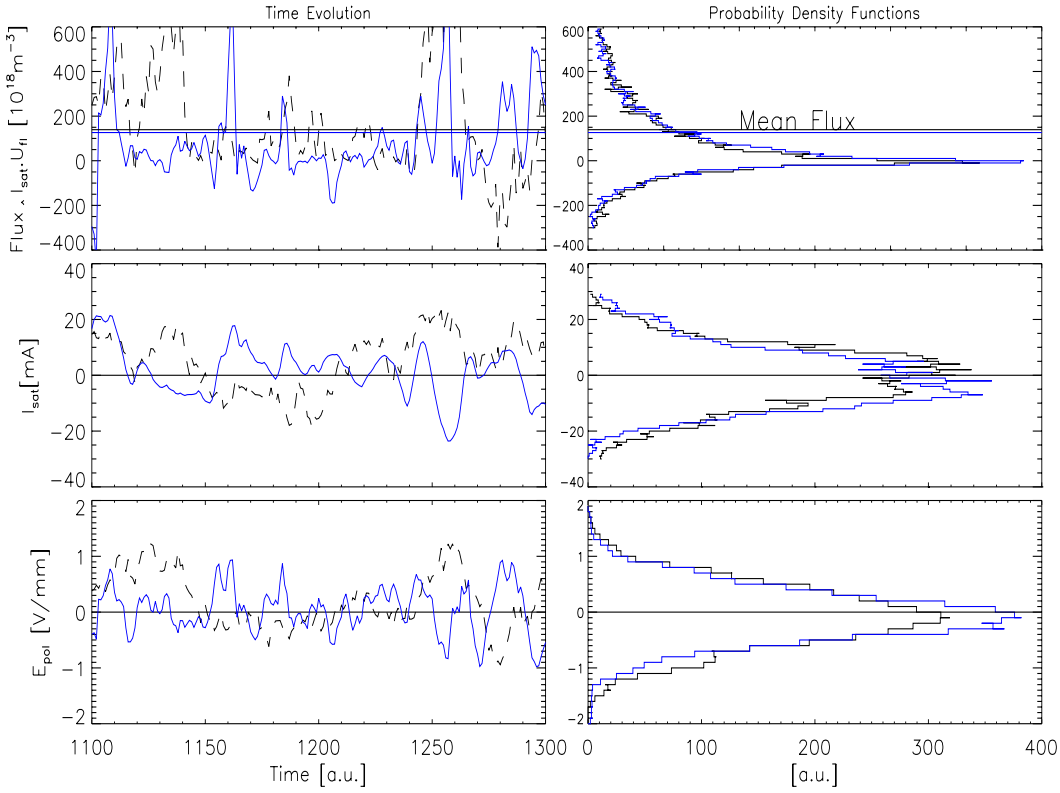

Fig. 7.1: Comparison of the randomly **generated** I_{sat} and E_{pol} with the **measured** data and also the **outflux** Γ_r computed from both the generated and measured data. The ratio P can be estimated from the top right figure as a ratio of areas above / below the mean value.

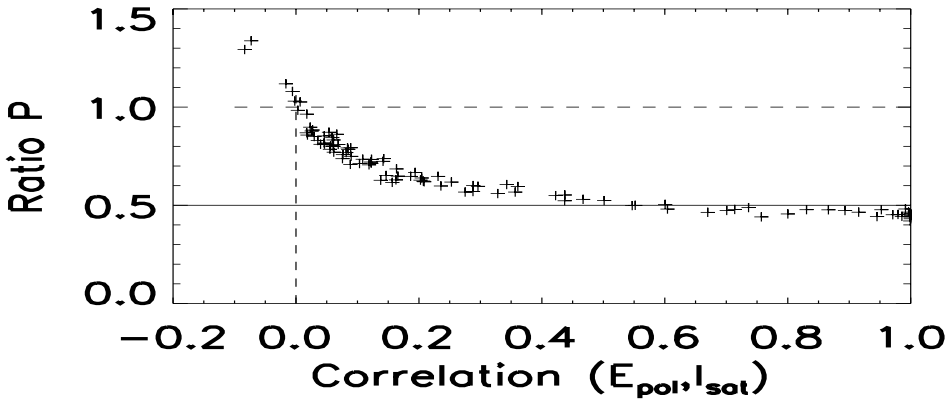

Fig. 7.2: Numerically computed dependence of the ratio P as a function of correlation between I_{sat} and E_{pol}.

Chapter 8

Edge turbulence at plasma polarization

8.1 Introduction

Electrostatic turbulence is responsible for anomalous particle and heat losses from tokamak plasmas. The equilibrium level of plasma fluctuations is determined by competition of the *growth rate* γ and the *damping rate* ω of the most unstable modes.

The fluctuation growth rate is hardly to be deduced theoretically, namely at the plasma edge, where various models of the core and scrape-off layer turbulence overlap. A reasonable lower estimate of γ can be found from the *autocorrelation time of fluctuations* τ_A that can be easily derived from experimental data, $\gamma > 1/\tau_A$ [11].

On the other hand *turbulence is damped by sheared plasma flows* that are believed to be *the main mechanism behind formation of transport barriers* [12], Fig.C.5. The plasma flows are closely related to the radial electric field, $E_r = \nabla p/(en) + v_p B_T + v_T B_p$. Usually, in tokamak discharges without any additional heating, the toroidal momentum and pressure gradient terms play a minor role. Therefore, the *radial electric field is mostly linked to the poloidal flow term* $v_p B_T$. Consequently, damping of turbulent structures due to the sheared flow is characterized by the decorrelation rate $\omega_{E\times B} = dv_p/dr \approx (dE_r/dr)/B_T$. Reduction of the electrostatic turbulence can be expected if the $E \times B$ decorrelation rate prevails the growth rate γ. The described mechanism plays an essential role in the formation of edge [13] and internal [14] transport barriers as well as in tokamak regimes with edge plasma polarization (see e.g. [15],[17]).

The aim of this contribution is to study the impact of a sheared electric field on the spatial structure of edge fluctuations in the radial and poloidal directions on the CASTOR tokamak [26]. A biased electrode is used for external modification of the radial electric field in the proximity of the natural velocity shear layer (VSL).

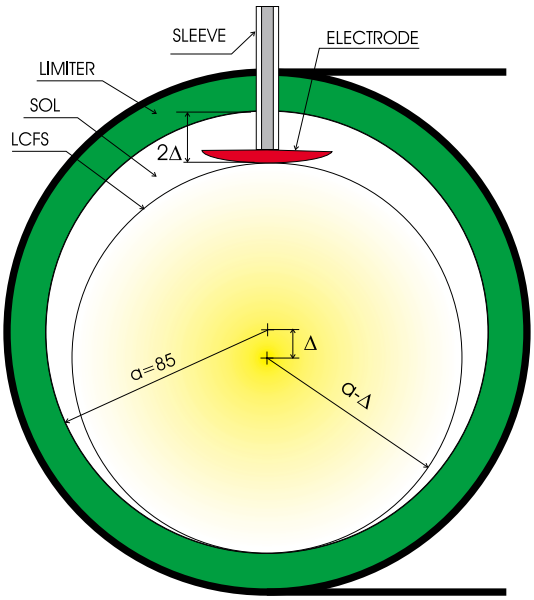

Fig. 8.1: Poloidal cross section, schematically showing the location of plasma column and biasing electrode.

8.2 Experimental arrangement

The radial electric field is imposed to the edge plasma by a mushroom-like electrode[1] biased with respect to the vacuum vessel by a voltage pulse[2]. The fluctuations are monitored using the two multiple Langmuir probes arrays oriented in the radial and poloidal directions (see chapter 4). Individual tips measure either the floating potential U_{fl} or the ion saturation current I_{sat}.

All the key elements of the biasing experiments on the CASTOR tokamak are depicted in Fig.C.4 and Fig.4.3.

The specific feature of the analyzed discharges is a downward shift of the plasma column, as schematically shown in Fig.8.1.

The minor radius of the plasma column is already not determined by the radius of the poloidal limiter, but it is reduced to $a - \Delta$. As a consequence, an additional scrape-off layer appears. Its width is 2Δ at the top of the torus. The connection length in this region is much larger than the circumference of the torus ($2\pi R$) and varies with the safety factor $q(a - \Delta)$.

The radial electric field, which is one of the basic parameters of the biasing experiment, is deduced in a single shot using the radial probe array (Section 4). The individual tips measure the floating potential, which is related to the plasma potential by Eq.(C.3) The radial electric field is estimated as the gradient of the floating potential

$$E_r = -\nabla\phi \cong -\nabla U_{fl} - 2.5 \times k\nabla T_e/e \approx -\nabla U_{fl} \ ,$$

since the edge temperature profile is rather flat on the CASTOR tokamak ($k\nabla T_e/e \sim 0.1\, V/mm$).

The vertical displacement of the plasma column is deduced from the vertical shift of the Velocity Shear Layer (VSL), defined here as the radius where $\nabla U_{fl} = 0$. Simultaneous measurements of ∇U_{fl} and propagation velocity of fluctuations in the poloidal direction show

[1] The electrode influences the plasma: V_{fl}-profile shifts a bit less as the electrode shifts, however, its shape stays unperturbed.

[2] The biasing method is explained in chap. C.4.

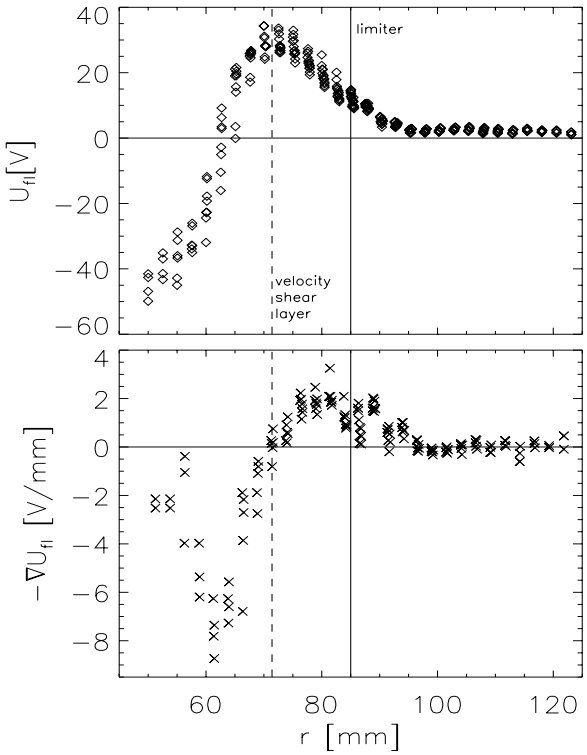

Fig. 8.2: a) Radial profile of the floating potential without biasing as measured by the radial probe array from the top of the torus. b) The gradient of the floating potential corresponds to the radial electric field: $E_r \approx -\nabla U_{fl}$. These figures consists from several shots with different radial positions of the probe; it show that the probe does not influence E_r.

that the position of the real VSL is still a few millimeters more inside the plasma column (probably because the $\nabla T_e \neq 0$). However, in this contribution we refer to the apparent position of VSL.

In the shot series shown here, the vertical displacement $\Delta = 6 \div 7\ mm$.
Due to the strong poloidal asymmetry of the scrape-off layer, the probe arrays as well as the biasing electrode are located at the top of the torus, to define better their respective radial positions. The biasing electrode is radially located in the SOL, slightly outside the natural VSL. In fact, the electrode acts as a biased limiter. The aim of this configuration is to modify the shear of the radial electric field (defined as $\frac{dE_r}{dr}$) just in the proximity of the natural VSL by positive biasing. Another practical advantage of such configuration is that the radii $r < r_B$ are accessible by the probe arrays (r_B is the distance of the electrode from the center of the vacuum chamber).

8.3 Experimental results

8.3.1 Evolution of polarized discharges

The temporal evolution of a typical discharge with positive biasing is shown in Fig.8.3. A voltage pulse is applied to the electrode during the quasistationary phase of the discharge. Typically, a current $I_B = 30 \div 40\ A$ is drawn by the electrode at $\mathrm{U_B}$=+200 V. A fraction of the return current flows to the poloidal limiter ($\sim 30\%$), the remaining part flows directly to the vessel wall. The next panel shows the evolution of the intensity of the H_α spectral line I_{H_α}, which is proportional to the influx of neutral hydrogen atoms from the chamber wall. The small increase of I_{H_α}, observed at biasing, can not explain the significant increase of the line average density observed in the experiment. At the same time, the influx of impurities remains unchanged. Therefore, we conclude that the global particle confinement improves with biasing.

Quantitatively, the relative increase of the global particle confinement time τ_p^B/τ_p^{OH} can be estimated from the relation

$$\frac{\tau_p^B}{\tau_p^{OH}} \geq \frac{n^B}{n^{OH}} \frac{I_{H\alpha}^{OH}}{I_{H\alpha}^{B}}$$

The relative increase of τ_p by $\sim 50\%$ is evident from the bottom panel.

When the biasing pulse terminates, the plasma density starts to decay exponentially to the original level as $n \sim e^{-t/\tau_N}$. The characteristic time $\tau_N \approx 1.4\ ms$ is a reliable estimate of the particle confinement time without biasing τ_p^{OH}.

These observations clearly indicate the formation of a transport barrier during the biasing period when the electrode is slightly outside the VSL.

It should be noted that even stronger improvement of τ_p is observed, if the electrode is deeper immersed into the plasma, i.e. into the confinement region [18]. Moreover, in this case the *H_α-line radiation* intensity[3] drops with biasing by $\sim$ 50 %. In contradiction with phenomena observed on the ISTTOK tokamak at limiter biasing experiments, the negative

[3] measured along one chord ($\Rightarrow$ not averaged over the whole poloidal plane) $\Rightarrow$ makes only a rough estimate of the recycling level, and therefore τ_p

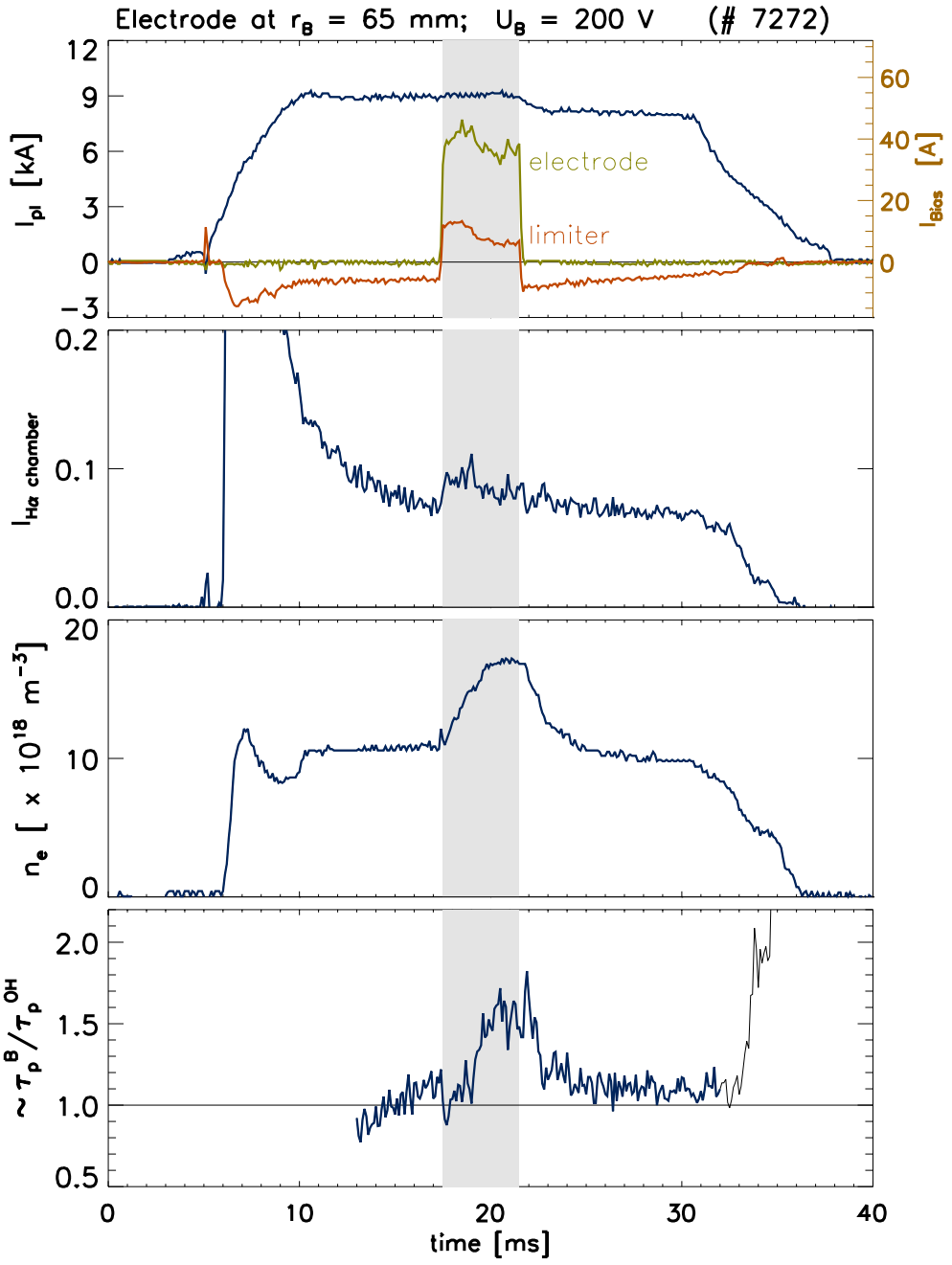

Fig. 8.3: Time evolution of some basic plasma parameters: **a)** plasma current (upper line, left y-axis), electrode current, and return current to the limiter (both right y-axis) **b)** Intensity of the H_α spectral line **c)** line average density $\bar{n}_e$ **d)** lower estimate of the relative increase of the particle confinement time. When the electrode is located more inside into the plasma, the parameters do not change much except of the H_α-signal which drops during the biasing.

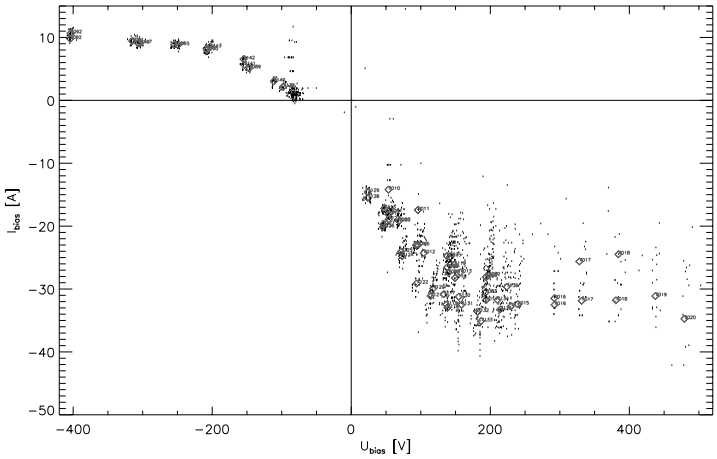

Fig. 8.4: VI-characteristics of the biasing electrode

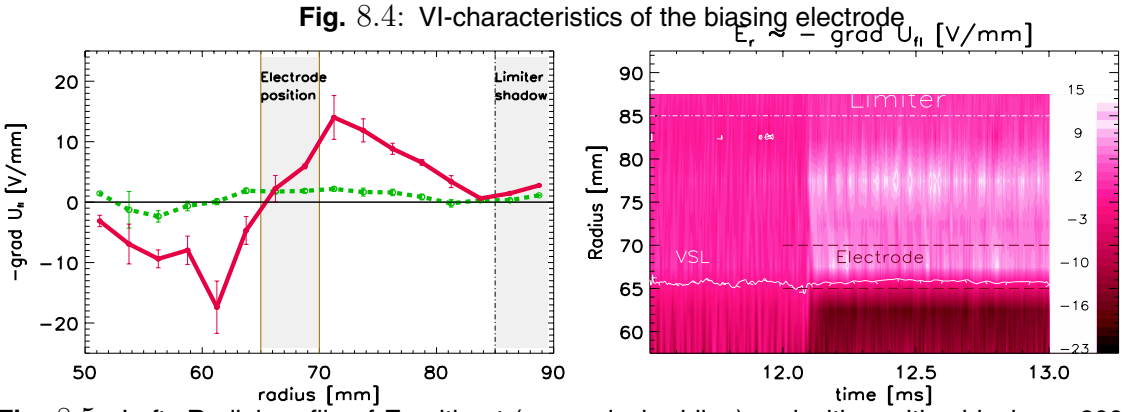

Fig. 8.5: Left: Radial profile of E_r without (green dashed line) and with positive biasing + 200 V (red solid line). Right: Gray scale plot of the spatial-temporal evolution of E_r; the scale (in V/mm) is indicated at the right hand side.

biasing on CASTOR shows only slight effect on the plasma confinement. Also in TEXTOR the *negative* bias did make change of potential profile [16], however, the positive bias really *is* more effective[4].

8.3.2 Radial profiles at the plasma edge

The response of the edge plasma to positive biasing is measured by the radial probe array. An example of the radial electric field measurements is shown in Fig.8.5.

The left panel compares the time averaged profiles of the radial electric field without and with biasing. It is well seen that the electric field increases significantly with biasing at both sides of the VSL, i.e. in the SOL as well as in the edge plasma, reaching there values $\sim \pm 20\ V/mm$. The shear of the radial electric field increases from 0.8 up to 4 V/mm^2 at the separatrix.

The right panel shows an instantaneous radial profile of E_r, recorded in a single shot with the sampling $1\ \mu s$. The bright colours indicate regions with $E_r > +15\ V/mm$, while the dark regions correspond to the negative radial field ($E_r < -15\ V/mm$). The radial position of the

[4] this is because for $U_B < 0$ the electrode current collects less absolute current ($I_{Bias} = I_{sat}$) than for $U_B > 0$ when $|I_{Bias}| < |E_{sat}|$, Fig.8.4

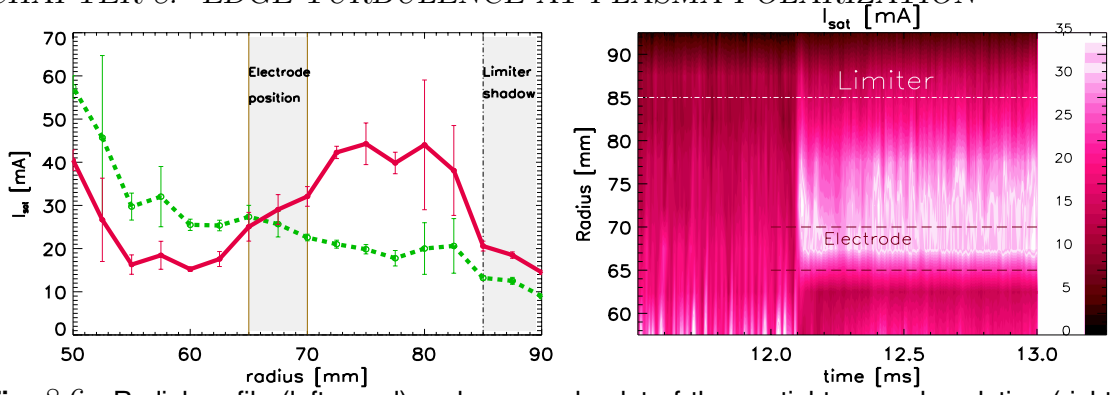

Fig. 8.6: Radial profile (left panel) and gray scale plot of the spatial-temporal evolution (right panel, #7355) of the ion saturation current.

VSL (marked by the white line) remains unchanged at biasing.

The increase of the E_r – shear strongly impacts the edge plasma density as demonstrated in Fig.8.6.

These plots are arranged in a similar way as the previous ones. The probe tips are operating in the ion saturation current mode. It is evident that the increase of the dE_r/dr is followed by a reduction of the edge density by a factor ~ 2 at $r < 65\ mm$, i.e. inside the VSL. This, together with the increase of the line average density, indicates the formation of a steep density gradient somewhere deeper in the plasma column. Note also the reduction of density fluctuations in this region. One of the peculiarities of the biasing experiment is the increase of I_{sat} in the scrape-off layer.

The quasiperiodical structures ($f \sim 10\ kHz$) in E_r and I_{sat} are formed in SOL during biasing as seen in Figs 5 and 6. They appear, when the biasing voltage exceeds $\sim +100\ V$. Similar "coherent" structures have been observed also on TEXTOR-94 [11], however, at higher frequencies.

8.3.3 The Correlation analysis of fluctuations

The correlation analysis is used to deduce the characteristic dimensions/lifetimes of the turbulent structures and their propagation velocities [26].

The correlation length and phase velocity in the poloidal direction are deduced from correlation analysis of data from the poloidal probe array. The method and interpretation of results are described in [20]. The 2D plots of the spatial temporal correlation functions of the potential fluctuations are shown in Fig.8.7 for nine shots differing in the radial position of the probe array.

The horizontal axis of each panel is the time lag τ_{lag} (in μs), while the vertical axis represents the distance d_p along the probe array (in mm). The bright elliptical patterns correspond to combinations of τ_{lag} and d_p with a high correlation ($> 50\%$). The poloidal correlation length of turbulent structures is deduced here as the FWHM (Full Width at Half Maximum) of the correlation function at $\tau_{lag} = 0$. The sense and absolute value of the poloidal velocity can be deduced from the slope of the correlation patterns by such method:

Find a slope of symmetry[5] of a given graph from the Fig.8.7. This slope defines ratio of poloidal distance : time lag which is just equal to the *phase poloidal velocity* v_{pol}^{phase}.

[5] It is not just a slope of symmetry but a close direction, properly described in [19].

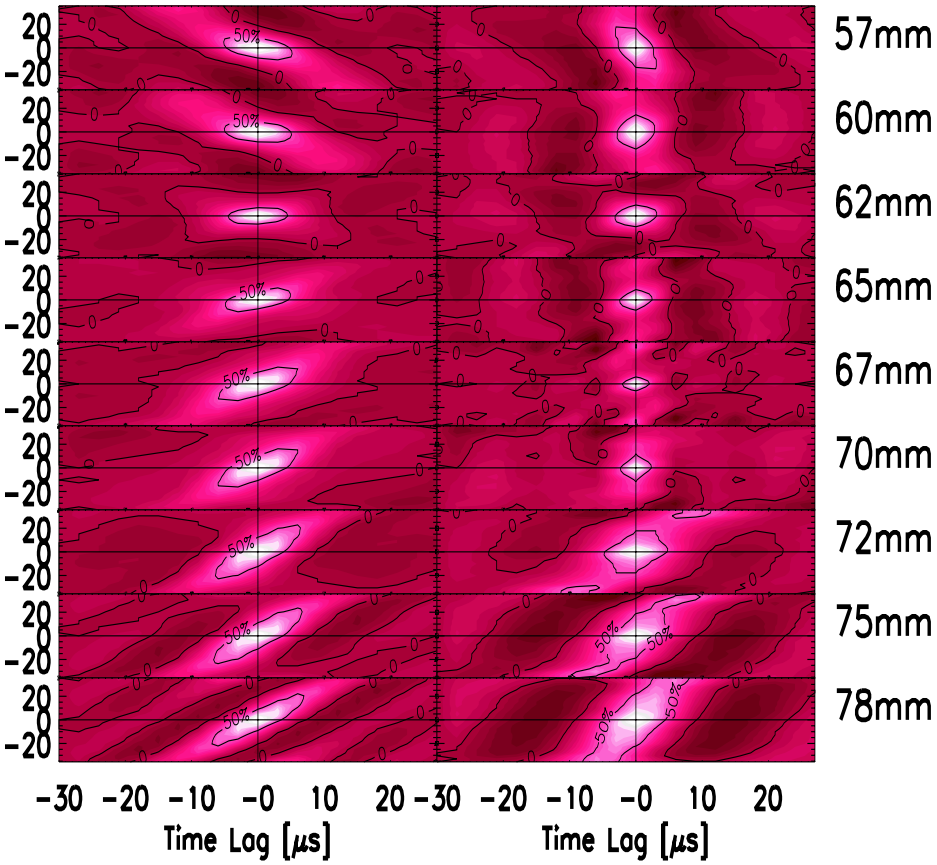

Fig. 8.7: Spatial-temporal correlation functions of the potential fluctuations for nine shots differing in the position of the poloidal probe array. The left (right) column corresponds to the situation without (with) biasing.

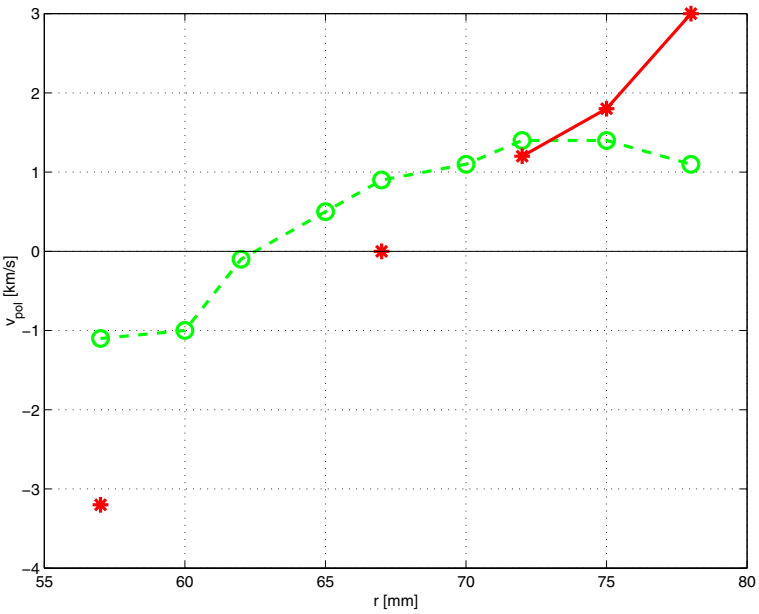

Fig. 8.8: Phase Poloidal Velocities of the potential fluctuations estimated from measurements of type of the Fig.8.7 for several shots differing in the position of the poloidal probe array. The blue empty (red full) circles corresponds to the situation without (with) biasing.

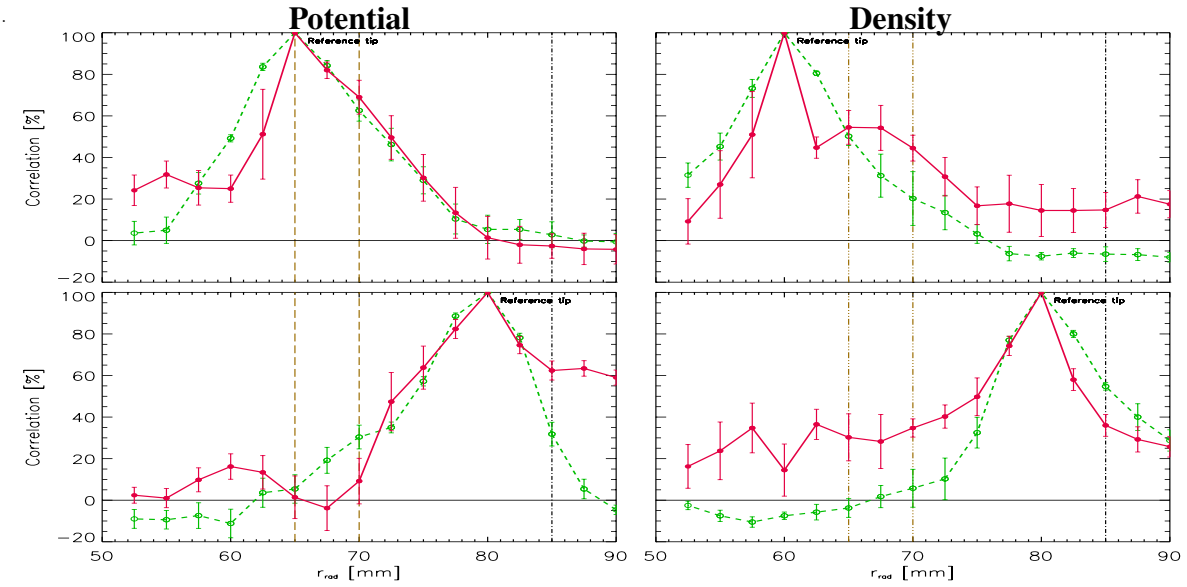

Fig. 8.9: Spatial correlation of the potential (left column) and density (right column) fluctuations in the radial direction. Correlations without (green dashed line) and with (red solid line) biasing are compared. First row: the reference tip is in the proximity of the VSL; Second row: the reference tip is in the SOL.

Its connection to the *flux poloidal velocity*, v_{pol}^{flux} has been measured at CASTOR by the *Mach probe* which preliminary *confirms that the flux and phase poloidal velocities are equal.*

Further, we compare here again the correlation patterns without (left column) and with (right column) biasing. It is well seen that, in the unpolarized plasma, the poloidal propagation reverses at the VSL, which is located at $r \sim 62\ mm$ in this shot series. During the polarized phase of the discharge, an increase of the propagation velocity is apparent outside as well as inside the VSL (compare the slopes of the correlation patterns with and without biasing at $r = 57\ mm$ and $r = 75\ mm$). However, the form of correlation patterns in the region of the highest shear does not allow to determine neither the sense of propagation nor the module of poloidal velocity.

In the radial direction, the turbulent structures are characterized by computing the correlation coefficient $C_{i,j}$ $(i, j = 1 \div 16)$ between the signals of the tips of the radial probe array. The time lag was taken as zero. Examples of the resulting radial profiles of $C_{i,j}$ are shown in Fig.8.9.

We see that the spatial cross-correlation functions without biasing (green dashed lines) appear to be symmetric around the position of the reference tip independently, whether the tip is in the proximity of the VSL or elsewhere. The radial correlation length, deduced here as the half width of the cross-correlation function is of about 10 mm. On the other hand, with biasing, the spatial correlation function is strongly asymmetric, namely if the reference tip is in proximity of the VSL (see the first row in Fig.8.9). This is because the radial correlation length is already comparable or even shorter than the distance between the tips. To overcome this problem, the correlation coefficients $C_{i,i+1}$ of signals of the adjacent tips are taken as a measure of the radial correlation length in polarized discharges.

The resulting radial profiles of the quantities which characterize the turbulent structures in the radial and poloidal directions are plotted in Fig.8.10.

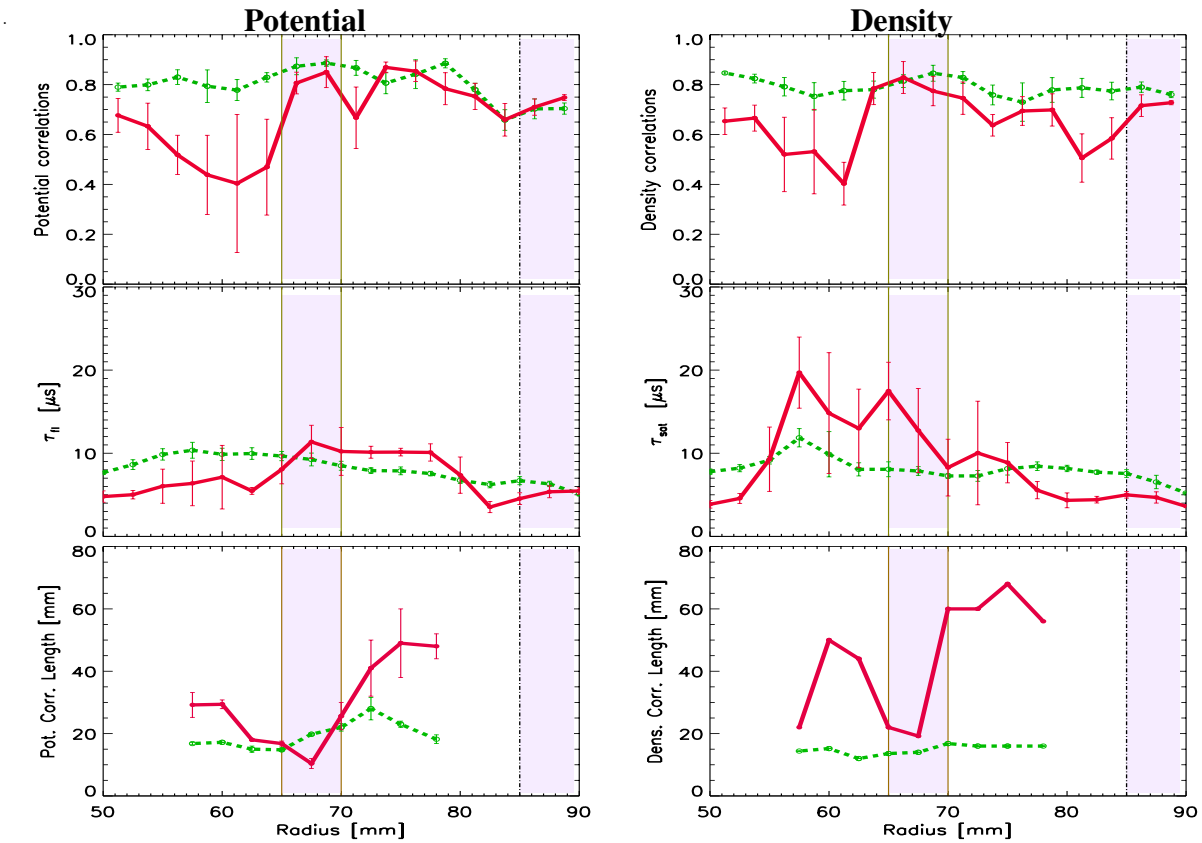

Fig. 8.10: Radial profiles of the parameters, characterizing the potential (left column) and density (right column) fluctuations without (green dashed lines) and with (red solid lines) positive biasing. The positions of the electrode and of the poloidal limiter are marked by shadowing. The profiles shown in the first two rows are derived using the radial probe array, while the last row corresponds to data from the poloidal probe array measured on the shot-to-shot basis. Individual rows (from top to bottom): Correlation coefficient $C_{i,i+1}$ of signals of adjacent tips (proportional to the radial correlation length), the autocorrelation time (determined as the FWHM of the autocorrelation function) and the poloidal correlation length.

As it is evident from this figure, the enhancement of the E_r - shear by a factor of ~ 5 at biasing is followed by a complex response of the edge turbulence. A dramatic drop of the potential as well as of the density correlation coefficients $C_{i,i+1}$ are observed in the region, where E_r appears to be more negative, i.e. in the confinement region. On the other hand, fluctuations seem to be radially "untouched" within the scrape-off layer ($E_r > 0$). One should note that the drop of $C_{i,i+1}$ below 0.5 implies a reduction of the radial correlation length below 2.5 mm.

The reduction of the autocorrelation time, observed at $E_r < 0$ for potential fluctuation and at $E_r > 0$ for the density fluctuation can be explained either by a reduction of the life time of the fluctuations or by a Doppler shift, which appears due to an enhanced poloidal rotation. On the other hand, an increase of τ_A (observed in SOL for the potential fluctuations and in the edge plasma for the density fluctuations) can be attributed only to an increase of average lifetime of turbulent structures.

The poloidal correlation length is reduced or remains unchanged only at radii corresponding to the radial position of the biasing electrode. However, it increases significantly with biasing at both sides of the electrode.

8.3.4 Fluctuation-induced flux in polarized plasmas

The fluctuation-induced flux Γ, which is generally believed to be responsible for particle losses from tokamak plasmas [21], is determined by the cross-correlation of the density $\tilde{n}$ and poloidal electric field fluctuations $\tilde{E}_p$ as

$$\Gamma =< \tilde{n}\tilde{E}_p > /B_T \tag{8.1}$$

Alternatively, Γ can be expressed as a product of density ($\tilde{n} = \sqrt{< \tilde{n}^2 >}$) and the poloidal electric field ($\tilde{E}_p = \sqrt{< \tilde{E}_p^2 >}$) fluctuations

$$\Gamma = (\tilde{n}\tilde{E}_p C(n, E_p))/B_T \quad , \tag{8.2}$$

where $C(n, E_p)$ is correlation between the density and E_p fluctuations [11].

The flux Γ can be easily experimentally deduced using the poloidal probe array operating with odd tips in the floating mode and even tips in the ion saturation current mode [20]. The radial profiles of Γ without (green dashed line) and with (red solid line) biasing are compared in Fig.8.11. As seen, the fluctuation-induced flux is practically suppressed outside the VSL. At the same time, the levels of n and E_p fluctuations are only slightly reduced. Therefore, the suppression of Γ is mainly due to the decorrelation between the density and poloidal field fluctuations. Similar observation was reported in [11].

8.4 Conclusions

Experiments on the CASTOR tokamak demonstrate the possibility to form a transport barrier in the edge plasma using a massive graphite electrode, positioned in the scrape of layer and biased at $+200\ V$. The radial electric field is affected not only between the electrode and the vacuum vessel as expected but also by the formation of a negative field of the same order of magnitude within the last closed flux surface. The global particle confinement improves by $\sim 50\%$.

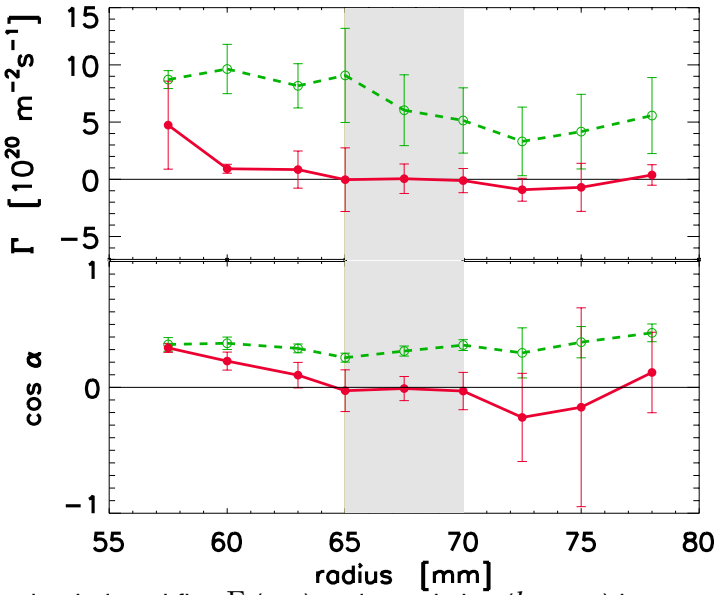

Fig. 8.11: Fluctuation-induced flux Γ (*top*) and correlation (*bottom*) between the density and poloidal electric field fluctuations, $C(n, E_p) =< \tilde{n}\tilde{E}_p > / \sqrt{< \tilde{n}^2 >< \tilde{E}_p^2 >}$.

The resulting shear of the radial electric field in the separatrix region is as high as $4\ V/mm^2$ which reveals the $E \times B$ decorrelation rate $\omega_{E\times B} \sim 4 \times 10^6 s^{-1}$. This value is substantially higher than the expected growth rate of the edge electrostatic fluctuations $\gamma \sim 10^5 \div 10^6 s^{-1}$.

The enhanced shear of the radial electric field in the separatrix region in polarized discharges impacts dramatically on the edge electrostatic fluctuations as shown by the spatial-temporal resolved probe measurements. Some observed features, such as the radial decorrelation in the proximity of VSL, can be expected. However, the observed increase of the poloidal correlation and lifetime of fluctuations is not understood up to now. The last effect could be related to a quasiperiodic low frequency component ($f \leq 10\ kHz$) of the plasma fluctuations, which appears when dE_r/dr prevails a critical value. Such modulation is even more apparent, if the electrode is deeper immersed in the edge plasma and biased to more than $+150V$.

In conclusion, we show in this contribution that the polarization of the edge plasma, if it is accompanied by the spatially resolved measurement of the plasma fluctuations, represents a useful experimental tool to control the ExB decorrelation of the turbulent structures in the edge plasma of tokamaks. It is evident, however, that the correct interpretation of the complex behaviour of the edge turbulence shown here requires additional experiments.

Part III

Work at TCV (divertor physics)

At CRPP (TCV tokamak) I worked for three months (August-November 1999) in collaboration with

- Dr. R.A. Pitts (my supervisor), CRPP-EPFL, Lausanne, Switzerland,

  e-mail: richard.pitts@epfl.ch, Web: crppwww.epfl.ch/∼pitts
- Prof. P.C. Stangeby (discussion by e-mail), Institute for Aerospace Studies, University of Toronto, Canada, e-mail: stangeby@apollo.gat.com

Since TCV was under maintenance during this period, I could not attend the experimental programme and thus my work comprised these two separate themes:

- Code a *computer programme* for processing data from Langmuir probes embedded in the TCV divertor target. I incorporated number of (mostly) existing routines into a Graphical User Interface using the Matlab 5.3 high level language, employing the new technique of object oriented programming.

  Supervisor: Dr. R.A. Pitts, time of duration: two months.

- Using this programme to try to answer the following important question:

  Why do divertor Langmuir probes measure too high electron temperature in TCV high recycling regimes ?

  We focused on three different "explanations" and the last one, described in chapter 12, seems to be really credible.

  In collaboration with Dr. R.A. Pitts and prof. P.C. Stangeby with time of duration of three weeks:

  - *decision* between two different methods ("T_e - min", "up to U_{fl}") of VI-characteristics processing, chapter 10
  - *comparison* between artificial and measured VI-char. An artificial characteristics were generated to investigate the *effect of noise* on the data. This was performed by introducing noise on I_{sat}, V_{fl}, T_e of varying degree of (de)correlation and amplitude, chapter 11.

After returning to Prague I continued in collaboration with R.A. Pitts and A. Loarte (EFDA-CSU, Garching, loartea@ipp.mpg.de) in modelling (concerning the above question), but this time concentrating on the effect of SOL collisionality, chapter 12.

Basic literature of divertor physics: start with [1, chap. 9.10], much more detailed in [30].

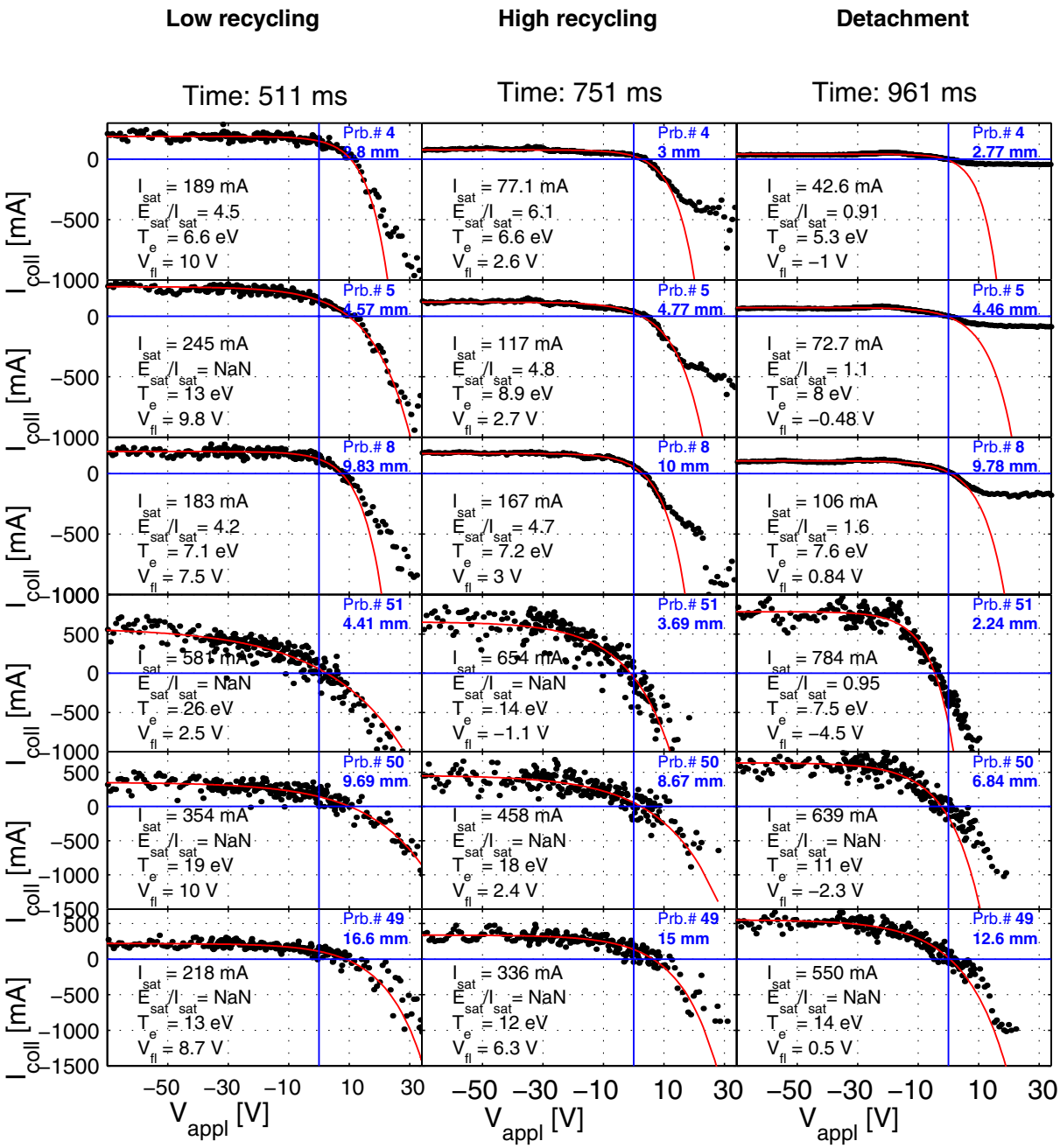

Fig. 8.12: Gallery of VI-char.. Are these fits wrong? No, but still one knows T_e can not be so high in high recycling or even detachment. The ratio E_{sat}/I_{sat} is also funny if compared with Eq.(C.2). Probes 4,5,8 are on the floor, 49,50,51 on the central column; their distances from the midplane separatrix are written - these probes are geometrically the closest ones to mag. surfaces (1.8, 4.7, 9.6 mm) computed by the B2-Eirene, used in Chap.12.

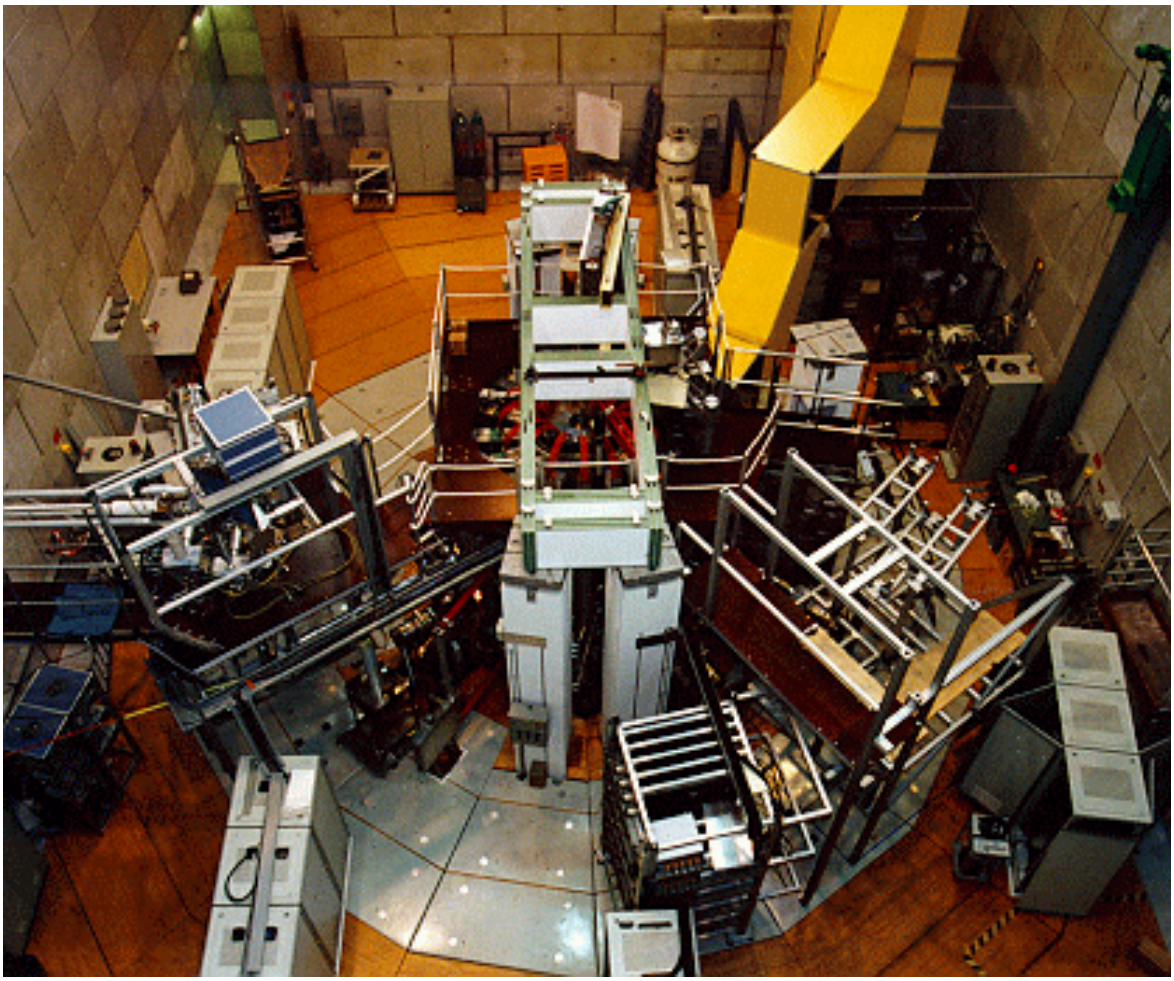

Fig. 8.13: TCV top view

Chapter 9

Hardware

9.1 Tokamak TCV

TCV tokamak (in operation from 1992) is located at the Centre de Recherche en Plasma Physique (CRPP), the university École Polytechnique Fédérale de Lausanne (EPFL), Switzerland. Visit its web-page: http://crppwww.epfl.ch.

The distinguishing feature for the TCV (**T**okamak à **C**onfiguration **V**ariable), compared to other world tokamaks, is *variability of plasma shape and position,* as is shown in Fig.9.2.

9.2 Divertor geometry and Langmuir probes

The TCV *divertor*[1] is

- *very open*: the divertor plates are just parts of the inner wall.
- it is *very variable* (see Fig.9.2), also both *single null*[2] (SN) or *double null* (DN) magnetic configuration can be created.

There are two rows of probes embedded in protection tiles on the vacuum vessel floor and the central column, as depicted in Fig.9.3 and Fig.9.1. They are domed, single Langmuir probes with diameter of 4.0 mm and max. height above the surface of 1.0 mm. They are manufactured in graphite and have a complex spring system retaining them in the tile. There is a gap of 0.5 mm between each probe and the tile.

[1] Explanation of this concept is in section C.2.2.

[2] Null means place with zero B_θ, i.e. the X-point $\Rightarrow$ single (double) null means such a B-field configuration with one (two) X-points, respectively.

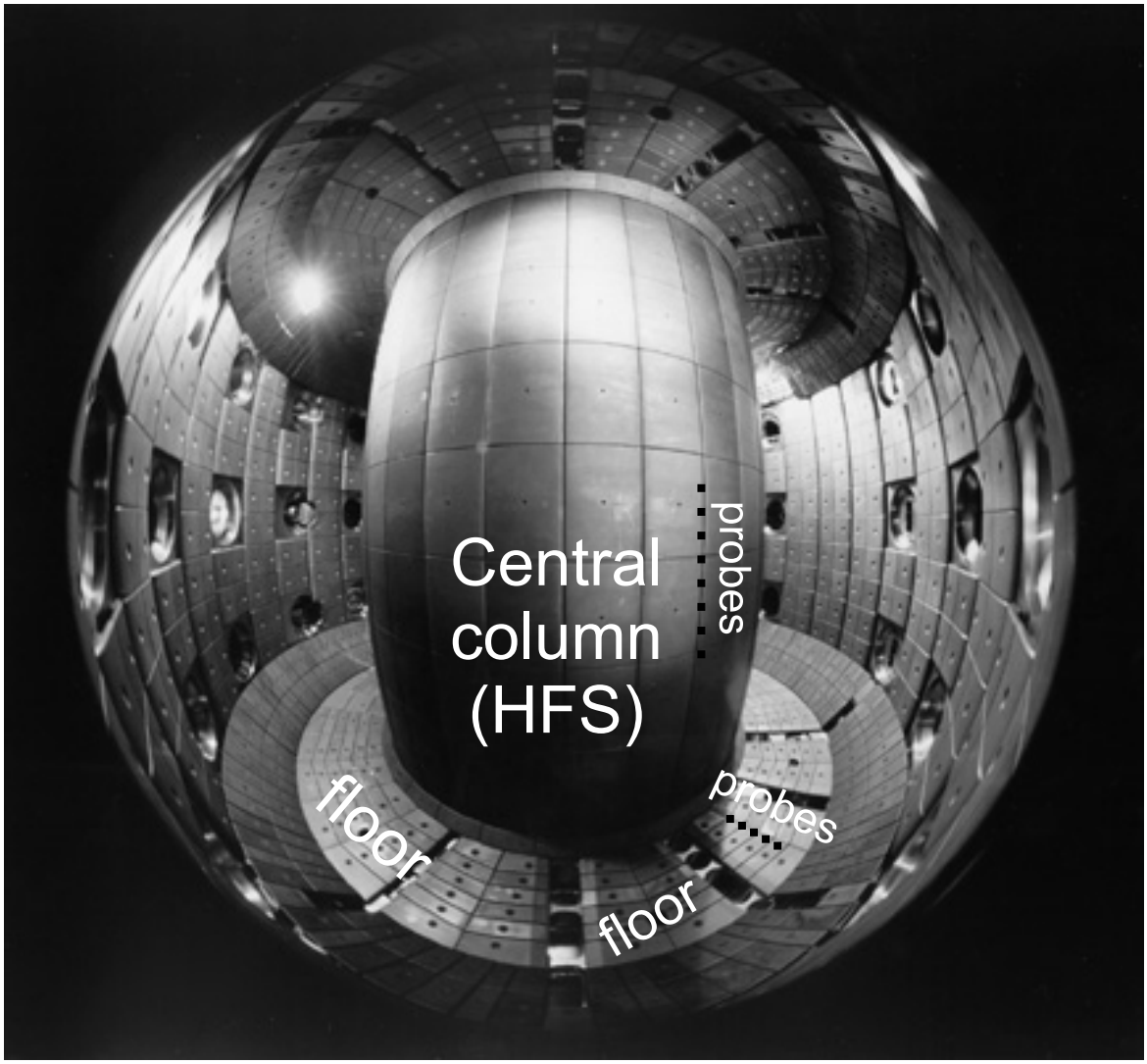

Fig. 9.1: An angle-spread view of the TCV inside. The two rows (on the floor, 26 probes & central column,) of Langmuir probes are schematically shown.

Plasma height	max. 1.44m
Plasma width max.	0.48m
Plasma major radius	0.875m
Plasma current	1.2MA
Plasma elongation κ	max. 3
Aspect ratio	3.6
Toroidal magnetic field on the magnetic axis	max.1.43T
Additional heating (ECRH)	max.4.5MW
Transformer flux	3.4Vsec
Loop voltage	max.10V
Plasma duration	max. 2 sec
Vessel width	0.56m
Vessel height	1.54m
Vessel ohmic resistance	55mW
Wall heating temperature	max.350°C

Table 9.1: Tokamak TCV parameters

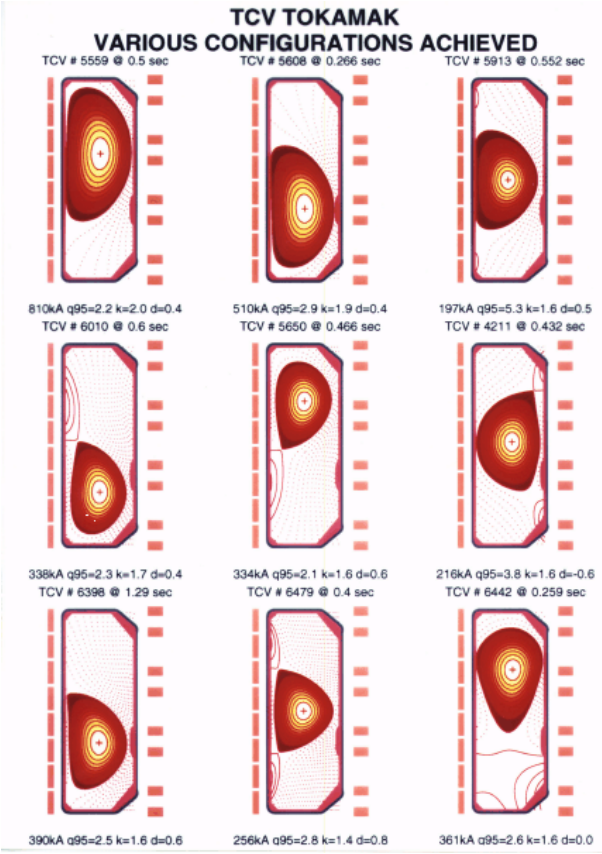

Fig. 9.2: Examples of various plasma shapes in TCV (poloidal cross-section)

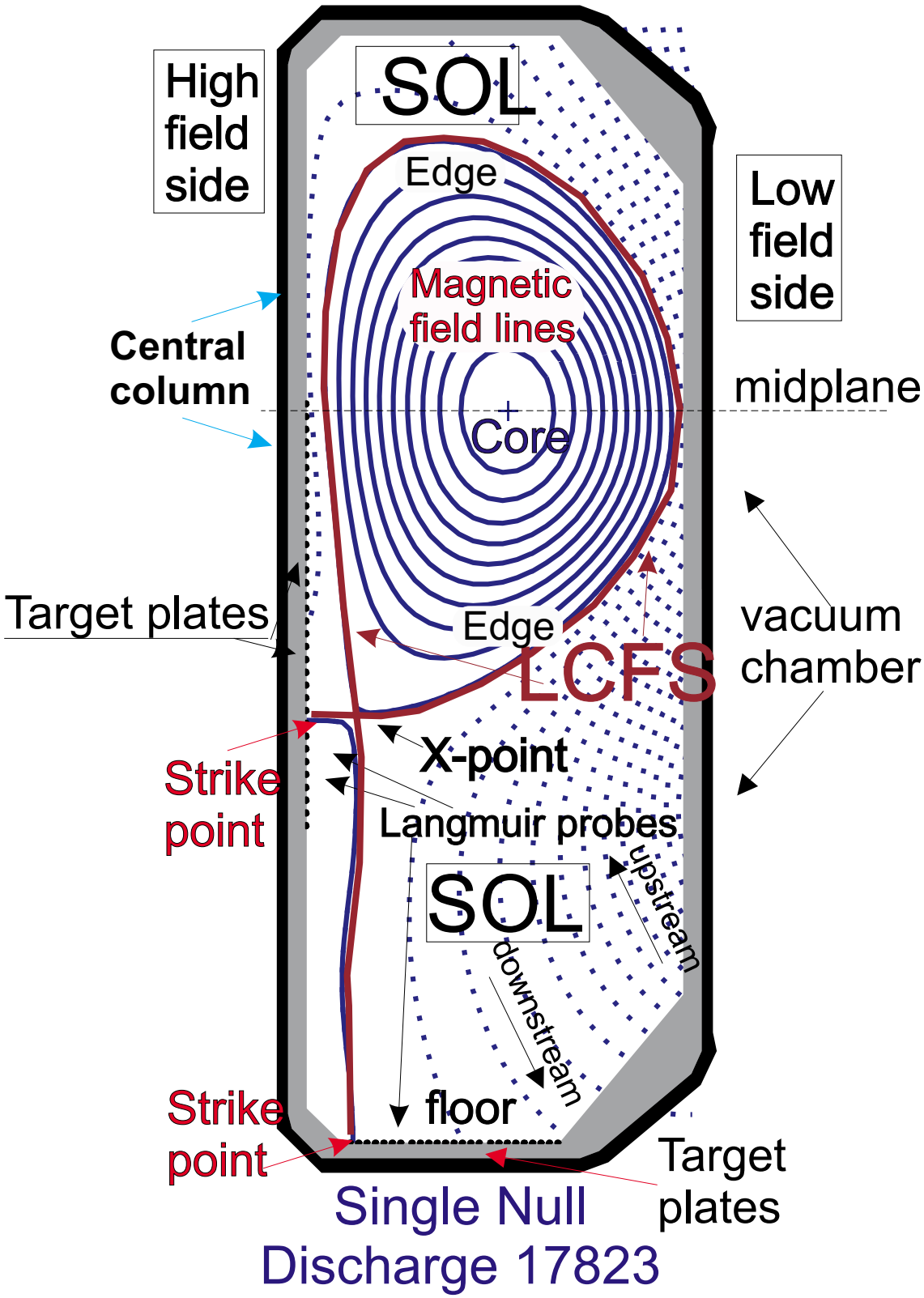

Fig. 9.3: Poloidal cross-section of the TCV chamber; visualization of divertor function & two rows of Langmuir probes, emphasized in the bottom figures (floor & central column probes).

Chapter 10

Two methods of Langmuir probe characteristics processing

10.1 Langmuir probe in strong magnetic field and at low T_e

The standard theory of VI-characteristic of LP has been proposed by Langmuir, assuming non-magnetized plasma with Maxwellized electron velocity distribution. This is in detail described in chapter C.1. In this case the collected current (I_{coll}) as a function of applied voltage (V_{appl}) is:

$$I_{coll} = I_{sat}(1 - exp(\frac{V_{appl} - V_{fl}}{k_B T_e})),$$

Some physicists [31] *doubt* that in magnetized plasmas the points [V_{appl},I_{coll}] have this "exponential behavior" outside this region:

$$V_{appl} < V_{fl} \ <=> \ I_{coll} > 0; \quad definition\ of\ "up\ to\ U_{fl}"\ -\ region \tag{10.1}$$

The standard ("up to U_{fl}") - method of processing VI-chars. takes into account only points in the "up to U_{fl}"- region.

In the following chapter we just focus on some more robust method.

10.2 "T_e - min" - method

There has been proposed following recipe to process VI-char.:

- From the VI-char. take into account only these points [V_{appl},I_{coll}] belonging to these sets

  $$M_i : V_{appl} < V_i,\ V_i \in (V_{fl}, V_{E_{sat}}),\ V_i < V_{i+1},\ \ definition\ of\ M_i \tag{10.2}$$

  where $V_{E_{sat}}$ is a potential, where the VI-char. *turns* from "exponential" to "saturated", E_{sat}, i.e.

  $$I_{coll}(V_{appl} > V_{E_{sat}}) \simeq E_{sat} \quad .... \ definition\ of\ V_{E_{sat}} \tag{10.3}$$

  i is now *a new (discrete) degree of freedom*, $i \in (1, n)$, where n equals (due to Eq.(10.2)) the number of points measured in the region of $V_{fl} < V_{appl} < V_{E_{sat}}$

- Fit these VI-chars. for all sets M_i to evaluate four sets of values of $I^i_{sat}, E^i_{sat}, T^i_e, V^i_{fl}$.
- Find the *minimal* value of T^i_e, i.e. find index i_{min} which fulfils[1]:

$$T_e^{i_{min}} = min(T_e^i)$$

Then the corresponding value of $I^{i_{min}}_{sat}, E^{i_{min}}_{sat}, T^{i_{min}}_e, V^{i_{min}}_{fl}$ call as "real".

From description of the "T_e - min" - method one can see **the "up to U_{fl}" - method is equal to the "T_e - min" - method with constant $i = 1$.**

The "T_e - min" curve can be drawn as a function of $V_i - V_{fl}$, see Fig.10.1. In the graph of T_e - *min* one can see strong *correlation* between T_e and I_{sat}.

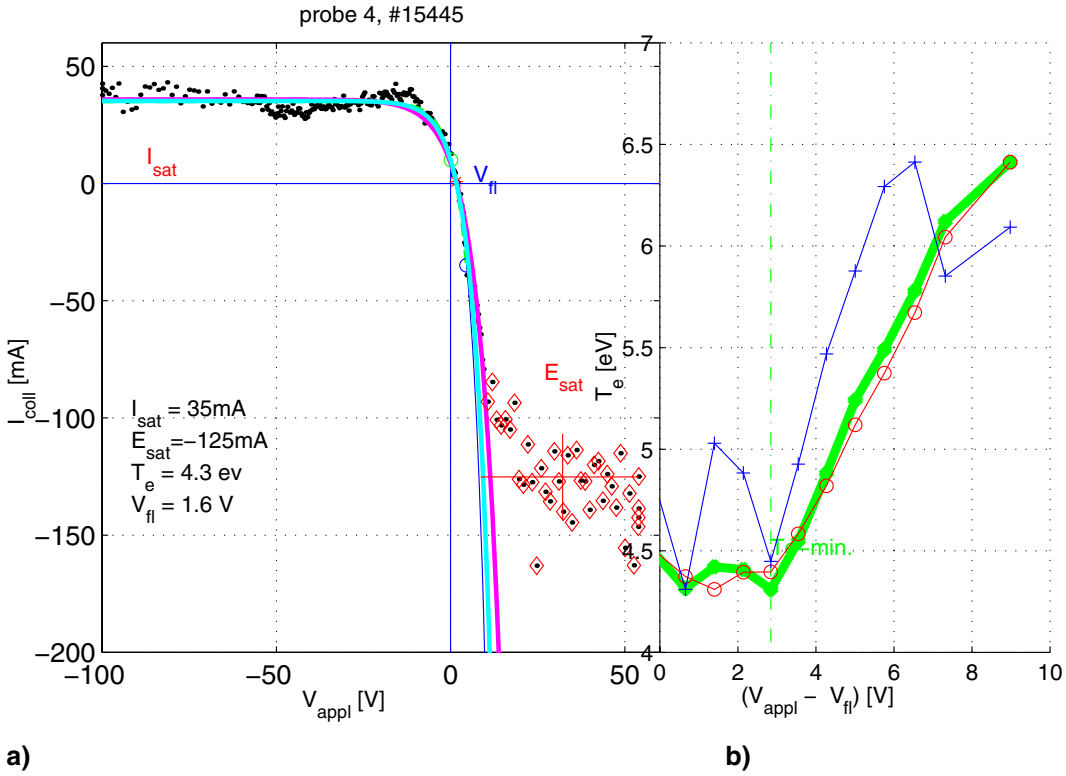

Fig. 10.1: **a)** Typical Langmuir probe VI-char. measured by a TCV divertor probe. The red diamonds are associated to E_{sat}. **b)** The "T_e - min"-figure; minimum of the T_e - curve (green) defines T_e associated to the VI-char.There are also V_{fl} (blue) and I_{sat} (red) curves. The Y-scale is associated only with the T_e - curve, the curves of I_{sat}, V_{fl} are *rescaled* to *fit* the figure.

10.2.1 Is "T_e - min" better than "up to U_{fl}" -method?

- In high recycling and detached regimes the divertor T_e measured by *spectroscopy* is usually *many times lower*[2] than that measured by Langmuir probes[3]. Some authors

[1] Therefore this method is called T_e - minimization

[2] This low temperature (c. $1eV$) must exist to explain the drop in ion flux to the divertor targets during detachment.

[3] let us assign it further as T^{LP}_e

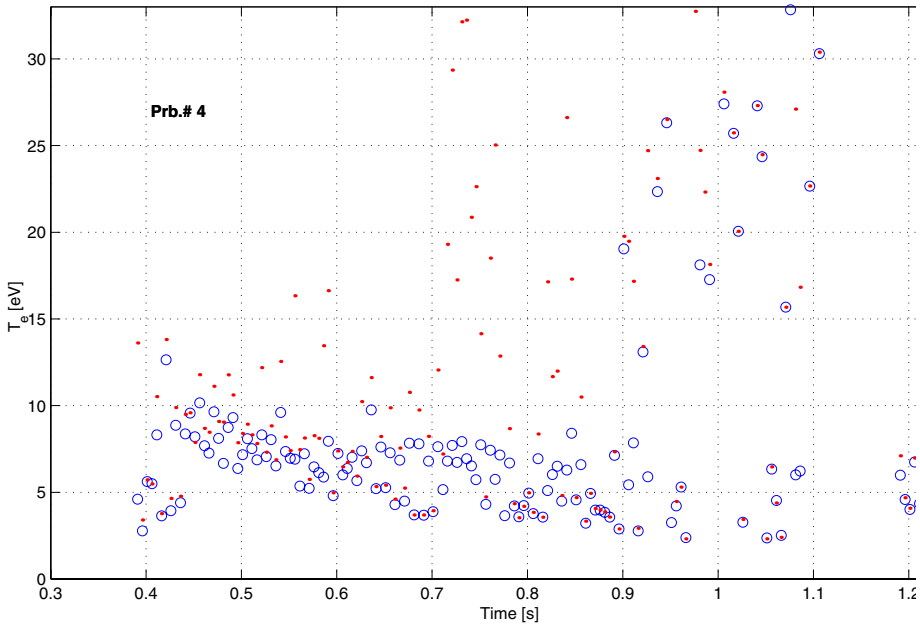

Fig. 10.2: T_e estimated by the "T_e - min"(blue circles) and "up to U_{fl}"(red dots) method.

therefore employ the "T_e - min"method to ensure that at least the "lowest" value of T_e is found. The method is "ad hoc" - *there is no physics justification* whatsoever. The reasoning is simply that progressively adding some points above V_{fl} can help to guide the fit to lower T_e's, even though the characteristics is very often not exponential there.

- One more degree of freedom (index i) allows to fit more VI-chars. Indeed, there is *higher chance to get at least any value* of $[I_{sat}, T_e, V_{fl}]$ from a given VI-char. $\Leftarrow$ *not for all the indices* i (and so for $i = 1$ corresponding to the "up to U_{fl}" - method) one *can fit* (i.e. get *any* value); look at the Fig.10.1: the T_e green curve can be discontinuous.

- *Relative values* of T_e fluctuations, $\frac{\tilde{T}_e}{T_e}$, are slightly *lower* for the "T_e - min" -method, see Fig.10.2

Chapter 11

Can fluctuations increase T_e measured by Langmuir probe ?

In this chapter we focus on trying to explain the too high temperature T_e^{LP}(i.e. measured by a Langmuir probe) by *modelling* the VI-characteristics, assuming it is given by fluctuating I_{sat},E_{sat},V_{fl},T_e quantities.

11.1 Artificial VI-char. creation

1. create a set of "input" *random* values of these quantities[1] $q_i = [I_{sat}^{in}, E_{sat}^{in}, T_e^{in}, V_{fl}^{in}]$ with a definite PDF; we used *normal* distribution characterized by its *mean value* $< q_i >$ and *standard deviation* σ_i, i.e. two parameters for each of the four quantities.

   Further, more complicated sets of *varying fluctuation amplitudes* σ_i or of *non-zero correlation* C_{ij} between some of these four quantities can be created:

   $$q_i(t) =< q_i > +\sigma_i R_i(t), \;\; t = 250\, pts./char. \tag{11.1}$$

   where R_i is the random quantity of *normal distribution* (i.e. $< R_i >= 0, \; \sqrt{R_i^2} = 1$) of zero mutual and auto- correlation[2] $C(q_i(t), q_j(t')) = \delta_{ij}\delta_{tt'}$. If non-zero correlation between e.g. I_{sat}^{in} and V_{fl}^{in} is desired, $C_{I_{sat},V_{fl}} \neq 0$, then just recompute $R_{I_{sat}}$

   $$a \stackrel{\text{def}}{=} 1 - |c|, \quad \frac{a \cdot R_{I_{sat}} + c \cdot R_{V_{fl}}}{\sqrt{a^2 + c^2}} \rightarrow R_{I_{sat}}. \tag{11.2}$$

   where $c = c(C_{I_{sat},V_{fl}})$ is a parameter of a suitable value[3]. Now $R_{I_{sat}}$-distribution remains *normal*[4]; the same recomputation could be done, due to its symmetry, for the conjugated $R_{V_{fl}}$.

2. create $I_{coll}(V_{appl})$ using Eq.(C.1):

[1] $i = [1, 2, 3, 4]$, i.e. it just selects quantity.

[2] However, a few autocorrelation was add to make the VI-char.s look more realistic.

[3] It holds at least $c(\pm 1) = \pm 1, c(0) = 0 \; \leftarrow \; C(\frac{a \cdot R_{I_{sat}} + c \cdot R_{V_{fl}}}{\sqrt{a^2+c^2}}, R_{V_{fl}})$

[4] This comes from statistical mathematics

- $I_{coll} = I_{sat}^{in}(1 - exp(\frac{V_{appl} - V_{fl}^{in}}{k_B T_e^{in}}))$
- create E_{sat} - part: if $I_{coll} < E_{sat}^{in}$ set $I_{coll} := E_{sat}^{in}$

i.e. one value of I_{coll} associated to four random values [I_{sat}^{in}, E_{sat}^{in}, T_e^{in}, V_{fl}^{in}]

3. standardly *fit* this VI-char. (composing from these points [V_{appl},I_{coll}]), using the same Eq.(C.1), to get out [I_{sat}^{out}, E_{sat}^{out}, T_e^{out}, V_{fl}^{out}], i.e. four values per one characteristics.

Remark: One "out" value belongs to one VI-char. which contains a lot of "in" points. For example, if one creates, let's say, $n = 10^5$ of [I_{sat}^{in}, E_{sat}^{in}, T_e^{in}, V_{fl}^{in}] and use e.g. $m = 10^3$ points of [V_{appl},I_{coll}] per each characteristic, then one gets out $n/m = 10^2$ of [I_{sat}^{out}, E_{sat}^{out}, T_e^{out}, V_{fl}^{out}].

This set of "output" values is interpreted as an output from a LP measuring plasma which is described by the "input" set of parameters.

The estimated *mean "out" values* will be, of course, equal to the *mean "in" values* if these "in" values do not fluctuate and are not correlated, too[5]. In the next sections we study just the effect of non-zero correlation and of varying amplitudes of fluctuations.

11.2 Varying amplitudes of random V_{fl}^{in}

The example of the artificial "input" data set is shown in Fig.11.1 together with VI-char. created using this input data.

After fitting these characteristics one gets the "output" parameters, shown in the Fig.11.2 as a function of V_{fl}^{in}-SD, from which the effect of varying fluctuations of the V_{fl}^{in} is clear: with **raising V_{fl}^{in}-SD** not only SD of *all "output"* parameters raises (as naturally expected) but also *non-trivially decreases mean value of T_e*.

The explanation of this effect can be done as following: imagine that only V_{fl}^{in} fluctuates. Due to the non-linearity of the VI-char. (Eq.(C.1)) the oscillations of V_{fl}^{in} lead to a *non-symmetrical*[6] oscillations of the I_{coll}. These oscillations favour electron collection and thus pull the fit *down* (i.e. increase its curvature) and hence give a *decreased* value of T_e^{out}. Finally, the result is that T_e **decreases, i.e. changes its mean value in opposite direction than desired** for explanation of the stated question on p. 54.

11.3 Varying correlation of artificial "input" values

We created random "input" values where all [I_{sat}^{in}, E_{sat}^{in}, T_e^{in}, V_{fl}^{in}] were fluctuating, see Fig.11.1, but *only* some of them had *non-zero and varying correlation*.

The "output" values from our fitting routine are shown in the Fig.11.3. The surprising conclusion is that there is *no* dependence of any of these variables on the level of correlation.

[5] in this case the VI-char. is purely exponential, i.e. with no fluctuations

[6] meaning non-symmetrically distributed around a mean value

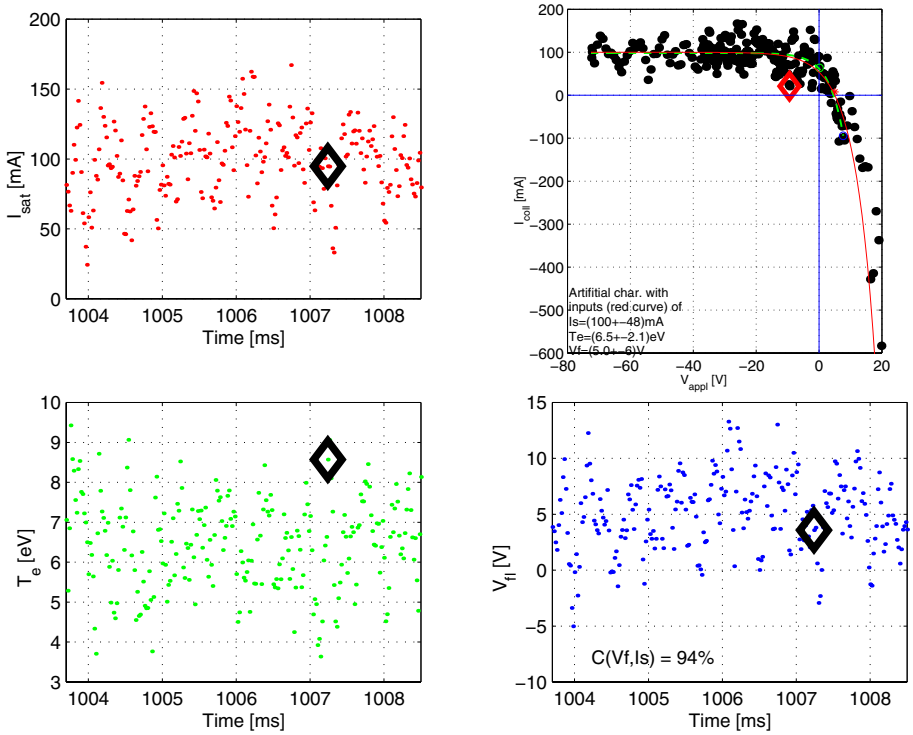

Fig. 11.1: Example of artificial "input" data sets (normal distribution) and an **artificial** VI-chars. created by them: one 3-point (the big ◇) from the three "input" data sets corresponds to one point in the VI-char.. Each of these four quantities is characterized by its mean value and standard deviation as written in the VI-char. fig. An example of non-zero correlation between I_{sat} and V_{fl} is shown.

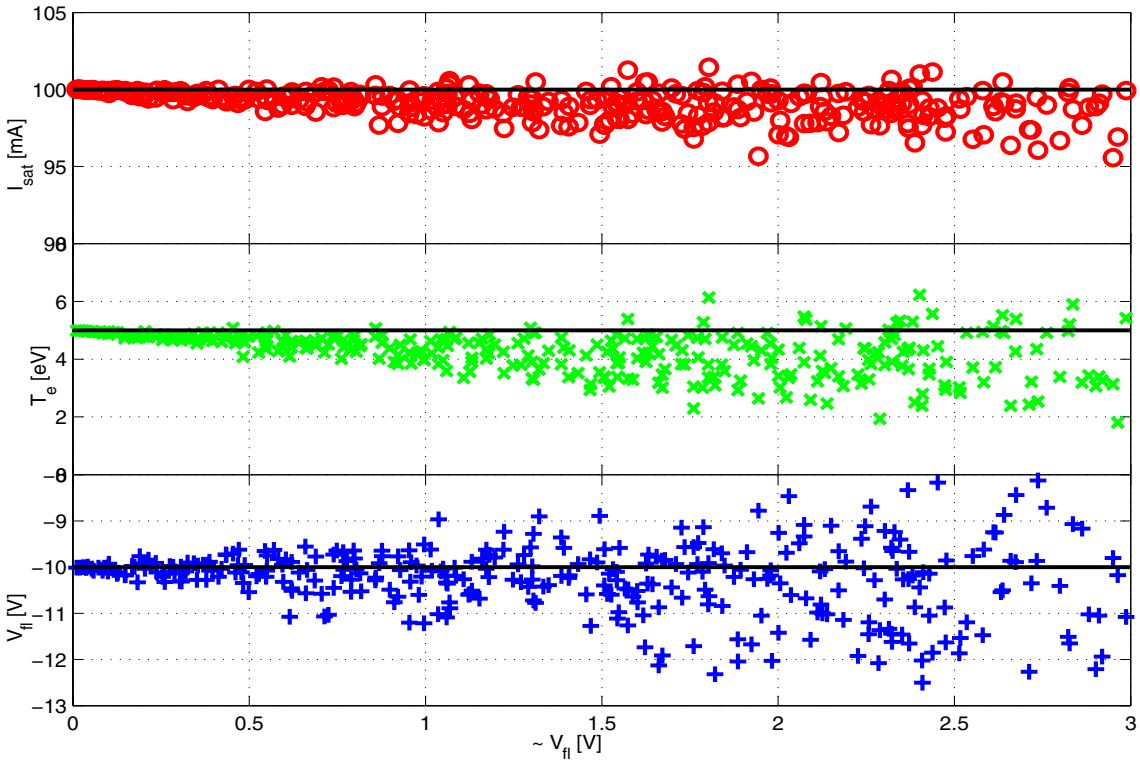

Fig. 11.2: **Varying amplitude**: Dependence of the "**output**" parameters [I_{sat}^{out}, T_e^{out}, V_{fl}^{out}] as a function of V_{fl}^{in} standard deviation. Used "T_e - min" - method, set $I_{sat}^{in} \equiv$ 100mA, $T_e^{in} \equiv$ 5eV, $< V_{fl}^{in} >$=-10V, only V_{fl}^{in} fluctuates.

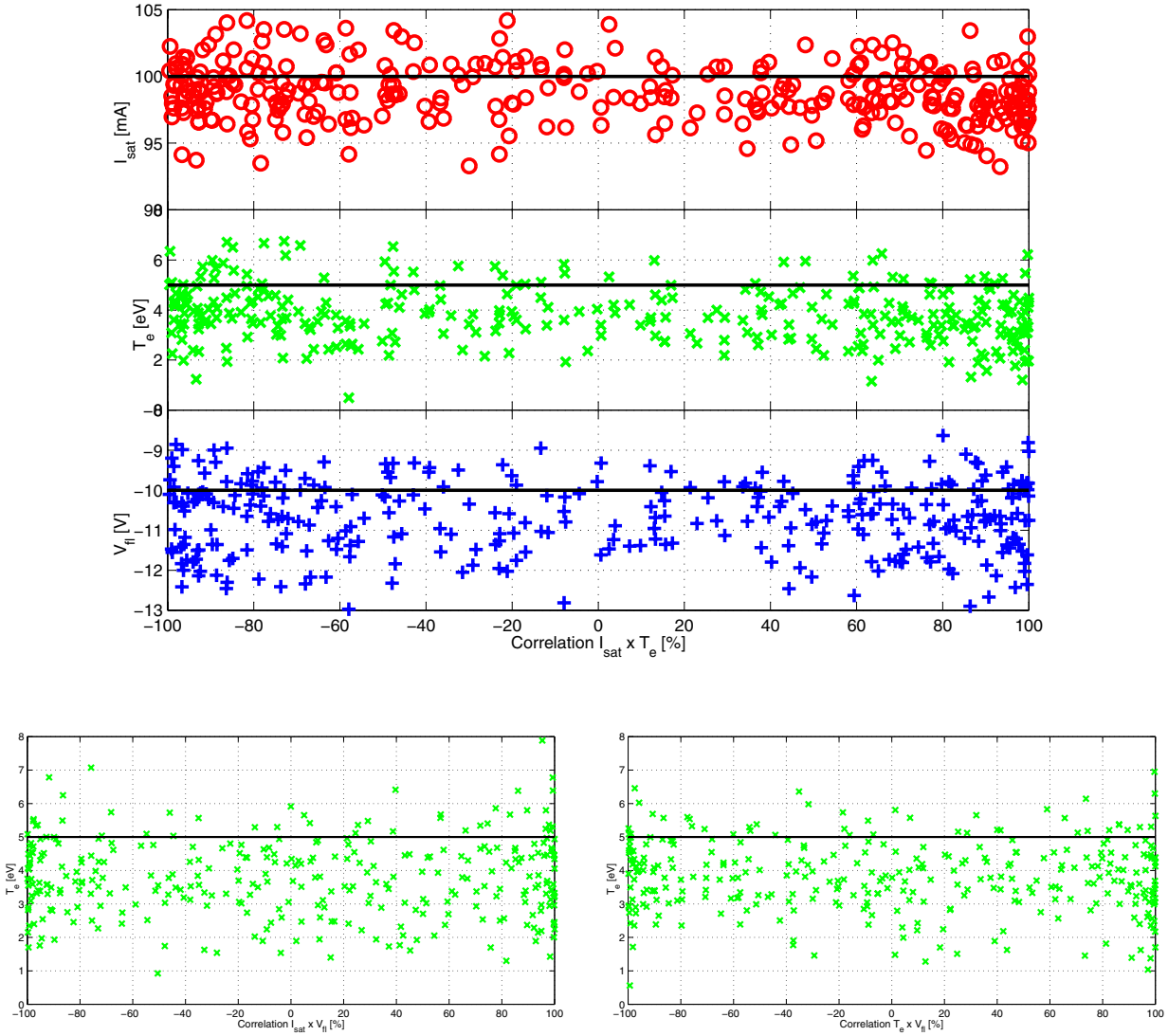

Fig. 11.3: **Varying correlation**: Dependence of the **"output"** parameters [I_{sat}^{out}, T_e^{out}, V_{fl}^{out}] as a function of **correlation.** Used "T_e - min" - method, set I_{sat}^{in}=(100± 20) mA, T_e^{in}=(5± 1) eV, V_{fl}^{in}=(-10± 4) V.

11.4 Conclusions

The effect of the level of V_{fl}^{in} fluctuations on the extracted T_e^{out} has been found, but in opposite direction than desired for explanation of the too high T_e^{LP}(i.e. measured by a LP. In addition, surprisingly, no effect of correlation has been found.

Chapter 12

Effect of parallel temperature gradient on effective divertor target temperature measured by Langmuir probe

In this chapter we are again focused on the same question as in both previous chapters:
"Why does divertor Langmuir probe measure T_e so high in high recycling regime ?"
but now trying to find the answer using an 1 D idea of effect of parallel temperature and density gradient[1] $\nabla_{\parallel} T_e$, $n(x)$ on plasma sheath in the divertor region. This idea is based originally on [37, p. 878], [38], and improved by J.A. Wesson in **[29]**. These T_e, n_e-profiles will be taken[2] from the *2-3 D edge numerical code-package B2-EIRENE [35].*

12.1 Main idea

It is known that any material surface placed in plasma creates a negative sheath in the vicinity of it, which repels electrons. The only electrons collected at the surface are therefore these with energy high enough to overcome the sheath potential barrier; in other words $I_{coll}(V_{appl})$ of a Langmuir probe is determined mostly by the *high-energy tail of the electron PDF* while I_{sat} is assumed to be independent of V_{appl} and hence of the potential sheath drop ϕ_0.

This part of PDF is, however, disturbed by *fast electrons* coming from the *hotter* plasma region more distant from the probe along field lines. If there are regions upstream that are hotter than the local T_e, then the fast (i.e. hot) electrons can reach the probe *collisionlessly* (i.e. without energy losses) and thus contribute to the high-energy tail of the PDF. Therefore the *Langmuir probe does not measure local* $T_0 \equiv T_e(x=0)$ *but "mean"*[3] *temperature across the temperature gradient from the point of a last collision.*

For example, in the theoretical work [32] two temperature (i.e. double-gaussian) PDF is

[1] i.e. gradient of T_e in direction parallel with $\vec{B}$: $\nabla_{\parallel} T_e \equiv \frac{\partial T_e}{\partial x}$, where $x \equiv L_c$ Connection Length, i.e. distance along magnetic field line with respect to the divertor target (where x=0). In following let's assign electron temperature simply as T.

[2] while using input data from TCV-tokamak discharges

[3] At least T_e^{LP} satisfies either $T_\infty \geq T_e^{LP} \geq T_0$ or $T_\infty \leq T_e^{LP} \leq T_0$.

assumed. There is shown that presence of even only *several* per cent of (say $10\times$) hotter electrons is enough to influence the VI-char. of a divertor Langmuir probe to give effectively the *hotter* T_e:

$$n_{hot} \geq 0.01 n_{cold} \ \wedge \ T_{hot} \geq 10 T_{cold} \ \Rightarrow \ T_{eff} \sim T_{hot}, \tag{12.1}$$

while "energetic" mean temperature is naturally

$$T_{Energy} = \frac{n_{hot}T_{hot} + n_{cold}T_{cold}}{n_{hot} + n_{cold}} \approx T_{cold}.$$

$\nabla_\parallel T_e$ is, however, very difficult to measure experimentally in a tokamak since many individual measurements of $T_e$must be made in the SOL across the whole poloidal cross-section. Such measurements are difficult given the lower temperatures and densities in the edge plasma and can often be accomplished only by invasive tehniques such as Langmuir probes. A Thomson scattering diagnostic is being prepared for TCV to at least try and address this problem in the divertor volume of TCV [34].

Therefore we use computed $\nabla_\parallel T_e$ from the *B2-EIRENE code [35],* which is being used to simulate the TCV SOL. This $\nabla_\parallel T_e$ we implement into the work [29] which allows us to estimate the divertor potential profile drop ϕ_0 (which would be the same as in the standard Langmuir theory if temperature is constant[4]) and also an *effective target temperature*[5], T_{eff}, i.e. temperature which is expected to be measured by a divertor Langmuir probe[6] if real target temperature is $T_0 : T_e^{LP} \overset{prediction}{=} T_{eff}$

Thus in following, there are shown in section 12.2 the T, n-profiles extracted from the B2-EIRENE code, which finally comes as inputs to the computed ratios of T_{eff}/T_0 in Sec. 12.4. An interesting threshold phenomena found in Sec. 12.4 is further described and discussed in Sec. 12.5. A theoretical part (including additional density profile effect) is described in Sec. 12.3.

12.2 TCV $T(x), n(x)$-profiles from B2-Eirene code

The B2-Eirene package consists of a 2D, multifluid edge code (B2) describing the details of the ion and electron flow coupled to a 3D Monte-Carlo code (Eirene) [35] describing the dynamics of neutral particles (atoms and molecules). The code uses measurements of power balance from the plasma and profiles of T_e, T_i and n_e upstream from the divertor targets to prescribe cross-field diffusion coefficients for energy and particles which are then used to compute details of the charged particle flows in the SOL. Assuming values of the chemical sputtering yield and recycling coefficients at wall surfaces, the code computes a solution for the divertor plasma from which a number of parameters can be extracted for comparison with experiment (eg. radiation distributions in the divertor, particle and power fluxes to divertor targets). Important output parameters for the modelling described here are the parallel field profiles of density and temperature which, as mentioned earlier, cannot generally be measured experimentally. We have used these profiles from B2-Eirene runs of TCV discharges as input to the Wesson theory

[4] in this chapter "constant" always means "constant along magnetic field line"

[5] More or less different from T_0

[6] because it is just the potential drop which determines Langmuir probe VI-char.from which T_e is found.

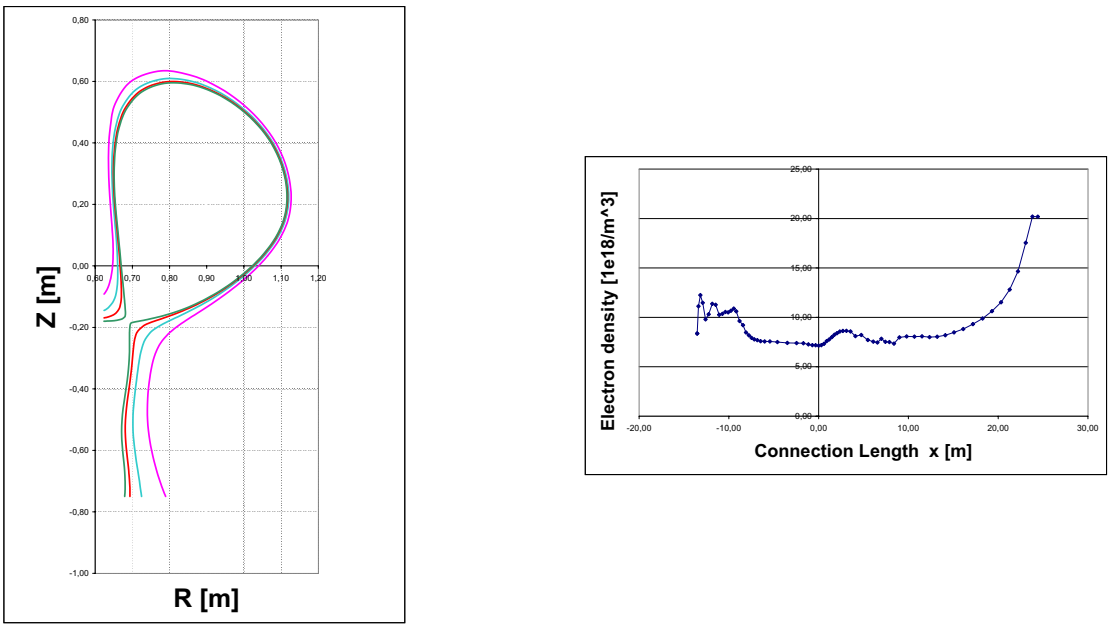

a) **b)**

Fig. 12.1: Example of results from the B2-EIRENE code: **a)** Magnetic surface configurations (with distances from midplane separatrix of 0.4, 1.8, 4.7, 9.6 mm) in poloidal cross-section (to be compared to Fig.9.3). The end points of the field line are the strike points. **b)** Density profile, now the connection length is distance from the stagnation point along magnetic field (which is mainly toroidal), inner target is at RHS of the fig.

(and its extended form). For any radial point on the target, the profiles are expressed in terms of the distance, along the total magnetic field, from the target to the *stagnation point* in the SOL, defined as half the total magnetic connection length between the two targets. For the work here, the connection length is also given with reference to a zero point at one target.

Typical B2-Eirene result used as an input to this model is shown in Fig.12.1.

12.3 Including density effect

In this section a theoretical part of this chapter is described and summarized at the end. It contains derivation of additional *effect of density profile,* following the Wesson's paper [29].

Before start, let us assign

$$T_0 \equiv T(0), n_0 \equiv n(0), \phi_0 \neq \phi(0) \equiv 0 \tag{12.2}$$

and mark equations used in the Wesson's paper [29] by symbol Eq.($?_W$). As a basic unit length we use *mean free path* at divertor target [1, p. 666]:

$$\lambda_0 = 8.5 \frac{T_0^2}{n_0} \ [mm, eV, 10^{18}/m^3] \tag{12.3}$$

12.3.1 Potential effect OFF

Calculate the electron current density j_e at the target plate:

$$j_e = e \int_0^{-\infty} f(0, v) v dv \tag{12.4}$$

where $f(x, v)$ is the *electron distribution function.* Since, in the absence of collisions, f is constant along a particle trajectory (i.e. the B-field line) we can approximate $f(0, v)$ by

$$f(0, v) = f(x, v'(x)) \tag{12.5}$$

up to the distance of the "last collision", the velocity $v'(x)$ being related to the velocity v *at* the surface by the energy-conservation equation

$$\frac{1}{2} m v^2 = \frac{1}{2} m v'^2(x) - e\phi(x) \tag{12.6}$$

where $\phi(0) \equiv 0$ and e is the electric charge. If one neglects change of potential *outside* the sheath then $\phi = \phi_0$. The more general case will be discussed in the chapter 12.3.2.

Now, in general we need to know $\phi(x), n(x), T(x)$. Further, we will *not neglect* role of $n(x)$ (as is in the [29]).

Let us assume the essential change in ϕ is only that across the sheath - the more general case will be considered in section 12.3.2. Thus, setting $\phi = \phi_0$ outside the sheath, substituting Eq.(12.5) into Eq.(12.4) and using Eq.(12.6) with $x = \lambda(v')$ (the MFP)

$$j_e = e \int_{-\sqrt{2e\phi_0/m}}^{-\infty} f(\lambda(v'), v') v' dv' \tag{12.7}$$

The distribution function is taken to be locally Maxwellian, that is,

$$f(x, v') = n(x) \sqrt{\frac{m}{2\pi k_B T(x)}} \exp\{-\frac{\frac{1}{2} m v'^2}{k_B T(x)}\} \tag{12.8}$$

where again $x = \lambda(v')$.

Substituting now this into Eq.(12.7):

$$j_e = e \sqrt{\frac{m}{2\pi}} \int_{-\sqrt{2e\phi_0/m}}^{-\infty} \frac{n(\lambda(v'))}{\sqrt{k_B T(\lambda(v'))}} \exp\{-\frac{\frac{1}{2} m v'^2}{k_B T(\lambda(v'))}\} v' dv' \tag{12.9}$$

Further, let us use only the following dimensionless variables

$$\begin{gathered} e\phi_{0(c)}(x) / \, k_B T_0 \to \phi_{0(c)}(\varepsilon) \\ \frac{T_{eff}, T(x)}{T_0} \to T_{eff}, T(\varepsilon) \\ n(x)/n_0 \to n(\varepsilon) \\ v \sqrt{\frac{m}{k_B T_0}} \to v \\ \sqrt{\frac{x}{4\lambda_0} \frac{n(x)}{n_0}} \stackrel{\text{def}}{=} \varepsilon = \frac{1}{2} v'^2 \end{gathered} \tag{12.10}$$

where $T(\varepsilon)$ is the temperature at $x = \lambda(\varepsilon)$ (and the same for $n(\varepsilon), \phi(\varepsilon)$). The equality for ε comes from the MFP relation [1, p. 666]

$$\frac{\lambda}{\lambda_0} = \frac{T^2}{n} \tag{12.11}$$

and the *equipartition theorem*[7] (not normalized $\frac{1}{2}mv'^2 = \frac{1}{2}k_BT$ corresponds to $v'^2 = T$)

$$4\varepsilon^2 \stackrel{\text{def}}{=} v'^4 = T^2 \tag{12.12}$$

which finally gives (for $x = \lambda(\varepsilon)$): $\varepsilon = \sqrt{\frac{n(x)}{n_0}\frac{x}{4\lambda_0}}$.

One therefore gets

$$j_e = -\frac{n_0\sqrt{T_0}}{\sqrt{2\pi m}}\int_{\phi_0}^{\infty}\frac{n(\varepsilon)}{\sqrt{T(\varepsilon)}}\exp\{-\frac{\varepsilon}{T(\varepsilon)}\}d\varepsilon \tag{12.13}$$

In contrast to Wesson's original model, which invokes an assumption about the magnitude of the ion current j_i balancing the electron current at the sheath edge, we set

$$j_i = n_0 c_s = n_0\sqrt{\frac{T_{0e} + T_{0i}}{m_i}}, \tag{12.14}$$

further assuming $T_i = T_e$, as usual, with c_s being the *ion sound speed* as representative of the ion flux density at the sheath edge. For any variation of density or temperature along the magnetic field, this equality will always remain true provided a stable sheath has formed [33].

Thus, finally, using $j_i + j_e = 0$, one gets an implicit equation for the desired unknown sheath potential drop ϕ_0:

$$\int_{\phi_0}^{\infty}\frac{n(\varepsilon)}{\sqrt{T(\varepsilon)}}\exp\{-\frac{\varepsilon}{T(\varepsilon)}\}d\varepsilon = 2\sqrt{\pi\frac{m_e}{m_i}} \tag{12.15}$$

After solving this one can define physically an *effective temperature* T_{eff} as a temperature constant along magnetic field line [8] $T_{eff} = T_{eff}(\phi_0(T_e(x)))$ which gives the same potential drop ϕ_0 as for the case of non-constant temperature profile $T_e(x)$. This ϕ_0 just determines the LP VI-char. which is used to find T_e.

Mathematically, T_{eff} can be thus found from Eq.(12.15) while fixing this just found ϕ_0 but now assuming constant temperature T_{eff}

$$\frac{1}{\sqrt{T_{eff}}}\int_{\phi_0}^{\infty} n(\varepsilon)\exp\{-\frac{\varepsilon}{T_{eff}}\}d\varepsilon = 2\sqrt{\pi\frac{m_e}{m_i}} \tag{12.16}$$

where for the constant density case the right-hand-side is just equal to RHS of Eq.(20_W).

[7] This model takes care about parallel velocity v' distribution which determines the sheath potential drop ϕ_0; the other perpendicular components of v' do not play role and therefore there is only one degree of freedom.

[8] just only for T_e=const the classical VI-char. processing (section C.1) works

12.3.2 Potential effect ON

We now return to the question of the $\phi(x)$-influence. In the above calculation, the entire change in ϕ was taken to be within the sheath, see Eq.(12.6). More generally there is a potential variation in the upstream plasma. Basically this arises from the electron force balance (22_W) $\nabla p_e = ne\nabla\phi$, where $p_e = nk_BT$ is the electron pressure. Differentiating this, one gets

$$\frac{1}{k_BT_0n_0}\nabla p_e = T(\varepsilon)(n(\varepsilon)-1) + n(\varepsilon)(T(\varepsilon)-1) = n(\varepsilon)(\phi(\varepsilon)-1) \tag{12.17}$$

Substituting now $\phi(\varepsilon)$ from Eq.(12.17) into Eq.(12.6) one gets a relation between v and v':

$$\frac{1}{2}v^2 = \frac{1}{2}v'^2 - \phi_0 + 1 + T(\varepsilon)(\frac{1}{n(\varepsilon)} - 2) \tag{12.18}$$

Using now Eq.(12.19) and Eq.(12.18) one gets

$$\varepsilon = \frac{1}{2}v^2 + \phi_0 - 1 - T(\varepsilon)(\frac{1}{n(\varepsilon)} - 2) \tag{12.19}$$

Differentiating this an expression for vdv

$$vdv = [1 + \frac{dT}{d\varepsilon}(\frac{1}{n(\varepsilon)} - 2) - \frac{dn}{d\varepsilon}\frac{T(\varepsilon)}{n(\varepsilon)^2}]d\varepsilon \tag{12.20}$$

is found. This Eq.(12.20) substitute into the Eq.(12.4) with Eq.(12.8) to get expression for j_e:

$$j_e = -\frac{n_0\sqrt{T_0}}{\sqrt{2\pi m}}\int_{\mathcal{E}_0}\frac{n(\varepsilon)}{\sqrt{T(\varepsilon)}}\exp\{-\frac{\varepsilon}{T(\varepsilon)}\}[1 + \frac{dT}{d\varepsilon}(\frac{1}{n(\varepsilon)} - 2) - \frac{dn}{d\varepsilon}\frac{T(\varepsilon)}{n(\varepsilon)^2}]d\varepsilon \tag{12.21}$$

where the *interval* of integration $\mathcal{E}_0$ is given by the Eq.(12.19) with[9] $v > 0$ as implicit function:

$$\mathcal{E}_0(\phi_0): \;\; \mathcal{E}_0 - \phi_0 + 1 - T(\mathcal{E}_0)[2 - \frac{1}{n(\mathcal{E}_0)}] > 0 \tag{12.22}$$

These Eq.(12.21) and Eq.(12.22) are identical to the Eq.(26_W) in the constant density case $n \equiv n_0 = 1$.

Thus, finally, using again $j_i + j_e = 0$, with j_i still given by Eq.(12.14), one gets an implicit equation for the unknown sheath potential drop ϕ_0:

$$\int\limits_{\mathcal{E}_0(\phi_0)}\frac{n(\varepsilon)}{\sqrt{T(\varepsilon)}}[1 + \frac{dT}{d\varepsilon}(\frac{1}{n(\varepsilon)} - 2) - \frac{dn}{d\varepsilon}\frac{T(\varepsilon)}{n(\varepsilon)^2}]e^{-\varepsilon/T(\varepsilon)}d\varepsilon = 2\sqrt{\pi\frac{m_e}{m_i}} \tag{12.23}$$

Again, when this is solved (i.e. ϕ_0 is found) the effective temperature T_{eff} can be found from Eq.(12.23) while fixing this just found ϕ_0 but assuming now constant temperature $T(\varepsilon) \to T_{eff}$:

$$\frac{1}{\sqrt{T_{eff}}}\int\limits_{\mathcal{E}_0^{eff}(\phi_0,T_{eff})} n(\varepsilon)[1 - \frac{dn}{d\varepsilon}\frac{T_{eff}}{n(\varepsilon)^2}]e^{-\varepsilon/T_{eff}}d\varepsilon = 2\sqrt{\pi\frac{m_e}{m_i}} \tag{12.24}$$

[9] physically, only electrons with positive target velocity do reach the target plate

which is again an implicit function of T_{eff}, where $\mathcal{E}_0^{eff}(\phi_0, T_{eff})$ is, similarly as Eq.(12.22), given by the Eq.(12.19) with $v > 0$ as implicit function

$$\mathcal{E}_0^{eff}(\phi_0, T_{eff}) : \quad \mathcal{E}_0^{eff} - \phi_0 - T_{eff}(1 - \frac{1}{n(\mathcal{E}_0^{eff})}) > 0 \tag{12.25}$$

where $T_0 = 1$ was exchanged by T_{eff} in Eq.(12.19) because T_0 is defined as $T_0 \equiv T(x = 0)$ which is now equal to T_{eff}.

12.3.3 Summary of equations

For the case without the potential effect one finds *the sheath potential drop* ϕ_0 by solving Eq.(12.15) and then *the effective target temperature* T_{eff} by solving Eq.(12.16) while using this just found ϕ_0.

For the case of including the potential effect use Eq.(12.23) instead of Eq.(12.15) and Eq.(12.24) instead of Eq.(12.16), where $\mathcal{E}_0^{(eff)}$ is given by Eq.(12.22),Eq.(12.25).

In following, the normalized units are defined in Eq.(12.10), λ_0 in Eq.(12.3) and Eq.(12.2).

The derived equations and used numerical methods have been *verified*

- in the case of constant density $n(\varepsilon) \equiv n_0 = 1$ when the result has to be independent of whether density effect is ON or OFF
- in the case of constant temperature $T(\varepsilon) \equiv T_0 = 1$ when the final T_{eff} should be equal to $T_0 = 1$

To solve these equations one has to know profiles of $T(x), n(x)$, which we took from the B2-EIRENE code [35], as is described in section 12.2.

12.4 Results

Using now the B2-Eirene profiles in this model we get Fig.12.2 of the effective temperatures T_{eff}. **The divertor target effective temperature is really several times higher than the local one,** $T_{eff} > 1$. It implicates important result that one can not believe the temperature T_e^{LP}measured by Langmuir probe in high recycling regimes; the Langmuir probe measures higher temperature, which is also the answer to the stated question.

Further, as a comment to the stated assumption in [29] that the effect of density is neglectable we can say the density effect is really smaller, maximally it is comparable with the effect of potential.

Including the potential effect slightly increases the potential profile far away from the target value[10]. This implicates greater electrons repulsion, thus the potential profile drop ϕ_0 has to decrease to satisfy still $j_i = j_e$ and therefore T_{eff} decreases, too.

On the other hand we expect the effect of density should increase ϕ_0 and T_{eff}. The B2-Eirene density profiles always *decrease* from high values at the target to lower values upstream,

[10] as assumed $\phi(x > x_{sheath}) = \phi_0$ for the case without potential effect

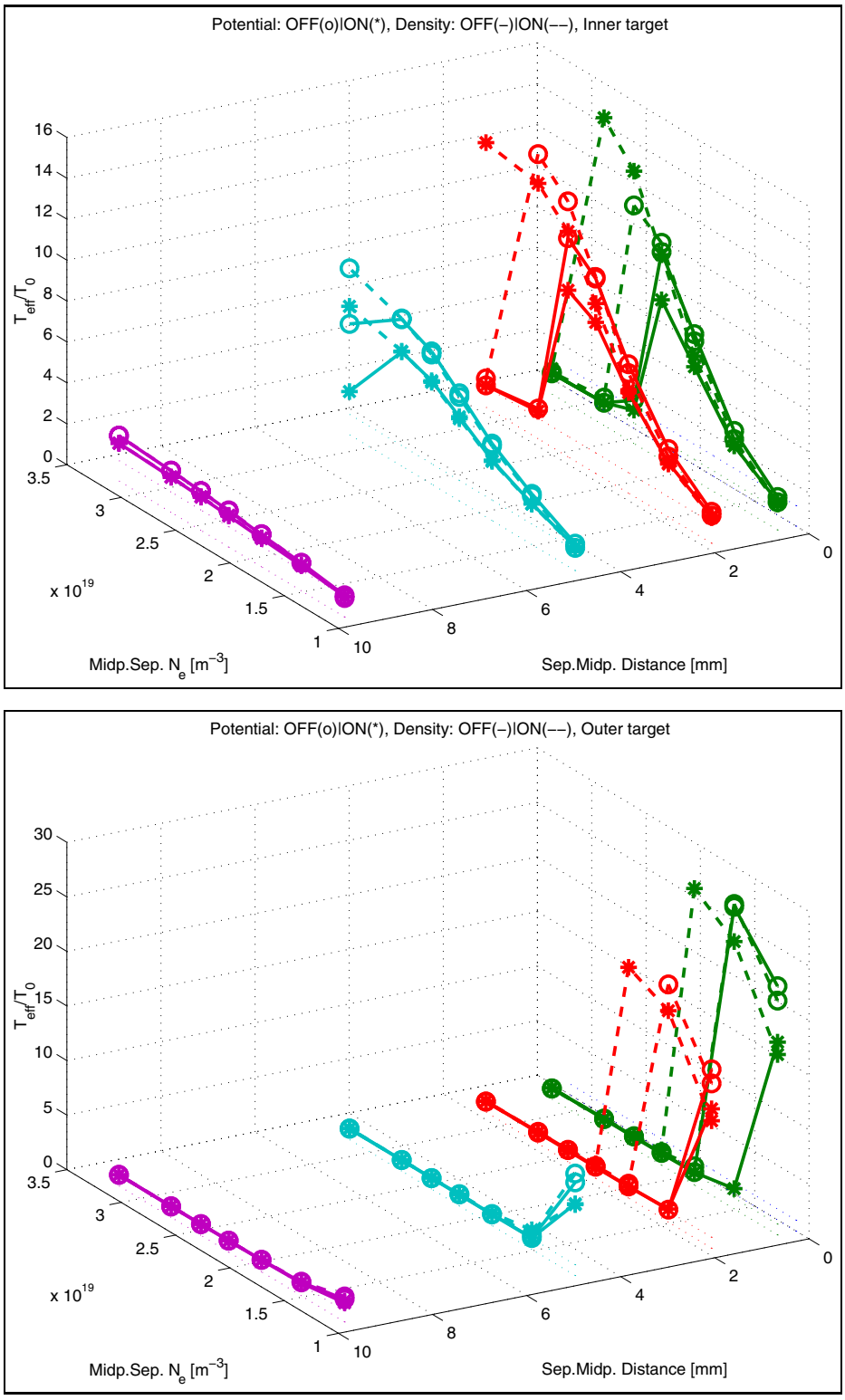

Fig. 12.2: Computed values of the T_{eff}/T_0 (using B2-Eirene profiles for TCV shot #17823) for the inner and outer target plate as a function of midplane density and distance from separatrix.

Fig.12.1. Since MFP goes like $\propto n_e^{-1}$ the distanced places should contribute more[11] and thus ϕ_0 and T_{eff} should increase.

These cases lead us to statement that potential effect ON (OFF) with density effect OFF (ON) leads to *lower (higher)* estimate of T_{eff}.

Indeed, it is visible from Fig.12.2 that Pot ON & Dens ON is always lower than the case OFF/OFF, except of cases near the threshold[12] when the ON/ON case reaches the threshold at higher densities. This could be a good reason why not to believe these T_{eff}s in these conditions. It might indicate that the principal assumption, Maxwellian distribution, can not be true, at least not near the threshold. From this viewpoint computing PDF like in [39] would be useful.

12.5 Threshold phenomena

Looking at T_{eff} dependence on density one can see the typical behaviour is that T_{eff} increases with density up to a certain point (the threshold) above which T_{eff} suddenly decreases to one. In other words, this model predicts that effective target temperature should be slightly higher (than the real target temperature) at low densities, much higher (up to $20 - 30\times$) at higher densities, and should suddenly decrease to right values $T_{eff} \sim 1$.

The following thoughts concern, for simplicity, only the case without both potential and density effect included. The more general case is discussed in Sec.12.6.

12.5.1 Mathematical observation

Three typical cases with increasing density have been chosen for the following analysis[13]:

- low[14] T_{eff}=12 before threshold, red curve
- high T_{eff}=23 before threshold, green curve
- very low T_{eff}=1.1 after threshold, black curve

Integrand of Eq.(12.15), Fig.12.4, corresponds to contributions to the target electron current density j_e of varied distanced pieces of plasma. The decrease at short distances is due to the exponential term $\exp(-\varepsilon/T)$ while T_e is about constant $T(\varepsilon) \simeq T_0$. The further increase (not for the red case) comes from increasing T_e (Fig.12.3): $T(\varepsilon) > T_0 \;\Rightarrow\; e^{-\varepsilon/T(\varepsilon)} > e^{-\varepsilon/T_0}$.

Integral of these curves (i.e. RHS of Eq.(12.15)) shows Fig.12.5. Its typical behaviour is just the reason for the threshold appearance. Indeed, the integral in Fig.12.5 always decreases until it gets *flat* when the integrand (Fig.12.4) reaches values close to values at the large middle part ($10^{-(2\div 3)}$ for the green curve). The integral starts to decrease again after reaching this middle part ($\varepsilon \simeq 60 \;\Leftrightarrow\; x \simeq 4m$ for the green curve). If now the curve in Fig.12.5 has its flat region *above* zero then ϕ_0 has to be large and therefore T_{eff} is large, too.

The threshold can be thus expressed using the following condition: RHS>LHS of Eq.(12.15), while integrating only in region $\varepsilon > \mathcal{E}_T$

[11] in comparison to density effect OFF

[12] i.e. the point of the T_{eff} sudden drop, discussed in detail in Sec.12.5

[13] outer target, densities m=1, 2, 3

[14] T_{eff} can vary from 1 up to high values

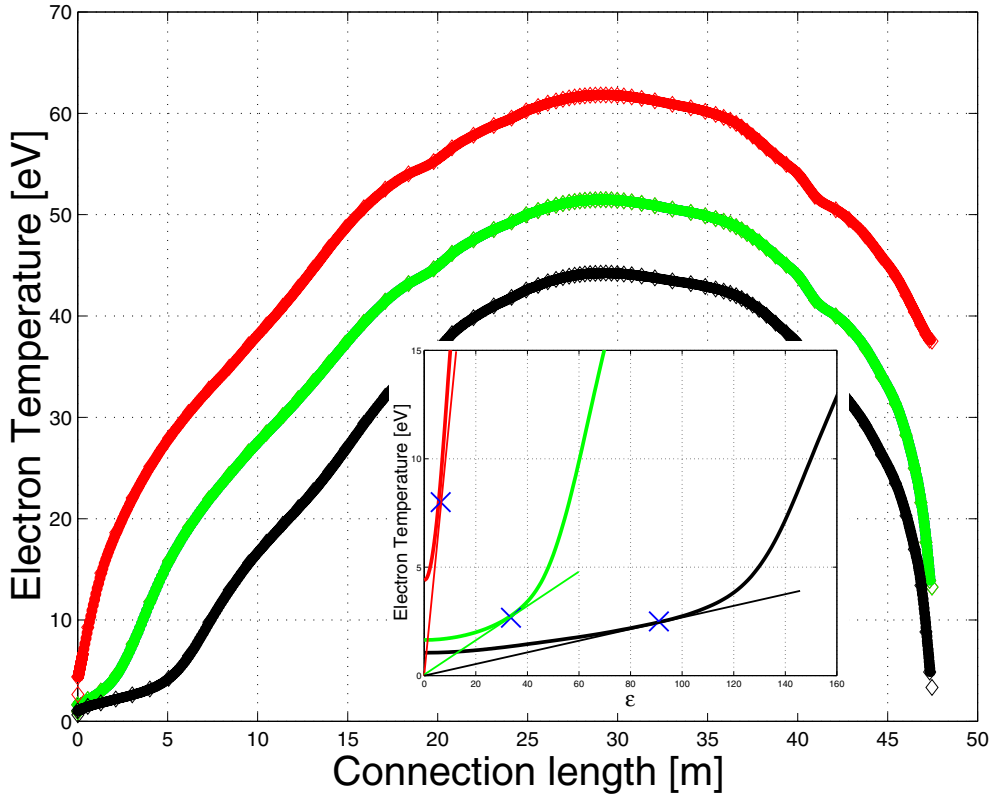

Fig. 12.3: Electron temperature profile with region close to target (now as a function of ε) in detail (there is no $\mathcal{E}_T$ in the red case).

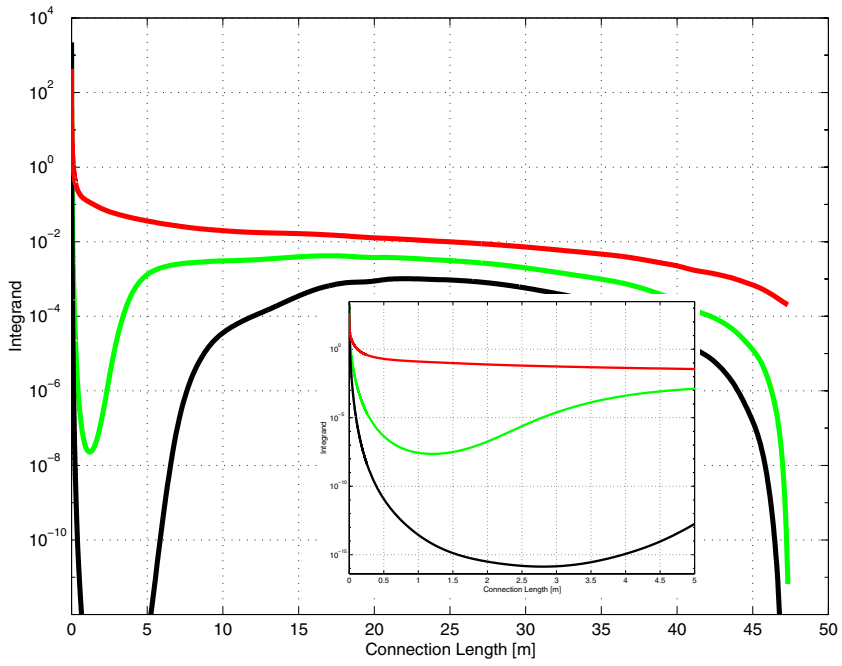

Fig. 12.4: Integrand of Eq.(12.15), i.e. contribution of distanced plasma regions to the target electron current. Region close to target is in detail.

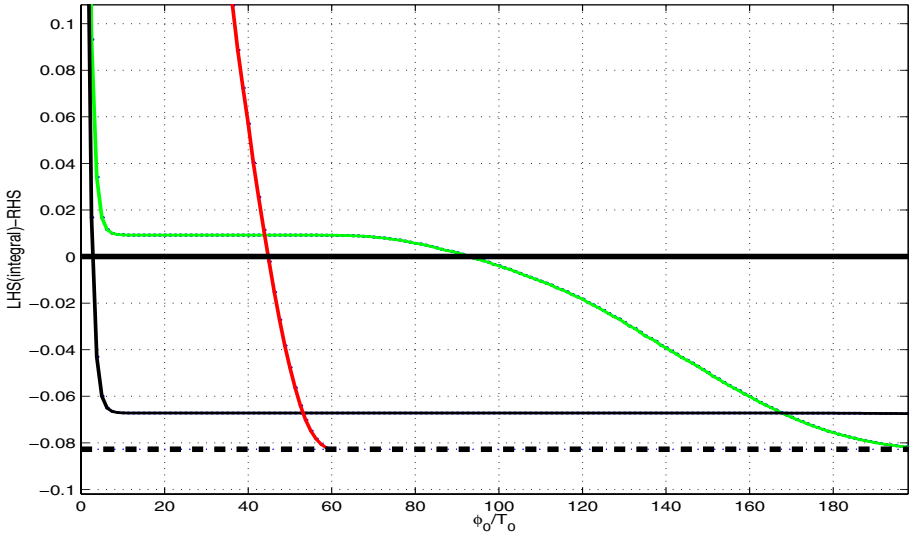

Fig. 12.5: LHS-RHS of Eq.(12.15), i.e. $\int_{\varepsilon>\phi_0} I(\varepsilon)d\varepsilon$ where I is just the integrand from Fig.12.4. Crossing zero axis defines ϕ_0 : $\phi_0^{red} \simeq 45$, $\phi_0^{green} \simeq 92$, $\phi_0^{black} \simeq 5$

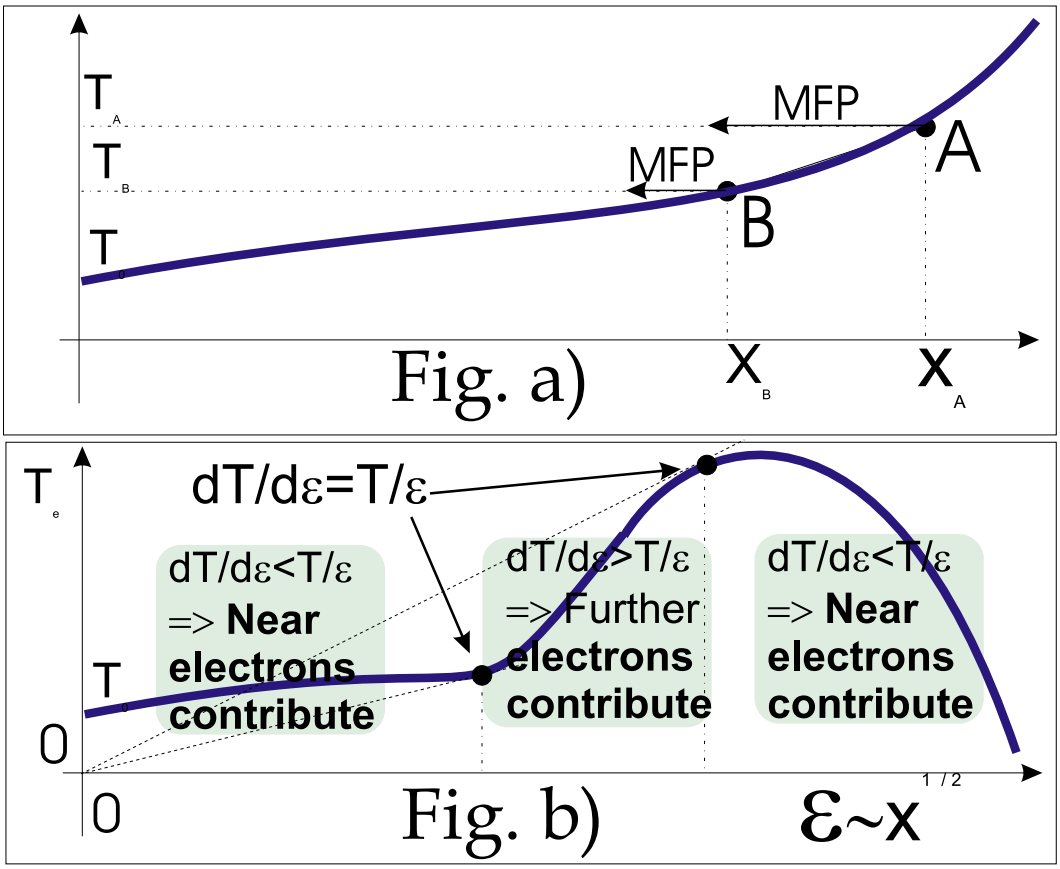

Fig. 12.6: Geometry of the threshold explanation

$$\int_{\mathcal{E}_T}^{\infty} \frac{1}{\sqrt{T(\varepsilon)}} \exp\{-\frac{\varepsilon}{T(\varepsilon)}\} d\varepsilon > 2\sqrt{\pi \frac{m_e}{m_i}} \tag{12.26}$$

where $\mathcal{E}_T$ divides the integrand into two regions[15]. Let's define $\mathcal{E}_T$ naturally as a minimum of the integrand

$$\frac{d}{d\varepsilon}(\frac{e^{-\frac{\varepsilon}{T(\varepsilon)}}}{\sqrt{T(\varepsilon)}}) = 0$$

thus $\mathcal{E}_T$ can be found by the following condition

$$\frac{dT}{d\varepsilon}|_{\varepsilon=\mathcal{E}_T} = \frac{1}{\frac{\mathcal{E}_T}{T(\mathcal{E}_T)} - \frac{1}{2}}. \tag{12.27}$$

Because $\frac{\varepsilon}{T} \gg 1/2$ is mostly satisfied for $\varepsilon = \mathcal{E}_T$ and also LHS of Eq.(12.26) does not matter much on the bottom limit since the integrand is minimal for $\varepsilon = \mathcal{E}_T$, therefore the Eq.(12.27) can be mostly simplified as

$$\frac{dT}{d\varepsilon}|_{\varepsilon=\mathcal{E}_T} = \frac{T(\mathcal{E}_T)}{\mathcal{E}_T}. \tag{12.28}$$

which geometrical meaning is depicted in the detailed Fig.12.3.

Thus the final result is that if Eq.(12.26) is satisfied than the integral in the flat region of Fig.12.5 is higher than the RHS and therefore both ϕ_0 and T_{eff} are high. **Eq.(12.26) with Eq.(12.27) just determines the threshold. Let us call $\mathcal{E}_T$ as a threshold point.**

If there is no $\mathcal{E}_T$, i.e. Eq.(12.27) has no solution, then T_{eff} is slightly higher than one - no threshold phenomena appeares, like it is for the model T_e-profile[16] from [29]

$$T = T_0 + (T_\infty - T_0) \tanh \frac{x}{l}; \tag{12.29}$$

indeed, Eq.(12.27) is not satisfied anywhere.

It is also surprising that the effect is *very fine*[17]: for a particular case just before and *very close* to the threshold (T_{eff} is high) it is enough to *decrease* the T_e-profile by several promilles

(!) to cross over the threshold to the low T_{eff} case, for example[18] (corresponding $T_e(x)$ shown in Fig.12.7):

$$T_{eff}(T(x)) = 22.1 \text{ is "high"} \quad \text{while} \quad T_{eff}(0.998 \cdot T(x)) = 2.9 \text{ is "low"}$$

where the statement "low/high" comes from the Eq.(12.26) and Eq.(12.27). Mind also that the MFP changes only twice, Eq.(12.19), i.e. by

[15] as will be shown in section 12.5.2, electrons coming from only one of the regions contribute to j_e

[16] l defines scale of the profile

[17] Of course, it depends on how deep (the deeper the faster the transition is) and long (the longer the more T_{eff} drops) is the well in the integrand in Fig.12.4. For example in detachment T_e(x) is flat in long region (black curve in Fig.12.3), the same for Fig.12.5 $\Rightarrow$ the T_{eff} drop during the threshold would be great.

[18] Potential-effect OFF, Density-effect OFF, Outer target, # 17823, m=2, sep. dist. 0.4 mm

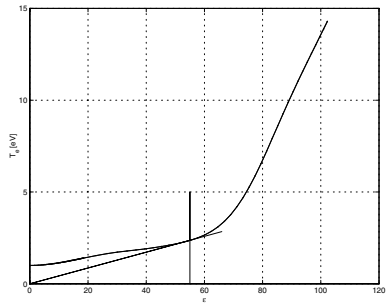

Fig. 12.7: T_e-profile just at the threshold (i.e. just RHS=LHS in Eq.(12.26)), with depicted $\mathcal{E}_T$. There are two nearly identical T_e-profiles (dots and line), described in the text, each with quite different T_{eff}: $T_{eff}^{dots} = 22.1,\ T_{eff}^{line} = 2.9$.

12.5.2 Physical explanation of the threshold

Let us derive now a simple model based on the MFP relation (see Eq.(12.19)) while assuming, for simplicity, density profile effect is negligible (Dens.OFF), and using Eq.(12.10)

$$\frac{\lambda_A}{\lambda_B} = \frac{T_A^2}{T_B^2} \tag{12.30}$$

The idea is sketched on the Fig.12.6a), where the points $\mathcal{A}$ and $\mathcal{B}$ are infinitessimally close. Electron PDF at both points $\mathcal{A}$ and $\mathcal{B}$ is expected to be Maxwellian.

Part of PDF contributing to the target electron current density j_e is proportional to λ/x. Let us assume now, that locally a condition

$$\frac{\lambda_A}{x_A} > \frac{\lambda_B}{x_B} \tag{12.31}$$

is satisfied, as depicted in the Fig.12.6a), and thus more distanced place (i.e. $\mathcal{A}$) contributes more to j_e than the place $\mathcal{B}$, i.e. the effective target temperature T_{eff} is then determined mainly by the more distanced part of the profile.

This condition can be rewritten as following: Eq.(12.30), Eq.(12.31) and Eq.(12.10) give together

$$\frac{\varepsilon_B}{\varepsilon_A} = \sqrt{\frac{x_B}{x_A}} > \sqrt{\frac{\lambda_B}{\lambda_A}} = \frac{T_B}{T_A} \tag{12.32}$$

and in term of local temperature gradient

$$\nabla_\parallel T_e \stackrel{\text{def}}{=} \frac{dT}{dx} = \frac{T_A - T_B}{x_A - x_B} \stackrel{Eq.(12.32)}{=} \frac{T_A(1 - \sqrt{\frac{\lambda_B}{\lambda_A}})}{dx} > \frac{T_A(1 - \sqrt{\frac{x_B}{x_A}})}{dx} = \frac{T_A(1 - \frac{\varepsilon_B}{\varepsilon_A})}{8\lambda_0 \varepsilon d\varepsilon} = \frac{T}{8\lambda_0 \varepsilon^2} \tag{12.33}$$

where the last equality is because the points $\mathcal{A}$ and $\mathcal{B}$ are infinitessimally close. Rewritting now $\nabla_\parallel T_e$ as

$$\frac{dT}{dx} = \frac{dT}{d\varepsilon}\frac{d\varepsilon}{dx} = \frac{dT}{d\varepsilon}\frac{1}{8\lambda_0 \varepsilon} \tag{12.34}$$

one gets finally expression

$$\frac{dT}{d\varepsilon} > \frac{T}{\varepsilon} \tag{12.35}$$

which can be interpreted as following (see Fig.12.6b): **if locally $\frac{dT}{d\varepsilon} > \frac{T}{\varepsilon}$ then the electrons comming from further distanced plasma contributes more to j_e, thus to the target potential drop ϕ_0 and therefore to the effective target temperature T_{eff}.**

Eq.(12.28) gave us *the same* condition and thus we can finally rewrite Eq.(12.26) more properly, based on arguments from this section, as:

$$\int\limits_{\frac{dT}{d\varepsilon} > \frac{T}{\varepsilon}} \frac{e^{-\varepsilon/T(\varepsilon)}}{\sqrt{T(\varepsilon)}} d\varepsilon > 2\sqrt{\pi \frac{m_e}{m_i}} \tag{12.36}$$

which can be interpreted like **if sum of contributions to the target electron current j_e comming only from regions satisfying $\frac{dT}{d\varepsilon} > \frac{T}{\varepsilon}$ is high enough (or even higher) to compensate j_i (i.e. Eq.(12.36) is satisfied) then the sheath potential drop ϕ_0 is formed dominantly by these, generally distanced and thus hotter, electrons, which leads finally to high T_{eff}.** In opposite, if Eq.(12.36) is not satisfied, then T_{eff} is low.

12.6 Conclusions and discussion

If this Wesson's model is correct one can conclude that in

- low recycling regime (red curve, no threshold point): T_{eff} is slightly higher above target temperature. Electrons collected by the probe come from far away regions, however, this region is too close because the threshold point $\mathcal{E}_T$ is too close to the target plate
- high recycling regime (green curve, before threshold): T_{eff} is very high $\Leftarrow$ electrons come from far away plasma
- detachment (black curve, after threshold): T_{eff} is 1, electron current density flowing from far away regions is not sufficient to compensate j_i anymore and thus ϕ_0 is given by the near plasma $\Rightarrow$ LP measures local T_e.

whether the assignments (low, high recycling and detachment) do really belong to the three T_{eff} cases is a question; it is only a suggestion, at least for the case with both potential and density effect included (which is the most sophisticated) the threshold appears at densities close to detachment density thresholds. Could, for example, this phenomena influence the divertor plasma at all ?

There is still a problem that TCV Langmuir probe data do not show such a threshold behaviour; we always measure T_e^{LP} several times higher than predicted by the B2-Eirene and spectroscopy but not so high as predicted by this model. However, we have no reference yet that LPs on other tokamaks do see it.

Chapter 13

Summary

Particular conclusions are included in each chapter separately.

13.1 Plans for future

I want to continue to work on the field of the thermonuclear fusion as a PhD-student. There are, however, two different principal ways from which I prefer the first one:

Work on TCV [1] in collaboration with Dr. R.A. Pitts. Theme of this research is planned to naturally continue on the field of edge plasma, especially fluctuations measurement during detachment and L-H transition by means of a *fast reciprocating Langmuir probe* which has been installed on the TCV last year.

Further, I would like to continue with the model described in Chap. 12 because its results are very interesting, especially the *threshold phenomena*.

In addition, chapters 10, 11 and mainly 12 are being compiled into a journal article to be submitted to the *Plasma Physics and Controlled Fusion* and presented as a poster at /11./

Work on CASTOR in collaboration with J. Stöckel. Theme would be based on measurement by a unique *two-dimensional probe*[2] and a unique *deep probe*[3], both developed on CASTOR recently.

Further, in collaboration with J. Gunn (Cadarache) I would run a numerical *particle in cell (PIC)* code, based on paper [24], computing the *rotating Mach probe*[4] or the *Gundestrup probe*[5].

In addition, I would like to rewrite and remeasure Chap. 6 and submit it as a paper of the *Plasma Physics and Controlled Fusion* journal[6].

[1] this work and study at EPFL is preliminary accepted by the head of the CRPP institute

[2] 8x8 pins in poloidal cross-section, see /6./

[3] this radial probe can be inserted deep into plasma without disrupting the discharge because the arm is very thin

[4] being used in CASTOR

[5] construction si planned

[6] I should have done it rather two years ago

13.2 Acknowledgements and remarks

- Chapters 5, 6 and 8 are parts of a grant project "Plasma turbulence in tokamak CASTOR", G-IA A 1043701.
- Chap.8 was presented as /5./ and published as [27] My contribution to this work was:

  - data-processing to create Fig.8.5, Fig.8.6, Fig.8.8, Fig.8.7, Fig.8.9, top and bottom windows of Fig.8.10
  - measurement assistance
  - discussion
  - small reconstruction of the poloidal probe head

- Concerning Chap.8 I would like to acknowledge to all the co-authors, [27]
- Concerning chapter 11 I would like to acknowledge to Prof. P.C. Stangeby (University of Toronto, Canada) for useful discussion
- Concerning chapter 12 I would like to acknowledge to A. Loarte (EFDA-CSU, Garching) for the B2-Eirene data and to J. Wesson for his interest and discussion

Part IV

Appendices

Appendix A

Poděkování (Thanks)

Protože není možné děkovat všem kteří si to zaslouží, zmiňuji jen ty nejvýznamnější:

- Děkuji těm, kteří ze mně vychovali člověka jež má rád sám sebe, lidi, přírodu a práci:
  - své ženě **Šárce** a **rodičům** za jejich lásku ♡ a domov, jež mi vytváří.
  - svým mnoha **přátelům**, :-)
- Děkuji svému **tátovi** a mnoha popularizátorům vědy (mj. J. Grygar, R. Feynman [57], G. Gamow [58], S. Hawking, ...) za probuzení mého *zájmu o fyziku.*
- Děkuji **Přírodě** a **své sestře** za poznání *důležitosti ochrany životního prostředí* před negativním vlivem civilizace.
- Děkuji manželům Wilhelmovým za jejich skvělý pionýrský oddíl s kterým nás tahali do Přírody a vedli diskuse o černých dírách, kulových blescích a (možná) i tokamacích.
- Děkuji mnoha učitelům gymnázia ve Valašském Meziříčí, že mi ukázali cestu nejen ke vědě ale i umění. Děkuji učitelům Novosadovi a Krouské za pevné nervy při hledání ztraceného Horáčka ve skalách, horách a lesích.

Děkuji všem zaměstnancům oddělení Tokamak ÚFP AV ČR za jejich *pomoc, pochopení, ochotu a umožnění mé seberealizace* na tokamaku CASTOR:

- Především svému *vedoucímu diplomové práce* p. **Stöckelovi** za jeho skvělé *vedení* (zvláště při seznamování se s problematikou fúze a fyziky plazmatu), fyzikální intuici a nápady, prosazení o vstup do EURATOMu, jeho pracovní *nadšení*.
- Panu **Žáčkovi**, *vedoucímu oddělení*, za jeho nevyčerpatelný optimismus, úsměv a ochotu pomoci s čímkoli.
- Studentům M. Hronovi, V. Weinzettlovi, I. Ďuranovi za jejich spolupráci a rady.
- *Technikům* panu **Zelenkovi** za každodenní skvělou připravenost tokamaku k měření; panu **Jiránkovi** za konstrukci Langmuirových sond.

Jsem také vděčný, že jsem důležitými životními křižovatkami správně prošel. Že jsem:

- vyšel z řevu a špíny diskoték do velebného ticha hvězd; díky, Malý princi [59]
- vystřízlivěl z romantických představ celoživotního pasení oveček, šerpování v Tatrách, řízení kamiónů ...
- psychicky přežil první ročník MFF UK (díky, Davide a Šárko!) a již tehdy objevil nabídku spolupráce na výzkumu termojaderné fúze a zašel se přeptat, juch!

Thank to Dr. **R.A. Pitts** for his collaboration, supervising and offer to work on at TCV.

A všem výše uvedeným děkuji také za jejich úsměv :-).

Děkuji také, že mi bylo umožněno psát tuto práci v angličtině (což není obvyklé v západních zemích) - ulehčilo mi to značně práci.

Appendix B

Overview of shots

B.1 Swingable probe measurements of (fluctuations of) I_{sat} and V_{fl} profile

Scanning of the I_{sat} and V_{fl} profiles in poloidal cross-section. In Fig.5.1 places of measurements are shown.

These experiments are described in chapters 5 and 6.

- february'97, shots $\# \ 4541 - 4586$, small limiter $a = 60mm$, I_{sat} measured at $-85V$
- april'98, shots $\# \ 6084 - 6140$, I_{sat} measured at $(-195V \pm 10)V$
- spring'00, $9255 - 9286$, I_{sat} measured at $(-130V \pm 10)V$
- $9443 - 9484$

B.2 Biased plasma diagnosed by Langmuir probe arrays

Systematic measurements of *poloidal and radial structure sizes (cross-correlation function parameters) and fluctuation level* during both Biasing and OH.

These experiments are described in chapter 8.

- july'97, *radial* and *poloidal* array of probes, shots $\# \ 5184 - 5240, 5282 - 5301, 5323 - 5335$, I_{sat} *measured at* $(-80 \pm 10)V$

  Introduction to the measurement technique, *cross-correlation function* computation
- may-august'98, *poloidal* probe array, shots $\# \ 6515 - 6533, 6680 - 6801$
- august'98, *radial* probe array, only V_{fl} measurement, shots $\# \ 6802 - 6841$
- autumn'98, *radial and poloidal* probe array, only V_{fl} measurement, shots $\# \ 6896 - 6931, 6936 - 6999$
- $7303 - 7389$ new design of the poloidal probe, $7409 - 7440, 7470 - 7483$
- measurement of the Reynolds stress, $V_{fl}(r), \ v_{pol}^{phase}(r)$: $7762 - 7770, 7792 - 7853, 7942 - 7983$

Remarks: Radial probe placed from the *top*, *Rail limiters* also used, since shot $\# \ 6936$ a new (mushroom-like) electrode installed for Biasing.

Appendix C

Basic theory

C.1 Langmuir probe theory

Langmuir probe is an *active* and well-localized diagnostic tool. It is just a biased short and thin pin inserted into plasma. It is used as the *main diagnostic tool for fluctuations measurement*, for estimating *local plasma temperature, density and potential*. *"Active"* implicates that it unfortunately *influences*[1] plasma; in spite of e.g. spectroscopy that just only *looks* at it. This is the general reason why being careful when using of Langmuir probes. Langmuir probes are therefore used mostly in the edge[2].

The collected current I_{coll} is a function of applied voltage[3] V_{appl} as ([1, chap. 10.9], [10]):

$$I_{coll} = I_{sat}(1 - \exp(\frac{e(V_{appl} - V_{fl})}{k_B T_e})), \tag{C.1}$$

where e is the electric charge, T_e is electron temperature, k_B is the Boltzmann constant[4], I_{sat} is the *ion saturation current*, V_{fl} is the *floating potential*. This equation does not take into account the *electron saturation current,* E_{sat}, at which I_{coll} saturates as $I_{coll}(V_{appl} \to +\infty) = E_{sat}$, and which is expected tobe[5]

$$E_{sat}/I_{sat} = -v_e/v_i = due\ to\ Eq.(2.3) = -\sqrt{m_i/m_e} \sim -43 \tag{C.2}$$

Ideal probe characteristic is shown in Fig.C.1, example of real ones in Fig.10.1.

Floating potential, V_{fl}, defined (due to Eq.(C.1)) as $I_{coll}(V_{fl}) = 0$, is related to the plasma potential ϕ as [10]:

$$V_{fl} = \phi - T_e \ln \sqrt{\frac{m_i}{m_e}} \simeq \phi - 3\frac{k_B T_e}{e} \tag{C.3}$$

where m_i, m_e are masses of ions, resp. electrons. If $V_{appl} \to -\infty$ then I_{coll} saturates at a value

[1] Impurities are evaporated from the probe surface and also negative electric (Debye) shield is created in vicinity of the probe [1, chap. 9.2].

[2] Not in CASTOR: because of low temperature and density Langmuir probes can be placed as deep as $0.4\ a$, see Fig.5.1.

[3] V_{appl}>0 corresponds to positive probe with respect to liner/chamber

[4] mind that $k_B T_e$ has dimension of energy, usually measured in electronvolts eV

[5] The ratio E_{sat}/I_{sat} is not always given as in Eq.(C.2), e.g. during the so called ***plasma detachment*** its amplitude falls even to 1, [31, p. 1346].

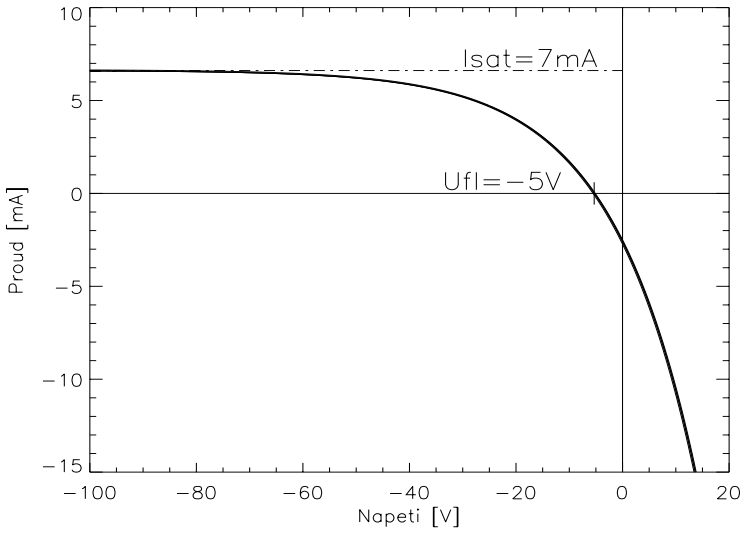

Fig. C.1: Ideal VI-characteristics of a single Langmuir probe

called *the ion saturation current*, I_{sat}:

$$I_{sat} = \frac{e}{2} A n_e \sqrt{\frac{k_B(T_e + T_i)}{m_i}}, \tag{C.4}$$

which is directly proportional to local electron density n_e. A is an active probe area, T_i is the ion temperature, respectively. Neglecting temperature fluctuations [6], the fluctuations of potential ($\tilde{\phi}$) and density ($\tilde{n}$) are related to the measured quantities (due to Eq.(C.3)) and Eq.(C.4)):

$$\tilde{V}_{fl}(t) = \tilde{\phi}(t), \qquad \tilde{I}_{sat}(t) \propto \tilde{n}_e(t) \ .$$

Poloidal electric field, E_p is usually measured by two floating probes (1, 2) spaced by distance d in poloidal direction:

$$E_p \stackrel{\text{def}}{=} -\nabla\phi = due\ to\ Eq.(C.3) = -\nabla\phi + const \cdot \nabla T_e \simeq -\nabla\phi \simeq (V_{fl}^{(1)} - V_{fl}^{(2)})/d \ .$$

Measurement of only V_{fl} is, due to its definition $I_{coll}(V_{fl})$=0, the simplest measured quantity: just measure potential of an isolated probe immersed into plasma. When wanted to know the local density of plasma, use the Eq.(C.4); now it is necessary to bias the probe to *negative* potential high enough: condition $I_{coll}(V_{appl}) \approx I_{sat}$ gives, due to Eq.(C.1), condition on V_{appl}: $\exp(\frac{e(V_{appl}-V_{fl})}{k_B T_e}) \ll 1 \ \Leftrightarrow \ V_{fl} - V_{appl} \gg \frac{k_B}{e} T_e$.

When wanted to know T_e, it is necessary to measure the whole VI-char. The problematic about T_e-measurement is discussed in detail in chapters 10, 11, 12.

[6] In comparison to $\tilde{V}_{fl}$

C.2 Limited/Diverted plasma configurations

To *keep plasma off the walls* a limiter and a divertor have been invented.

C.2.1 Limiter

Limiter [1, chap. 9.9] is a material plate placed radially *a bit deeper* into plasma column than walls, see the ring limiter in Fig.3.1. Therefore each particle flying outwards hits the limiter surface first, instead of the wall.

A limiter plays a number of roles in tokamak operation. It serves primarily to protect the wall from the hot plasma, especially when there are instabilities (the material of the limiter has to be therefore capable of withstanding high heat loads). Secondly, the limiter localizes the plasma-surface interaction. The high power and particle density at the limiter surface causes rapid removal of adsorbed gas, oxide layers and other easily desorbed impurities. When only the clean substrate remains it is possible to maintain plasmas with lower impurity levels. Thirdly, the limiter localizes the particle recycling.

C.2.2 Divertor

Divertor [1, chap. 9.10] defines the last closed flux surface (LCFS) not by a material surface (as in the limiter case), but by a magnetic field, as depicted in Fig.9.3. In comparison to the limiter case it is a more efficient way of keeping plasma off the walls because the distance from LCFS and the *strike point* is longer (by distance between the X-point and the strike point, Fig.9.3). This allows the recycled (impure & cold) particles (flying from the divertor plates into the hot plasma) to be ionised and may be swept back to the target by the plasma flow before they enter the confined plasma.

The divertor configuration also enables to reach the so called phenomena of *divertor detachment*.

C.2.3 Detachment

[36] Under certain operating conditions the plasma at one or both of the divertor plates of a single null divertor has been reported to detach. The primary indication of detachment is a *decrease by up to an order of magnitude in the ion saturation current* I_{sat}, registered by Langmuir probe embedded in the target plate. The electron temperature T_e measured by the probes tend to be already rather low before detachment, $\leq 5\ eV$, but may show further decrease at detachment. At the same time, the scrape-off-layer (SOL) plasma conditions far from the target remain essentially unchanged and the confined plasma may be little affected by the detachment.

In addition, increased power favours the attached state, but sufficiently high density can cause detachment even for high impurity power.

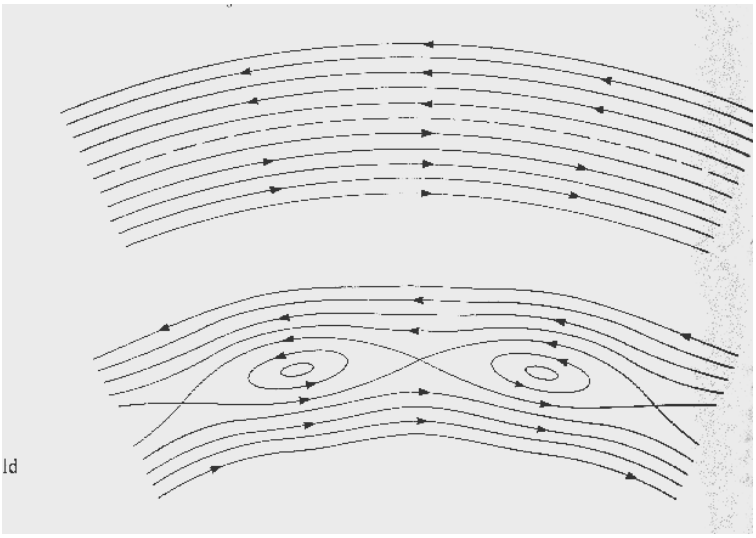

Fig. C.2: The magnetic field reconnection, i.e. formation of the magnetic islands. The top/bottom figure (in poloidal cross-section) shows $\vec{B}_{pol}$ before/after the reconnection.

C.3 Rational surfaces and magnetic islands

Rational surface is defined as a surface with constant and rational safety factor q

$$q \stackrel{\text{def}}{=} \frac{r}{R}\frac{B_{tor}}{B_{pol}} = m/n,$$

where m, n are both *small integers.* Their meaning is that any B-field line joins up on itself after m toroidal and n poloidal rotations around the torus[7], [1, chap. 3.4].

At these rational surfaces the B-field lines can break (due to the *MHD-instability*) and *reconnect* to form *Magnetic islands*, [1, chap. 7.2], Fig.C.2.

From the confinement point of view the magnetic islands are *wrong* because of the further process:

Particle at some B-surface inside an island can move radially easily by flying along the given B-line; magnetic island is a region of very fast (along B-field) *radial* movement.

Fast Radial Movement due to Magnetic Island

particle at $r < r_{island}$ *→ getting into the island (by a proper collision, across B-field) → fast radial movement inside the island (along B-field) → getting off the island (by another proper collision, across B-field)*

The islands can exist in several different radii (at which q is rational) so that these island regions can *overlap* which leads to a *chaotic case* with even *higher* cross-field diffusion, Fig.C.3.

Easy indication of magnetic islands is based on B_r-fluctuations measured by external *Mirnov coils*, Fig.4.1. It measures periodical fluctuations of frequency

$$f_{coil} = n \cdot f_{island} \tag{C.5}$$

[7] in fact, it defines helicity of B-field

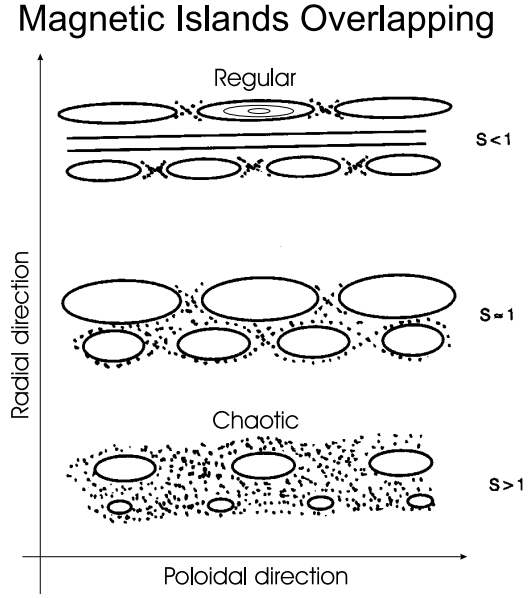

Fig. C.3: Overlapping of the magnetic islands (in poloidal cross-section). Any given B-line can either walk in the closed region of an island (mostly in the "Regular"-case) or (if starting in the "chaotic"-region) walk chaotically both in poloidal and radial direction (while, of course, it always walk mainly in the toroidal direction).

because the magnetic islands formation rotates poloidally with a certain frequency $f_{island} = \frac{v_{pol}}{2\pi r_{island}}$. What n should be taken in Eq.(C.5) can be estimated from q-profile (i.e. value of $q = m/n$) with expected small integer m.

C.4 Plasma polarization = Biasing

This is a method which would lead into *enhanced confinement* due to *transport barrier formation in the edge*. The main idea is to create *enhanced electric field gradient* which causes the *fluctuation induced* $\vec{E} \times \vec{B}$*-drift drops* $\Rightarrow$ the loss of particles (and so energy) is suppressed.

(Electrode) Biasing $\Rightarrow$ higher $\nabla E_r \Rightarrow$ higher $\nabla_r v_{pol} \Rightarrow \tilde{n}$ & $\tilde{E}_p$ structures are destroyed,
Fig.C.5 $\Leftrightarrow$ amplitude & mutual correlation of $\tilde{n}$ & $\tilde{E}_p$: $\Gamma_r = (\tilde{n}\tilde{E}_p C(n, E_p))/B_T$ drops,
Fig.8.11 $\Rightarrow \tau_p$ increases $\Rightarrow \tau_E$ increases, as desired

See the schema of the electric circuit, Fig.C.6. More about physics during biasing is in chapter 8.

and H_α-radiation profile [1, p. 182].

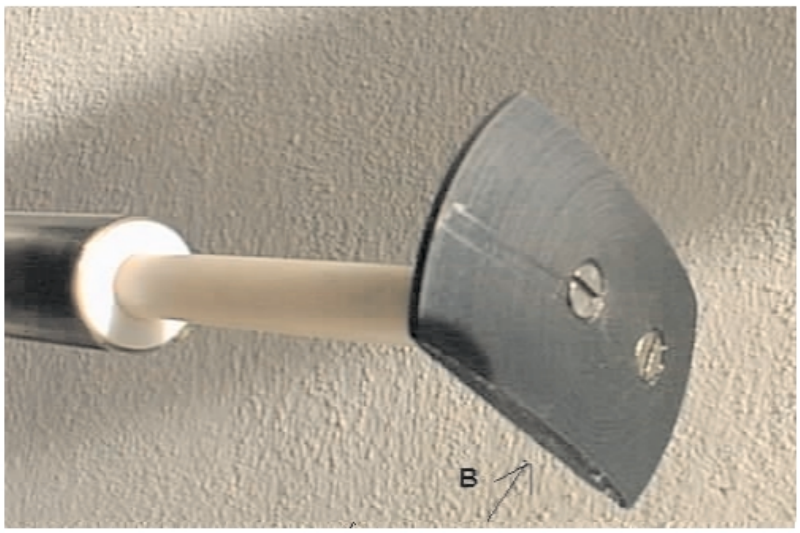

Fig. C.4: Biasing electrode, mushroom-like shaped, made of carbon, with surface of 27 cm^2 (toroidaly 80° from the limiter)

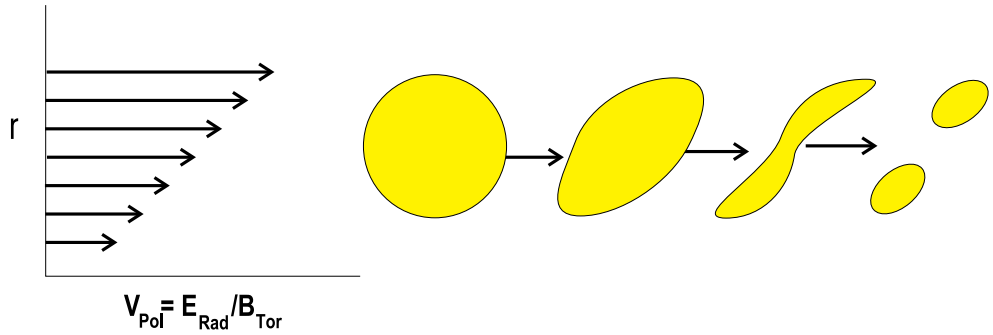

Fig. C.5: Model of $\tilde{n}$ & $\tilde{\phi}$ structures destruction due to radial gradient of poloidal velocity $\frac{dv_{pol}}{dr} \neq 0$.

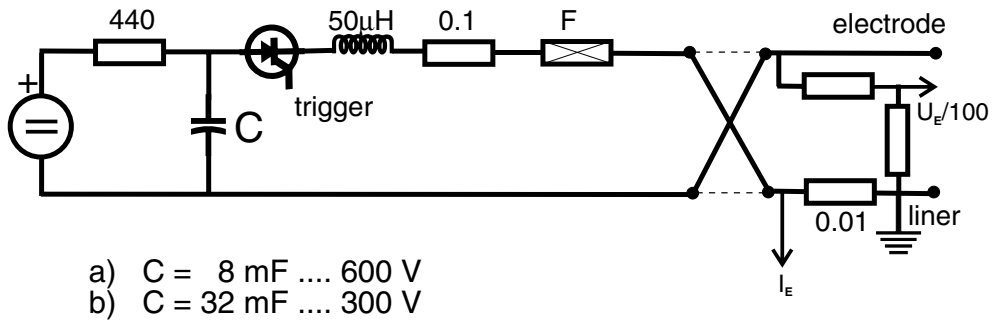

Fig. C.6: Electric circuit of the electrode.

Appendix D

Used Units, Abbreviations, Concepts and Symbols

There is a list of (links to) fusion related (basic) concepts on
tokamak.ipp.cas.cz/∼horacek/abbreviations/abbreviations.htm

$W_{(e)}$	Watt=Joule/second of (electric) power
e	electron charge, $e = -1.6 \times 10^{-19}\ C$
eV	ElectronVolt: energy obtained by voltage drop of $1V$ of a particle charged at $1e$
x, L_c	Connection Length, i.e. distance along magnetic field line with respect to a divertor target (where $L_c = 0$)
Θ	Poloidal Angle *Coordinate*
Φ	Toroidal Angle *Coordinate*
r	Radial *Coordinate*, $r \in (0, b)$
x, y	Cartesian *Coordinate* ($x = r \cdot \cos\Theta, y = r \cdot \sin\Theta$)
R, a, b	Major, Minor, wall radius

Table D.1: Units and Coordinates

ADC	Analog to Digital Convertor
APS	American Physical Society, http://www.aps.org/
B2-EIRENE	A big 2D multifluid edge numerical code B2 coupled with a 3D neutral gas Monte-Carlo numerical code EIRENE, [35]
CASTOR	Czech Academy of Sciences TORus, tokamak.ipp.cas.cz
(R)CCF	(Radial) Cross-Correlation Function
EPS	European Physical Society, http://www.eps.org/
EURATOM	EUROpean ATOMic agency, europa.eu.int/comm/research/fusion1.html
FWHM	Full Width at Half Maximum
HFS	High Field Side
IAEA	International Atomic Energy Agency
ITER	Int. Thermonuclear Experimental Reactor, www.iter.org, Fig.2.2
JAERI	JApan Atomic Energy Research Institute, device JT-60U, www-jt60.naka.jaeri.go.jp
JET	Joint European Tokamak, www.jet.uk
LCFS	Last Closed (magnetic) Flux Surface, i.e. Separatrix, Fig.9.3
LFS	Low Field Side
LHS	Left Hand Side
LP	Langmuir Probe, see section C.1
MHD	MagnetoHydroDynamic
PDF	Probability Distribution Function
RC	Rogowski Coil, see Index
RHS	Right Hand Side
SD	Standard Deviation $\sqrt{<(\tilde{q})^2>}$
SOL	Scrape-Off Layer, Fig.9.3, layer with open field lines crossing limiter or divertor plate; SOL is radially outside LCFS, [1, chap. 9.3]
TCV	Tokamak á Configuration Variable, crppwww.epfl.ch, chap. 9
TFTR	Tokamak Fusion Test Reactor, www.pppl.gov/TFTR
tokamak	russian word: TOroidalnaya KAmera i MAgnytnaya Katushka meaning toroidal chamber and magnetic coil
VSL	Velocity Shear Layer

Table D.2: Abbreviations

Aspect ratio	$A \stackrel{\text{def}}{=} R/a$
B-surface, (B-) field (lines)	Magnetic surface, field (lines), Fig.2.3
Biasing	transport barrier creation method by creating additional E_r at the edge, see chap. C.4
Core	the plasma center, Fig.9.3
Divertor	see Section C.2.2
H_α-radiation	measure of hydrogen recycling between plasma and surrounding surfaces, [1, p. 182]
Detachment	see Section C.2.3
Edge	edge of the plasma column up to LCFS, Fig.9.3
H_α	proportional to influx of neutral hydrogen from the wall, i.e. intensity of recycling
H-mode	High (i.e. enhanced in comparison to L-mode) energy confinement time mode, reached only in the divertor configuration in a spontaneous transition from L-mode (e.g. in TCV during increasing $\bar{n}_e$), necessary for future fusion devices, [1, p. 179]
L-mode	(Standard) Low confinement time mode, see H-mode, [1, p. 177]
Limiter	see Section C.2.1
OH	Ohmic Heating, fundamental tokamak heating used as a concept for regime without biasing
Strike Point	a point in a poloidal cross-section where LCFS crosses divertor plates, i.e. a place of the greatest energy deposition, see Fig.9.3
Transport barrier	potentially enhances confinement, created e.g. by biasing or NBI
X(Null)-point	a place of zero poloidal magnetic field, i.e. crossing of LCFS, see Fig.9.3
Effective ion charge, Z_{eff}	defined as $Z_{eff} = \frac{\sum_j n_j Z_j^2}{\sum_j n_j Z_j}$, where n_j, Z_j are density and charge of present ion species (i.e. $j \in \{electrons, ions\}$), [1, chap. 2.16]
Safety factor q	defined as $q \stackrel{\text{def}}{=} \frac{d\Phi}{d\Theta} = \frac{r}{R}\frac{B_{tor}}{B_{pol}}$, i.e. how many times the field line goes toroidally during one poloidal circulation, [1, p. 111]. Usually $dq/dr < 0$, Fig.6.3. as higher q as greater stability $\Rightarrow$ q is called "safety"

Table D.3: Concepts

$\tilde{q}$	fluctuation of q; $\tilde{q} \stackrel{\text{def}}{=} q - < q > \ \Rightarrow \ < \tilde{q} > \equiv 0$
$\propto$	proportionality; $q \propto p \ \Leftrightarrow \ q = k \cdot p, \ k = const$
$\equiv$	equivalent (by definition)
$\stackrel{\text{def}}{=}$	defined
$\simeq$ or $\sim$	nearly equal
$< ... >$	in time mean value; $< q > \stackrel{\text{def}}{=} \frac{1}{T} \int_a^{a+T} q(t)dt$
$(...)$	equation
$[...]$	bibliography citation, p. 101
$/.../$	presentation citation, p. 99
A	Active probe area
A	Aspect ratio $A \stackrel{\text{def}}{=} R/a$
$\vec{B}, B_t \equiv B_\Phi, B_p \equiv B_\Theta$	(Toroidal, Poloidal) magnetic field
c_s	ion sound speed $c_s = \sqrt{\frac{T_e + T_i}{m_i}}$
D	Deuterium, ${}^2_1H$
$errf$	error function $errf(b) = \frac{2}{\sqrt{\pi}} \int_0^b e^{-x^2} dx$
$E_t \equiv E_\Phi, E_p \equiv E_\Theta, E_r$	(Toroidal, Poloidal, Radial) electric field, $\vec{E} = -\nabla\phi$
I_p	Total Plasma Current
I_{sat}	Ion Saturation Current, defined as $I_{sat} \stackrel{\text{def}}{=} I_{coll}(V_{appl} \to -\infty)$
j_i, j_e, j_T	ion, electron, target current density
k_B	Boltzmann constant: $k_B T = n \cdot eV \Leftrightarrow T = n \cdot 11600K$
L	Particle number along the central chord
E_{sat}	Electron Saturation Current, defined as $E_{sat} \stackrel{\text{def}}{=} I_{coll}(V_{appl} \to +\infty)$
U_{fl} or V_{fl}	Floating Potential defined as $I_{coll}(V_{fl}) = 0$
ϕ	plasma potential
$(m_e, m_i)\ m$	(Electron, Ion) Mass: $m_e c^2 = 0.51 MeV$, $\frac{m_i}{Z} = m_p = 1836 m_e$
n_e, n_i	electron, ion plasma density, usually $[10^{18} m^{-3}]$
q	Safety factor - see Tab.D
T	Tritium, ${}^3_1H$
$(T^{LP}_{e,i})\ T$	(electron, ion) Temperature (measured by LP), $[eV]$
τ_p	particle confinement time, mean living time of an ionized particle inside a torus
τ_E	energy confinement time, defined as [1, p. 144] $\tau_E = \frac{Energy\ Content\ in\ Vessel}{Input\ Power} = \frac{\frac{2}{3}\int n(T_i + T_e) d^3x}{I_p U_{loop} + P_{add.\ heating}}$
U_{loop}	Loop Voltage
$v_\perp, v_\parallel$	velocity perpendicular (parallel) to magnetic field
$v^{phase}_{pol}, v^{flux}_{pol}$	(phase, flux) poloidal velocity
Z_{eff}	Effective ion charge - see Tab.D

Table D.4: Symbols

Appendix E

Publications, Conferences & Workshops

Actualized at tokamak.ipp.cas.cz/∼horacek/publications.html

/ 1/ Hron M, Stöckel J, Kryška L, Horáček J.: "Langmuir Probe Characteristics in Magnetized Plasmas", IAEA Technical Committee Meeting on Research Using Small Tokamaks, Prague, 26-28 Nov. 1996, No Proceeding

/ 2/ 18th Symposium on Plasma Physics and Technology, Prague, Czech Republic, June 1997, *poster* by M. Hron, J. Stöckel, L. Kryška, J. Horáček: *Langmuir Probe Characteristics in Magnetized Plasmas,* Proc. p. 8

poster: Stöckel J, Jakubka K, Kryška L, Žáček F, Ďuran I, Horáček J, Hron M, Petržílka J.: *Plasma Turbulence on the CASTOR Tokamak,* Proc. p. 39-41

/ 3/ J. Stockel, F. Zacek, L. Kryska, J. Badalec, K. Jakubka, M. Hron, J. Petrzilka, I. Duran, L. Krlin, J. Horacek: *"External Control of Edge Turbulence on CASTOR Tokamak",* final report of the IAEA research contract No. 6702/RB/R2, 1997

/ 4/ Stöckel J, Badalec J, Ďuran I, Hron M, Horáček J, Jakubka K, Kryška L, Petržílka J, Žáček F, Heller M.V.P, Brazilio Z.A, Caldas I.L.: "Magnetic and Electrostatic Fluctuations in the CASTOR tokamak", *published* as [26]

/ 5/ Hron M, Ďuran I, Dyabilin K, Horáček J, Jakubka K, Kryška L, Nanobashvili I, Nanobashvili S, Stöckel J,Tendler M, Van Oost G, Žáček F.: "Edge Turbulence at Plasma Polarization on the CASTOR Tokamak",

presented

- as a *poster* at the 26th EPS Conference on Controlled Fusion and Plasma Physics, as a *talk* (by M. Hron) at the 2nd REFPCE Workshop, both held in Maastricht, The Netherlands, June 1999, proc. ECA Vol. 23J (1999), p. 1589
  tokamak.ipp.cas.cz/∼hron/26EPS.pdf
- at WDS 1999, MFF of Charles University, Prague 1999, proc. p.268
  http://tokamak.ipp.cas.cz/∼hron/WDS99.pdf

and *published* as [27]

/ 6/ 27th EPS Conference on Controlled Fusion and Plasma Physics, Budapest, Hungary, *poster* by J. Stockel, M. Hron, I. Duran, K. Dyabilin, J. Horacek, K. Jakubka, L. Kryska, E. Martines, S. Nanobashvili, G.Van Oost, M. Tendler, F. Zacek: *"Plasma polarization of the separatrix on the CASTOR tokamak"*, submitted paper

tokamak.ipp.cas.cz/∼horacek/articles/eps2000.pdf

/ 7/ R.A. Pitts, B.P. Duval, J. Horáček, A. Loarte, J. Mlynář, J.-M. Moret, A. Refke, J. Rommers: *"Divertor Geometry Effects on Detachment in TCV",* 14th Int. Conf. on Plasma Surface Interaction in Controlled Fusion Devices (PSI), May 22-26 2000, Rosenheim, Germany,

crppwww.epfl.ch/∼pitts/pdf/psi2000_paper.pdf

/ 8/ J. Horacek: *talk* about this thesis at CRPP EPFL, August 2nd 2000

in preparation

/ 9/ K. Dyabilin, J. Stockel, F. Zacek, I. Duran, M. Hron, J. Horacek, K. Jakubka, L. Kryska, S. Nanobashvili, I. Nanobashvili: *"Modelling of the biasing experiment"*, sent to PPCF

/10/ R.A. Pitts, B.P. Duval, A. Loarte, J.-M. Moret, J. Horacek: *"Detachment in Variable Divertor Geometry in TCV"*, 18th IAEA Fusion Energy Conference, Sorrento, Italy, 4-10 October 2000,

http://crppwww.epfl.ch/∼pitts/pdf/pitts_iaea2000_abstract.pdf

/11/ R.A. Pitts, J. Horacek and A. Loarte: *"On the Measurement of Electron Temperature by Single Langmuir Probes in High Recycling Divertors"*, 42nd APS meeting, 23-27 October 2000, Quebec City, Canada, sustaines just from Chap. 10, 11, 12 of this thesis http://crppwww.epfl.ch/∼pitts/pdf/pitts_aps2000_abstract.pdf

Bibliography

[1] Wesson J.: *Tokamaks*, Clarendon Press - Oxford, 1997, the 2nd edition, easy-readable detail review book of tokamaks, the most cited literature in this thesis, 680 pages

[2] Chen F.F.: *Introduction to Plasma Physics*, Plenum Press, New York, 1974 an overview book for beginners in plasma physics

[3] Miyamoto K. : *Plasma physics for nuclear fusion*, really theoretical review book, The MIT Press, Cambridge in Massachusetts, USA, 1989

THESES

(available in the CASTOR building)

[4] Ďuran I.: Diplomová práce, 1997

[5] Weinzettl V.: Diplomová práce, 1997, tokamak.ipp.cas.cz/∼vwei/work/work.htm

[6] Fiala M.: *Využití obnovitelných zdrojů pro energetické účely*, Diplomová práce, mujweb.cz/veda/potomci, 1999

[7] Hron M.: Diplomová práce, 1996, tokamak.ipp.cas.cz/∼hron

[8] Petržílka J.: PhD. Thesis, 1997

TURBULENCE & FLUCTUATIONS

[9] Valovic M.: "Control of plasma position in the CASTOR tokamak", Czech. J. Phys. **B 39** (1989)

[10] M.Šícha, M. Tichý, V. Hrachová: Langmuir probe measurements in the low and the middle pressure plasma - Single probe technique, MFF UK, internal publication of MFF UK, detailed studies of different Langmuir probe theories

[11] J. Boedo, G. Van Oost et al: Czech. J. Phys, 48 (1998),12, Suppl. S3, p. 99

[12] M. Tendler: Plasma Phys. Control. Fusion, 39 (1997), B371-B382

[13] F. Wagner et al: Phys. Rev. Lett, 49, 1982, 1408

[14] E.J. Synakowski et al: Phys. Plasmas, 4(5) (1997),1736

[15] R.R. Weynants et al: Plasma Phys. Contr. Fusion, 40 (1998), 634

[16] R.R. Weynants, G.Van Oost et al: Nuclear Fusion, 32 (1992), No.5, p. 837

[17] J.A.C. Cabral et al: Plasma Phys. Control. Fusion, 40 (1998), 1001-1019

[18] F. Žáček et al: Czech. J. Phys, 48 (1998),12, Suppl. S3, p. 60

[19] Vayakis G.: *Anomalous Transport in the Tokamak Edge*, PhD-thesis, department of Engineering Science, Culham, UK, April 1991

[20] J. Petržílka, J. Stöckel: Contrib. Plasma Phys, 38S (1998), 74

[21] M. Endler et al: Nucl. Fusion, **35** (1995), 1307-1339

[22] B.Ph. van Milligen a col.: "Long-range correlations and universality in plasma edge turbulence", Physical Review Letters, **80** (1998), No.20

[23] F. Žáček, S. Nanobashvili, *internal report:* "8mm Microwave Reflectometry for Tokamak CASTOR", 1996

[24] J.P. Gunn, "Two dimensional quasineutral PIC simulation of a Gundestrup probe", Czech. J. Phys, **48**, p. 293 (1998)

[25] Nedospasov A. V, Sov. J. Plasma Phys. 15 (1989), p. 659

[26] J. Stöckel, J. Badalec, I. Ďuran, M. Hron, J. Horáček, K. Jakubka, L. Kryška, J. Petržílka, F. Žáček, M.V.P. Heller, Z.A. Brazilio, I.L. Caldas: "Magnetic and electrostatic fluctuations in the CASTOR tokamak", Plasma Phys. Control. Fusion **41** (1999), p. A577-A585, UK

[27] M. Hron, I. Ďuran, K. Dyabilin, J. Horáček, K. Jakubka, L. Kryška, S. Nanobashvili, I. Nanobashvili, J. Stöckel, M. Tendler, G. Van Oost, F. Žáček: "Edge Turbulence at Plasma Polarisation on the CASTOR Tokamak", Czechoslovak Journal of Physics, **49** (1999), Suppl. S3, p. 181 tokamak.ipp.cas.cz/∼hron/2REFPCE.pdf

[28] J. Stöckel, I. Ďuran, V. Dhyani, M. Hron, K. Jakubka, L. Kryška, V. Svoboda, F. Žáček, J. Petržílka, I. Nanobashvili, S. Nanobashvili: In Proc. of Int. Conf. on Plasma Phys, Nagoya 1996, Vol. 1, p. 322

DIVERTOR PHYSICS

[29] J.A. Wesson: "Effect of temperature gradient on plasma sheath", Plasma Phys. Control. Fusion **37** (1995) 1459-1466, UK,

tokamak.ipp.cas.cz/∼horacek/articles/wesson.pdf

[30] C.S. Pitcher and P.C. Stangeby: *review article of* "Experimental divertor physics", Plasma Phys. Control. Fusion **39** (1997) pages 779-930, UK

[31] P.C. Stangeby: "Determination of T_e from a Langmuir probe in a magnetic field by directly measuring the probe's sheath drop using a pin-plate probe", Plasma Phys. Control. Fusion **37** (1995), p. 1337-1347

[32] P.C. Stangeby: "A problem in the interpretation of tokamak Langmuir probes when a fast electron component is present", Plasma Phys. Control. Fusion **37** (1995), p. 1031-1037

[33] P.C. Stangeby, Phys. Fluids **27** (1984), p. 682

[34] R. Behn et al., Rev. Sci. Instr. **70** (1999), p. 768

[35] R. Schneider et al., J. Nucl. Mater. 196-198 (1992), p.810-815

[36] P.C. Stangeby: "Can detached divertor plasmas be explained as self-sustained gas targets?", Nucl. Fusion, **33**, No. 11 (1993), p. 1695-1705

[37] Y. Shimomura, M. Keilhacker, K. Lackner, H. Murmann,Nucl. Fusion **23** (1983), p. 869-879

[38] J.G. Watkins *et al.*, J. Nucl. Mater. 266-269, p. 980

[39] O.V. Batishchev et al: "Kinetic effects in tokamak SOL plasmas", Phys. Plasmas **4** (5), 1997, p. 1672

ENVIRONMENTAL & ECONOMICAL ASPECTS OF FUSION

[40] *journal* "Vesmír" (The Universe), Czechoslovak Academy of Sciences, **67** (1988), No. 3

[41] *journal* "Ochrana ovzduší" (climate conservation), (2000), No. 2

[42] *journal* europhysics news, **29**, No. 6, 1998, published by the EPS: epswww.epfl.ch

[43] H. Cabal *et al.*: "Environmental externalities of a future fusion power plant", 26th EPS Conf. on Contr. Fusion and Plasma Physics, Maastricht, ECA **23J** (1999), p. 1453-1456

[44] I. Cook *et al.*: "Direct Cost of Electricity from Fusion Power Plants", 26th EPS Conf. on Contr. Fusion and Plasma Physics, Maastricht, ECA **23J** (1999), p. 225-228

[45] Doc. ing. Petr Otčenášek, Csc.: "Volba zdrojů elektrické energie pro Českou republiku" (Choose of an electric energy supply for the Czech republic), Media 2000, s.r.o, 1997

[46] report on "Havárie v jaderné elektrárně Černobyl" (The Chernobyl nuclear power-station accident), Public relations ČEZ a.s. Jungmannova 29, Praha 1

[47] Doc. ing. Petr Otčenášek, Csc.: "Jaderná energetika" (Nuclear Energetics), SPN, The Charles University, Prague, 1989

[48] D.H. Meadows, D.L. Meadows, J. Randers, W.W.III. Behrens: "The limits to Growth", Chelsea Green, Pan Books, London, 1972

[49] D.H. Meadows, D.L. Meadows, J. Randers: "Beyond the limits", Chelsea Green, Post Mills, 1992

[50] B. Moldan: "Životní prostředí a globální perspektiva" (The Environment and Global Perspective), printed by the Center for the Environmental Tasks of the Charles University, ISBN 80-7066-938-1, Karolinum, Prague, 1995

[51] P.K. Kaw: "Fusion power: Who needs it?" - Artsimovich memorial lecture, IAEA Conference of Nuclear Fusion, IAEA-CN-56/A-0, Proc. I, Würzburg, 1993

[52] article "Fusion Reactor Economic, Safety and Environmental Prospects" from book "Safety, Environmental Impact and Economic Prospects of Nuclear Fusion" of *Proceeding of the 9th Course of the Int. School of Fus. Reactor Technology, August 6-12, 1989, in Erice, Sicily, Italy*

[53] magazín "Energie" www.energie.panorama.cz

[54] časopis "Věda, technika a my" (VTM), **6**, 2000

[55] firm SOLARTEC s.r.o. (Solar cell production and photovoltaic applications), 1. máje 1000 / M3, CZ-765 61, Rožnov pod Radhoštěm, The Czech Republic

---

MISCELLANEOUS

[56] Reader's Digest Výběr, "O dvou Castorech", str. 9, leden 1999,
tokamak.ipp.cas.cz/∼vwei/work/vyber.gif

[57] R.P. Feynman: "To snad nemyslíte vážně", Mladá Fronta, Praha, 1989

[58] G. Gamow: "Pan Tompkins v říši divů", Mladá Fronta, 1986, ("Mr. Tompkins in Paperback", Cambridge Univ. Press, 1965)

[59] A. de Saint-Exupéry: "Malý Princ" (The Little Prince), Albatros, Praha, 1994

Index

View publication stats